UCLouvain

École polytechnique de Louvain

Functionalization of graphene with magnetite nanoparticles

Author: **Diego Fossion**
Supervisors: **Benoît Hackens, Sophie Hermans**
Readers: **Jean-Christophe Charlier, Sébastien Faniel**
Academic year 2019–2020
Master [120] in Physical Engineering

Acknowledgements

First of all, I would like to thank my two promoters, Professors Sophie Hermans and Benoît Hackens for their incredible availability throughout this entire semester. In spite of this difficult period, I felt supported and motivated throughout my master thesis, even from a distance, which was a great source of motivation. They were always available to discuss with me the experimental and simulation results I was getting as I went along.

I would also like to thank Nadzeya Kryvutsa for involving me in her research throughout this master thesis and for her excellent feedback when writing my master thesis. She introduced me to the research and despite the difficulty encountered with our samples, taught me many things. She confirmed my desire to continue the research after my master thesis. I wish her good luck for the last year of her thesis.

Then, I would like to thank Nicolas Moreau. First of all, for the Kwant simulations where he made himself available at any time throughout this semester to answer my numerous questions. Then, for taking the time (several times) to explain us how the measurement system worked. Finally, I want to thank him for his very valuable feedback on the different chapters of my work.

Then, I would like to thank Zeila Zanolli and Guillaume Brunin for their help with my Abinit simulations. Thank you for answering all my questions throughout this semester.

Finally, I would like to thank Sébastien Toussaint who was always available to point me in the right direction or simply to answer my questions when a point of theory was unclear.

Abstract

When Rashba spin-orbit coupling and exchange field are induced in the graphene by proximity effect, a phenomenon called quantum anomalous Hall effect is obtained. This phenomenon induces the presence of a bandgap in the bulk graphene and a Hall resistivity of $\frac{1}{2}\frac{h}{e^2}$ is obtained. In this master thesis, we will investigate the effect induced by the presence of magnetite nanoparticles on the surface of graphene.

In the simulation part, tight-binding simulations are performed to simulate the effect of Rashba spin-orbit coupling and exchange field on the electronic transport in the graphene and highlight the quantum anomalous Hall effect in graphene. The effect of non-uniform Rashba spin-orbit coupling and exchange field is studied to mimic the presence of nanoparticles.

In the experimental part, the samples used were contaminated leading to a significant shift of the Dirac point. As the purpose is to deposit nanoparticles, we needed to limit the presence of other contaminants that could disrupt the future measurements. In this part, the different cleaning steps and their effect on the Dirac point and the graphene quality are detailed. Besides, the first results obtained after deposition of nanoparticles are described. Indeed, the quality is not affected by the presence of nanoparticles and the Dirac point had shifted from $12V$ before deposition to $6V$ after deposition.

Contents

Introduction

The study of topological insulator in condensed matter has attracted a lot of attention. These materials are insulating in the mass but have edge states, as in the case of the quantum Hall effect, but without the presence of an external magnetic field.

In this master thesis, the material used to study this new state of matter is graphene, a two-dimensional crystal with a hexagonal lattice composed of carbon atoms. It was first isolated by K. Novoselov and A. Geim in 2004 [1]. At low energy, the charge carriers of graphene behave like relativistic particles, giving them incredible electronic properties that have attracted the attention of many researchers for several years.

In 1988, Haldane was the first one to theoretically demonstrate a topological phase in graphene and to discover the presence of edge states without applying a magnetic field [2]. This phase is also known as the quantum anomalous Hall effect. However, this model is difficult to obtain experimentally in graphene.

In 2005, Kane and Mele described a new graphene effect called the quantum spin Hall effect [3], induced by the intrinsic spin-orbit coupling of graphene. Due to this effect, at each edge, a spin state propagating in opposite directions should be observable. However, graphene has a weak intrinsic spin-orbit coupling. Fortunately, observation of edge states without applying a magnetic field can be obtained by inducing Rashba spin-orbit coupling and proximity exchange field with other materials as in Ref. [4] by covering the graphene $RbMnCl_3$.

In this master thesis, the quantum anomalous Hall effect induced by the proximity effect with magnetite nanoparticles will be studied. These nanoparticles are composed of iron oxide surrounded by an organic envelope and are always magnetized. These nanoparticles induce a Rashba spin-orbit coupling and an exchange field in graphene.

In section 1, the various electrical properties and the tight bonding pattern of graphene will be described. The effect of the magnetic field inducing a quantum Hall effect in the graphene will also be described.

In section 2, the theory of topological insulation will be developed. First, the Berry's phase and curvature will be explained. Then, the quantum Hall effect, explained in section 1 by solving the Shrödinger equation, will be explained by considering the topological theory. Indeed, materials subjected to a high magnetic field are topologically not negligible. Then, the Haldane model and the graphene quantum spin Hall effect will be detailed.

In section 3, the magnetic properties of magnetite nanoparticles will be described. As will be explained, in the mass phase, magnetite is a ferrimagnetic material. However, when small diameter magnetite nanoparticles are used, the material becomes superparamagnetic.

In section 4, the results obtained with Kwant, a python set used for numerical computations, with particular emphasis on quantum transport, will be presented to highlight the presence of edge states. In addition, the results of the ab-initio computation will be detailed. An iron atom close to the surface of the graphene 4x4 supercell has been used to obtain the value of the band gap in the graphene mass.

In section 5, the different experimental equipments used during this master thesis will be presented. First, the general principle of the Raman spectroscopy will be developed. The description of the different peaks generally observed with graphene will be given. Then, the atomic force microscope will be described.

In section 6, a rapid description of two techniques of graphene synthesis will be given: the mechanical exfoliation and the chemical vapor deposition.

In section 7, the samples and the different cleaning steps used to lower the Dirac point will be presented. Electrical measurement will also be discussed.

In section 8, the synthesis of magnetite nanoparticles will be detailed.

In section 9, the different results obtained after the deposition of nanoparticles on graphene will be presented and discussed.

1 Graphene Physics

In this section, the physics in graphene will be explained. Firstly, the crystal structure and the band structure of graphene, obtained by using the nearest-neighbors tight-binding model, will be developped. Secondly, some electronic properties as the backscattering in graphene and the ambipolar effect will be shown. Finally, the effect of the magnetic field will be described.

1.1 Crystal structure of graphene

Graphene is a monolayer of graphite and was firstly isolated by K. Novoselov and A. Geim in 2004 [1]. It is a one-atom thick layer composed of sp^2-hybridized carbon atoms organized in a honeycomb lattice [5, 6] as represented in figure 1.

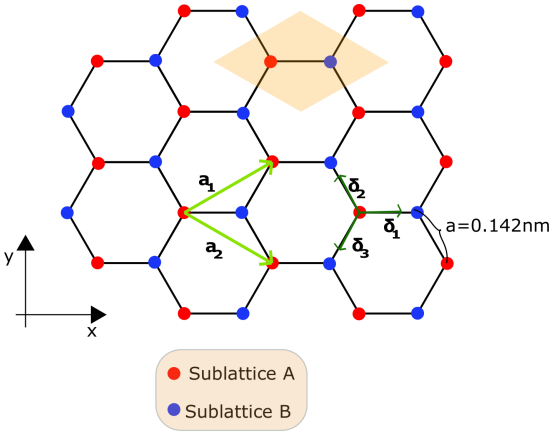

Figure 1: Representation of the lattice of graphene. The unit cell is indicated in orange. The sublattices A and B are represented in red and blue respectively. The nearest-neighboring carbons are separated by a distance $a_{cc} = 0.142nm$.

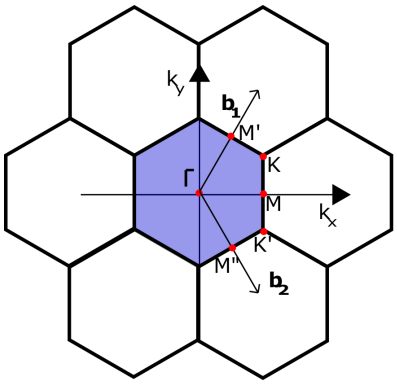

Figure 2: Representation of the reciprocal lattice. The first Brillouin zone is represented in blue with Γ, the center and K/K', the two inequivalent corners.

Its structure is composed of two triangular sublattices, A and B as shown in figure 1. The honeycomb lattice can also be seen as a triangular lattice with a two-atoms basis [6]. The unit cell is represented in orange in figure 1. The two basis vectors of the real space lattice are given by [7]:

$$\mathbf{a}_1 = \frac{a_{cc}\sqrt{3}}{2}(\sqrt{3}, 1) \text{ and } \mathbf{a}_2 = \frac{a_{cc}\sqrt{3}}{2}(\sqrt{3}, -1) \tag{1}$$

with $a_{cc} = 0.142nm$, the distance between two carbon atoms.

The reciprocal space is represented in figure 2. The reciprocal lattice vectors are given by [7]:

$$\mathbf{b}_1 = \frac{2\pi}{3a_{cc}}(1, \sqrt{3}) \text{ and } \mathbf{b}_2 = \frac{2\pi}{3a_{cc}}(1, -\sqrt{3}) \tag{2}$$

The Brillouin zone, in blue in figure 2, is composed of several crystallographic points: Γ, K, K', M, M', M''. These points are inequivalent since they can not be linked by a linear combination of the reciprocal basis vectors. Point K and K', called Dirac points, have an important role in the electronic properties of graphene and their coordinates are

$$K = \frac{2\pi}{3a}(1, \frac{1}{\sqrt{3}}) \text{ and } K' = \frac{2\pi}{3a}(1, -\frac{1}{\sqrt{3}}) \tag{3}$$

1.2 Band structure of pristine graphene

Carbon atoms possess 6 electrons, which are in the configuration $1s^2 2s^2 2p^2$ in the ground state. Two of these electrons are in the inner shell $1s$ and do not contribute to chemical reactions. When several carbon atoms are close to each other, one electron is excited from the $2s$ shell to the $2p$. In the case of graphene, each carbon atom will form three sp^2 bonds with their nearest-neighbors leading to three σ bonds. These bonds do not contribute to the electrical transport in graphene. However, the out-of-plane p_z orbital of a carbon atom will form π bonds between two electrons of neighboring atoms. These electrons, called π-electrons, determine the low-energy properties of graphene and are responsible for its uncommon electrical properties.

A tight-binding approximation that describes the π-electrons can be determined by solving the time-independent Schrödinger equation and by only considering the interaction between atoms and their first-nearest-neighbours [5, 6, 8, 9]:

$$H\Psi(\mathbf{r},\mathbf{k}) = E\Psi(\mathbf{r},\mathbf{k}) \tag{4}$$

with $\Psi(\mathbf{r},\mathbf{k})$ and E, respectively, the eigenfunctions and the eigenvalues of the Hamiltonian H. The wavefunction can be separated in two parts due to the two sublattices:

$$\Psi(\mathbf{r},\mathbf{k}) = A\Psi^{(A)}(\mathbf{r},\mathbf{k}) + B\Psi^{(B)}(\mathbf{r},\mathbf{k}) \tag{5}$$

with A and B, two unknown amplitude parameters and $\Psi^{(A)}$ and $\Psi^{(B)}$, two Bloch functions associated to the A and B sublattices. They can be written as a linear combination of the atomic orbital wave:

$$\Psi^{(j=A \text{ or } B)}(\mathbf{r},\mathbf{k}) = \frac{1}{\sqrt{N}} \sum_{\mathbf{R}} e^{i\mathbf{k}\cdot\mathbf{R}} \phi^{(j)}(\mathbf{r}+\boldsymbol{\delta}_j - \mathbf{R}) \tag{6}$$

$\phi^{(j)}(\mathbf{r}+\boldsymbol{\delta}_j - \mathbf{R})$ is the atomic orbital wave of the electron that describes the p_z orbitals. The electron is close to the j atom located at the position $\mathbf{R}-\boldsymbol{\delta}_j$ at the Bravais lattice $\mathbf{R}$. N is the number of unit cells in the crystal lattice.

In this theoretical part, as presented in the paper of M.O. Goerbig [6], the sites A are considered to coincide with the sites of the Bravais lattice. The three vectors $\boldsymbol{\delta}_j$, represented in figure 1, connect sublattice A to sublattice B and are given by:

$$\boldsymbol{\delta}_1 = a(1,0),\ \boldsymbol{\delta}_2 = \frac{a}{2}(-1,\sqrt{3}) \text{ and } \boldsymbol{\delta}_3 = \frac{a}{2}(-1,-\sqrt{3}) \tag{7}$$

After the description of the wavefunction, the next step is to characterize the Hamiltonian of a π-electron in atomic potential, which is given by the following equation:

$$H = \frac{\hbar}{2m}\Delta + \sum_{\mathbf{R}} V(\mathbf{r}-\mathbf{R}) + V(\mathbf{r}-\mathbf{R}+\boldsymbol{\delta}_j) \tag{8}$$

$V(\mathbf{r}-\mathbf{R})$ and $V(\mathbf{r}-\mathbf{R}+\boldsymbol{\delta}_j)$ correspond respectively to the potential induced by the nuclei from sublattice A and B. We can apply this Hamiltonian to $\phi(\boldsymbol{r})$. As represented in equation 9, the Hamiltonian can be divided into a atomic orbital part H^a and a perturbation part ΔU_j which comes from all other atoms.

$$H\phi^{(A)}(\mathbf{r}) = [\frac{\hbar}{2m}\Delta + V(\mathbf{r})]\phi^{(A)}(\mathbf{r}) + [V(\mathbf{r}+\boldsymbol{\delta}_j) + \sum_{\mathbf{R}\neq 0} V(\mathbf{r}-\mathbf{R}) + V(\mathbf{r}-\mathbf{R}+\boldsymbol{\delta}_j)]\phi^{(A)} \tag{9}$$

The first part is the orbital part. The eigenvalue of orbital Hamiltonian H^a is called the onsite energy and is equal to ϵ^A. The second part of the equation can be seen as a perturbation part ΔU_A due to the potential from all the other atoms. Consequently, this

equation can be simplified into $[\epsilon^A + \Delta U_A]\phi^{(A)}(\overrightarrow{r})$. The same result can be obtained by applying the Hamiltonian to $\phi^{(B)}(\mathbf{r} + \overrightarrow{\delta_j})$:

$$H\phi^{(B)}(\mathbf{r}) = (H^a + \Delta U_B)\phi^{(B)}(\mathbf{r}) \tag{10}$$

All the onsite energies are equal to ϵ_o. Indeed, the atoms have the same electronic configuration. For simplification purposes, ϵ_o is considered to be equal to 0. Now, two parameters, A and B, from equation 5 have to be determined. The time independant Schrödinger equation after multiplying by $\Psi^*(\boldsymbol{r}, \boldsymbol{k})$ gives:

$$(A^*, B^*)H_k \begin{pmatrix} A \\ B \end{pmatrix} = E(A^*, B^*)S_k \begin{pmatrix} A \\ B \end{pmatrix} \tag{11}$$

with,

$$H_k = \begin{pmatrix} \Psi^{(A)*}(\mathbf{r},\mathbf{k})H\Psi^{(A)}(\mathbf{r},\mathbf{k}) & \Psi^{(A)*}(\mathbf{r},\mathbf{k})H\Psi^{(B)}(\mathbf{r},\mathbf{k}) \\ \Psi^{(B)*}(\mathbf{r},\mathbf{k})H\Psi^{(A)}(\mathbf{r},\mathbf{k}) & \Psi^{(B)*}(\mathbf{r},\mathbf{k})H\Psi^{(B)}(\mathbf{r},\mathbf{k}) \end{pmatrix} \tag{12}$$

and

$$S_k = \begin{pmatrix} \Psi^{(A)*}(\mathbf{r},\mathbf{k})\Psi^{(A)}(\mathbf{r},\mathbf{k}) & \Psi^{(A)*}(\mathbf{r},\mathbf{k})\Psi^{(B)}(\mathbf{r},\mathbf{k}) \\ \Psi^{(B)*}(\mathbf{r},\mathbf{k})\Psi^{(A)}(\mathbf{r},\mathbf{k}) & \Psi^{(B)*}(\mathbf{r},\mathbf{k})\Psi^{(B)}(\mathbf{r},\mathbf{k}) \end{pmatrix} \tag{13}$$

The eigenvalues given by E from equation 11, are obtained by solving the secular equation:

$$det[H_k - ES_k] = 0 \tag{14}$$

After resolution that is described in annex 10.1, equation 14 becomes:

$$det \begin{bmatrix} E & tf^*(k) \\ tf(k) & E \end{bmatrix} = E^2 - t^2 f^2(k) = 0 \tag{15}$$

with t, called the hopping parameter. This parameter is due to the interaction between neighbouring atoms and is a constant approximately equal to $2.7 - 3eV$. Its expression is given in equation 94 from annex 10.1 Consequently, the eigenvalues of the Hamiltonian are:

$$\boxed{E = \pm t\sqrt{1 + 4cos\frac{\sqrt{3}k_x a}{2}cos\frac{k_y a}{2} + 4cos^2\frac{k_y a}{2}}} \tag{16}$$

with k_x and k_y, the momentum components of $\mathbf{k}$ in the x and y directions. The "+" and "−" are associated respectively to the conduction and the valence bands. Figure 3 represents the band structure of pristine graphene.

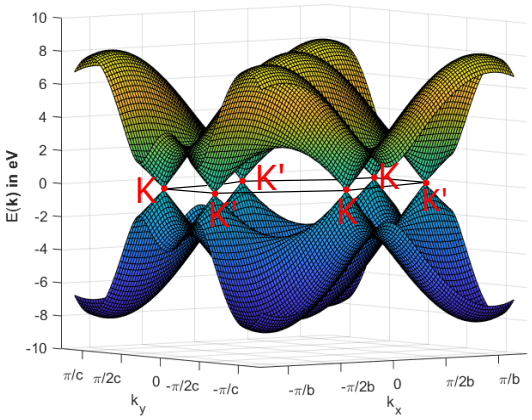

Figure 3: Energy dispersion in function of the wavevector with $a_{cc} = 0.142$, the distance between two carbon atoms, $b = \frac{a_{cc}}{2}$ and $c = \frac{\sqrt{3}a_{cc}}{2}$.

For undoped graphene, as each carbon atom contributes to one π-electron, the valence band is filled and the conduction band is empty. The Fermi Level is located at the intersection between the valence and conduction bands. The two bands are connected at the six K and K' points, which explains the name of gapless semiconductor or semimetal to graphene. Close to the points K and K', the energy dispersion can be described by

$$E = \pm\hbar v_f |\mathbf{q}| \tag{17}$$

with $v_f = \frac{3ta}{2\hbar} = 10^6$m/s, the Fermi velocity and $\mathbf{q}$, the translation of the momentum vector $\mathbf{k}$ at one of the Dirac points, equal to $\mathbf{k}$-$\mathbf{K}$.

Close to these points, the energy dispersion is linear in opposition to the usual $2D$ gas with a parabolic energy dispersion. In the case of graphene, the charge carriers have a zero effective mass. At low energies, they behave like relativistic particles, described by the Dirac-Weyl equation where the speed of light is replaced by the Fermi velocity and with a zero mass [10]. Consequently, developing the Hamiltonian around the Dirac points leads to the following effective Hamiltonian:

$$H = -\hbar v_f (\eta q_x \sigma_x + q_y \sigma_y) \tag{18}$$

with $\sigma = (\sigma_x, \sigma_y)$, the Pauli matrices and $\eta = \pm$. The "+" and "− " refer to a wavefunction close to the Dirac points K and K' respectively. However, in the case of graphene, σ does not operate on the real spin of the charge carriers but on the so-called pseudospin, which comes from the presence of the two sublattices. By analogy to the real spin, electrons can reside on A and B sublattices as the real spin-up and spin-down. The operator σ characterises the repartition of the wavefunction between the two sublattices. Consequently, the hopping of electrons between A and B sublattices is represented by a rotation of the pseudo-spin.

By solving the 2D Dirac equation for a massless particle:

$$-\hbar v_f (\eta q_x \sigma_x + q_y \sigma_y) \Psi_q^\eta = E \Psi_q^\eta \tag{19}$$

the wavefunction of the Hamiltonian is represented by the spinors [6]:

$$\Psi_q^\eta = \begin{pmatrix} \Psi_{q,A}^\eta \\ \Psi_{q,B}^\eta \end{pmatrix} = \frac{1}{\sqrt{2}} \begin{pmatrix} \pm e^{-\eta i \phi} \\ 1 \end{pmatrix} \tag{20}$$

with ϕ, given by $\arctan \frac{q_y}{q_x}$. The "$\pm$" outside the exponential corresponds to the conduction and valence bands respectively. As for the real spin, the wavefunction $(1,0)^T$ refers to the A sublattice (pseudospin up)and the $(0,1)^T$ refers to the B sublattice (pseudo spin down). Graphene is composed of carbon, consequently, both wavefunctions contribute equally to the total wavefunction and only differ by a phase ϕ [11].

To conclude this section, the density of state in pristine graphene can be given by [5]:

$$\rho(E) = \frac{2A_c}{\pi} \frac{|E|}{v_f^2} \tag{21}$$

with A_c, the unit cell, equal to $\frac{3\sqrt{3}a^2}{2}$.

1.3 Electronic Properties

1.3.1 Backscattering in graphene

The purpose of this section is to introduce two important parameters and their implication in the electronic properties of graphene: the Berry's phase and the helicity.

1.3.1.1 Berry's Phase

Equation 20 represents a spinor and, as for all spinors, a rotation of 2π leads to an accumulated phase of π. In the case of graphene, it means that if the vector $\mathbf{q}$ is forced to realize a full circle around the Dirac point at a constant energy, the wavefunction changes its sign. This phase is commonly called the Berry's phase that will be explained in more details in the section 2. The Berry's phase can explain the quantum interference in graphene, which can be destructive or constructive. The left part of figure 4 represents the interference between two electron paths. Due to the additional phase, π, the two paths can end up in opposite phases if there are no spin-orbit interactions and no scattering between valleys. This results in the observation of an anti-weak localisation (AWL) in graphene. On the other hand, when intervalley scatterings occur (due to ripples or large defects for example), the Berry phase leads to constructive interferences that are responsible for the weak localisation (WL). Then, depending on the scattering mechanisms, both WL and AWL can occur [12]. A way to measure the WL and AWL is by applying a magnetic field. The right part of the figure 4 gives the transition between the weak and anti-weak localisation in graphene from Ref. [13] due to a change of the electron density.

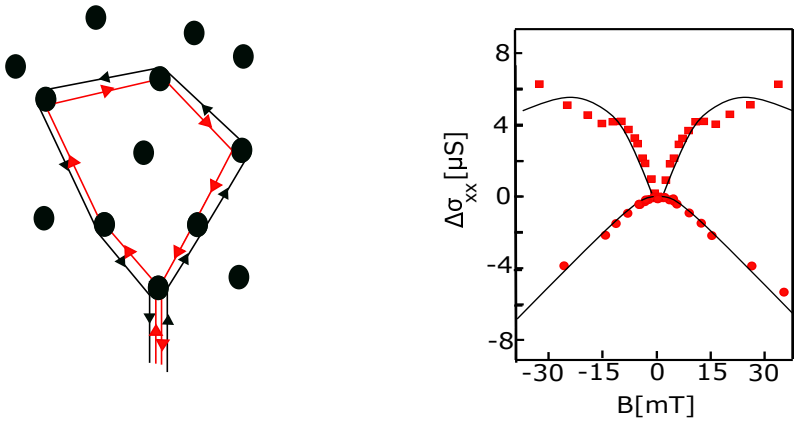

Figure 4: On the left part of the figure, a schematic representation of the localization in graphene. The dark points represent impurities. In graphene, it is expect to obtain a destructive interference due the Berry's phase of π. On the right , figure modified from Ref. [13] that shows, for the up-curve, the weak localization and for the down curve, the anti-weak localization. The points are obtained at a temperature of $27K$. The second curve is obtained by lowering the electron density.

1.3.1.2 Helicity

The helicity(which is the same as chirality in the case of massless relativistic fermions) is an operator described as [5, 6]:

$$h = \frac{1}{2}\boldsymbol{\sigma} \cdot \frac{\mathbf{q}}{|\mathbf{q}|} \tag{22}$$

It corresponds to the projection of the pseudo-spin onto the direction of propagation. The sign of the helicity is given in figure 5. In the case of Dirac Hamiltonian with no mass term, this quantum number is relevant to describe the wavefunction since the helicity and the Hamiltonian commute. A positive (negative) helicity means that the momentum and the pseudospin are (anti-)parallel. The sign of the helicity changes from K to K'. Note that the helicity is only correct when the massless Dirac Hamiltonian is a good approximation, which is not the case for high energy.
When intravalley events occur, the conservation of the helicity forbids the backscattering leading to, for example, the Klein tunneling [14]. This is explained by the necessity to flip the pseudo-spin to allow the backscattering process. However, when intervalley scattering occurs, backscattering is allowed as the helicity changes its sign leading to a conservation of the pseudo-spin.

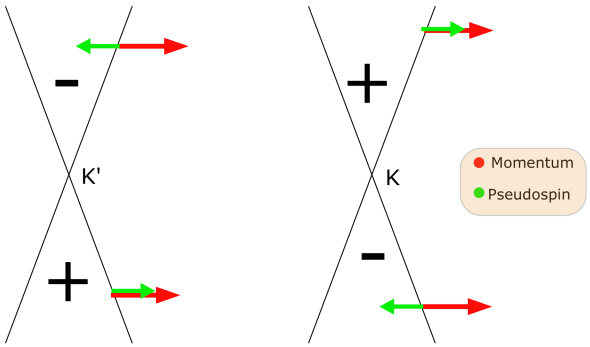

Figure 5: In green, the pseudospin. In red, the direction of the momentum. A positive helicity occurs when both are parallel and a negative helicity when both are anti-parallel.

1.3.2 Ambipolar electric field effect

The density of charge carriers can easily be changed by using a Graphene-Field effect transistor (GFET). The most common GFET was realized on a Si/SiO_2 substrate which is represented in figure 6.

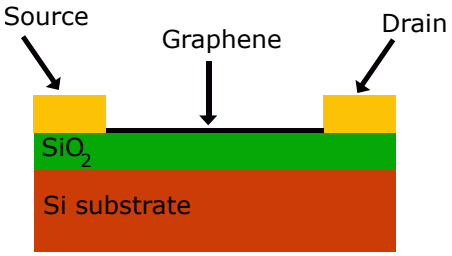

Figure 6: Side-view of a graphene-Field effect transistor realized on a Si/SiO_2 substrate.

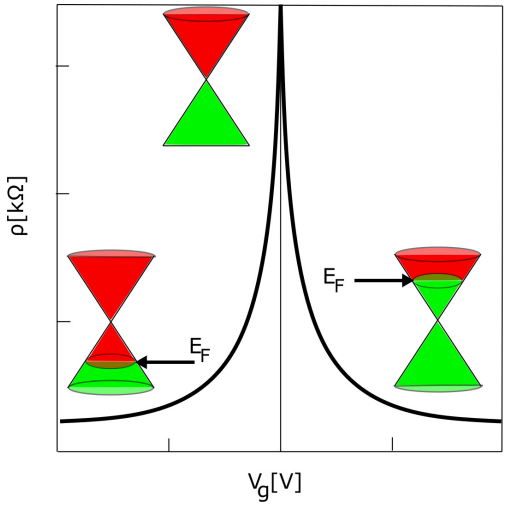

Figure 7: Ambipolar effect in graphene inspired from Ref. [15]. By changing the back gate voltage to tune the position of the Fermi level, the resisitivity increases until reaching a maximum value at $V_g = 0V$.

The silicon layer plays the role of the back-gate and by changing the back-gate voltage V_g, the position of the Fermi Level can be tuned. Indeed, as represented in figure 7, the resistivity ρ increases when the Fermi level is in the valence band (conduction band) and V_g is increased (decreased). When the Fermi level is located between the valence band and the conduction band, the resistivity reaches a maximum that represents the Dirac point [16]. In undoped graphene, the position of the Dirac point has to be at zero V_g. However, when graphene is in proximity with negatively charged impurities, the Dirac point is shifted toward negative voltage. When graphene is in proximity with positively charged impurities, the Dirac point is shifted toward positive voltage.

Using this kind of measurement, the mobility of the charge carriers can be calculated. The Drude model can be used and is valid for the linear part of the dispersion relation.

The mobility is given by the following equation:

$$\mu_{=}\frac{1}{e}\left|\frac{d\sigma}{dn}\right| \tag{23}$$

with n the charge carrier density which can be expressed as a function of the back-gate voltage:

$$n = \alpha(V_g - V_{go}) \tag{24}$$

with V_{go}, the gate potential at Dirac's point and α, the gate lever-arm:

$$\alpha = \frac{\epsilon_o}{e}\frac{\epsilon_{SiO_2}}{d_{SiO_2}} \tag{25}$$

with d_{SiO_2} and ϵ_{SiO2}, the thickness and the permittivity of the dielectric layer.

1.4 Graphene Nanoribbons

The presence of edges leads to strong effects for the low energy spectrum of the π-electrons. We can identify two different edges: "armchair" and "zigzag", which are represented on figure 8.

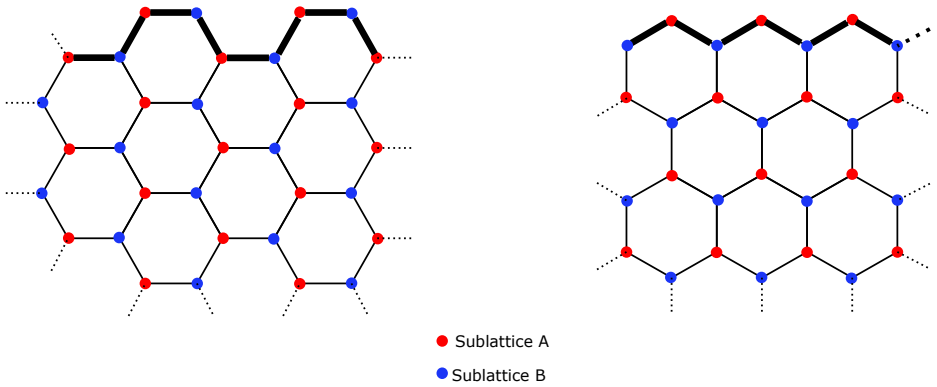

Figure 8: This figure represents on the left, an armchair nanoribbon of graphene and on the right, a zigzag nanoribbon of graphene. The upper bold lines represent the edges of the graphene nanoribbon

As shown in figure 8, the zigzag nanoribbon edge is composed of one type of carbon atoms (A or B). The armchair nanoribbon is formed by two different types of carbon atoms (A and B). These edges lead to localised edge states close to the Fermi level in the case of zigzag nanoribbons, but which are absent in the case of armchair nanoribbons [17]. In the next sections, the band structure for these two kind of nanoribbons will be described by using the nearest-neighbor tight-binding model.

1.4.1 Zigzag nanoribbons

In this case, as represented in figure 8, atoms of each edge are of one single type, A or B. Figure 9 represents the band structure of the zigzag nanoribbon obtained by using the nearest-neighbor tight binding model in Kwant. In this case, the width is described by N, which represents the number of zigzag lines. As can be seen, at $k = \pm\pi$, the valence band and conduction band are completely degenerated [18]. In the intervals $[K, \pi]$ and $[-\pi, K']$, the two bands are partially flat and are located close to the Fermi level.

1.4.2 Armchair nanoribbons

Figure 10 represents the band structure of armchair nanoribbons with different width. The top of the valence band and the bottom of the conductive band are at $k = 0$. As shown, depending on the width, the armchair nanoribbon behaves like a semiconductor

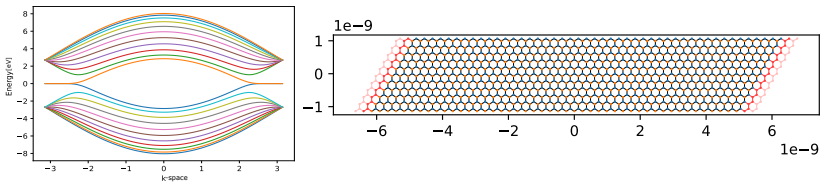

Figure 9: On the left the band structure of zigzag graphene nanoribbon obtained by using Kwant with the hopping parameter,t, equal to $2.8eV$. The path in the Brillouin zone corresponds to $K \rightarrow \Gamma \rightarrow K'$ with $k_y = 0$. This nanoribbon, with a width and a length composed of respectively 22 and 102 atoms, is represented on the right.

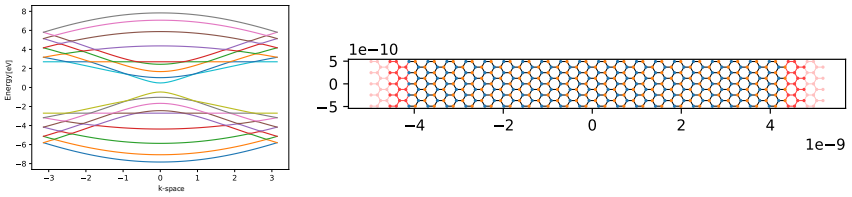

(a)

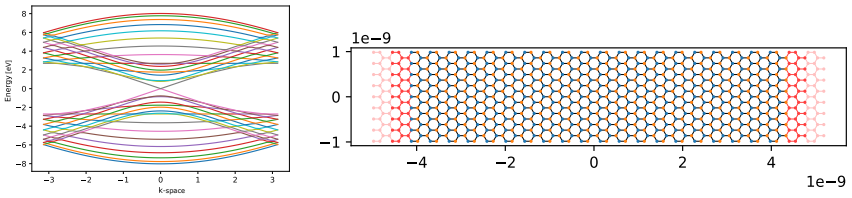

(b)

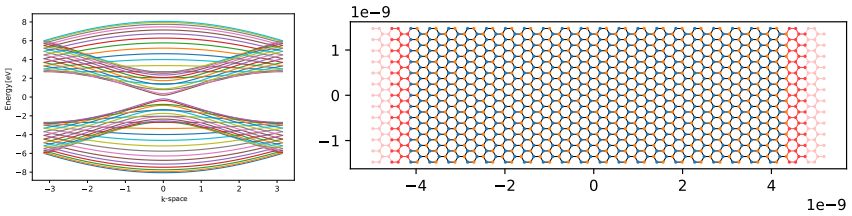

(c)

Figure 10: Band structures and systems of armchair nanoribbons with (a)$N = 9$,(b)$N = 17$,(c)$N = 25$ obtained by using Kwant with the hopping parameter,t, equal to $2.8eV$. The path in the Brillouin zone corresponds to $K \rightarrow \Gamma \rightarrow K'$ with $k_y = 0$. A band gap is opened when the number of two carbons sites is not equal to $3M - 1$ with M, an integer.

or a semi-metal. The band gap in the case of semiconductor reduces when the width increases. The energy spectrum is given by the following equation [17, 18]:

$$E_{\pm} = \pm t\sqrt{1 + 4cos(p)cos(\frac{k}{2}) + 4cos^2(p)} \tag{26}$$

with p= $\frac{r}{N+1}\pi$ and $r = 1, ..., N$. N is used to define the number of atoms in the width. It represents the number of two-carbon sites. As we can see, when $N = 3M - 1$ with M, an integer, the nanoribbon is a semi-metal. Otherwise, it is a semi-conductor.

1.5 Effect of the magnetic field

In this section, the effect of the magnetic field on the electronic transport properties of graphene will be developed. Firstly, the classical and integer quantum hall effect will be presented. Finally, the quantum Hall effect in graphene will be explained.

1.5.1 Classical Hall effect

Consider a bi-dimensional electron gas in a perpendicular magnetic field $\mathbf{B} = (0, 0, B)$. Due to the Lorentz force, there is an accumulation of charges at the edges. This accumulation results in a potential difference V_H, called Hall potential that creates an electric field perpendicular to the direction of the current and the magnetic field. It opposes the displacement of the charge carriers and increases until compensating the Lorentz force caused by the magnetic field. The total force is given by the following equation [19]:

$$\mathbf{F} = q(\mathbf{E} + \mathbf{v} \wedge \mathbf{B}) - m\frac{\mathbf{v}}{\tau} \tag{27}$$

with the last term, the friction term characterized by a collision time τ. The situation is represented in figure 11.

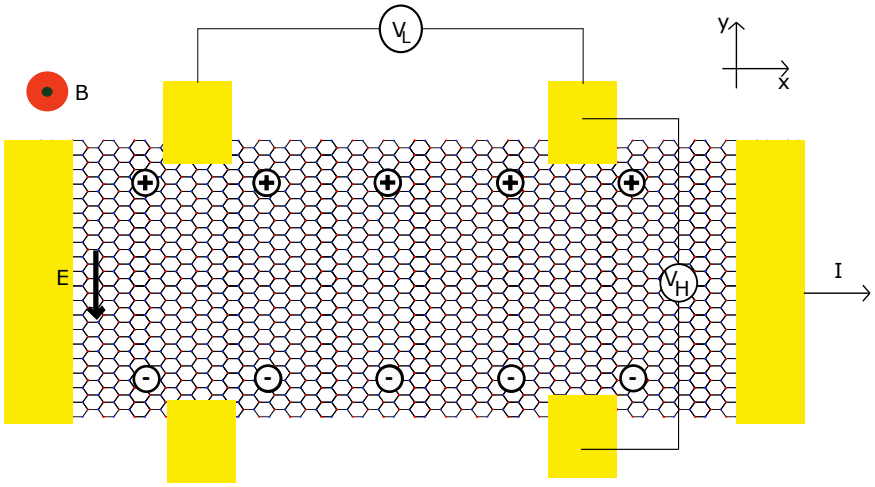

Figure 11: Schematic representation of a Hall Bar. A current I flows in the x-direction. A magnetic field $\boldsymbol{B}$ is applied in the z-direction resulting in a potential difference V_H.

The equilibrium state, $F = 0$, is reached when the Lorentz force due to the magnetic field is equal to the force resulting from the created electric field. To analyze this effect, the Ohm's law, $\mathbf{J} = \sigma\mathbf{E}$, will be used. This law can also be written as $\mathbf{E} = \rho\mathbf{J}$ with ρ and σ are respectively called resistivity and conductivity tensor. They are given by [19]:

$$\rho = \begin{pmatrix} \rho_{xx} & \rho_{yx} \\ \rho_{xy} & \rho_{yy} \end{pmatrix} \text{ and } \sigma = \rho^{-1} = \begin{pmatrix} \sigma_{xx} & \sigma_{yx} \\ \sigma_{xy} & \sigma_{yy} \end{pmatrix} \tag{28}$$

ρ_{xx} is called the longitudinal resistivity and ρ_{xy} is called the Hall resistivity. The equation 27 can be decomposed in the x-direction and the y-direction:

$$E_x = \frac{mv_x}{q\tau} - v_y B \text{ and } E_y = \frac{mv_y}{q\tau} + v_x B \tag{29}$$

There is not any current in the y-direction which corresponds to $v_y = 0$. The current density can be obtained by recalling that $J_{x/y}$=qnv$_{x/y}$ with n, the carrier density. Consequently, by introducing the Drude conductivity, $\sigma_0 = \frac{q^2 n\tau}{m}$ and the expression $\omega_c = \frac{Bq}{m}$, the Ohm's law becomes:

$$\begin{pmatrix} E_x \\ E_y \end{pmatrix} = \frac{1}{\sigma_0}\begin{pmatrix} 1 & \omega_c\tau \\ -\omega_c\tau & 1 \end{pmatrix}\begin{pmatrix} J_x \\ J_y \end{pmatrix} = \begin{pmatrix} \rho_{xx} & \rho_{yx} \\ \rho_{xy} & \rho_{yy} \end{pmatrix}\begin{pmatrix} J_x \\ J_y \end{pmatrix} \tag{30}$$

$$\begin{pmatrix} J_x \\ J_y \end{pmatrix} = \frac{\sigma_0}{1+\omega_c\tau}\begin{pmatrix} 1 & -\omega_c\tau \\ \omega_c\tau & 1 \end{pmatrix}\begin{pmatrix} E_x \\ E_y \end{pmatrix} = \begin{pmatrix} \sigma_{xx} & \sigma_{yx} \\ \sigma_{xy} & \sigma_{yy} \end{pmatrix}\begin{pmatrix} E_x \\ E_y \end{pmatrix} \tag{31}$$

As shown by the previous equation, we can determine the longitudinal resistivity:

$$\rho_{xx} = \frac{1}{\sigma_0} = \frac{m}{q^2 \tau n} \tag{32}$$

with n, the density of the charge carriers. Consequently, the longitudinal resistance is given by:

$$R_{xx} = \frac{V_x}{I_x} = \frac{E_x L}{J_x W} = \rho_{xx} L/W \tag{33}$$

with L and W respectively the length and the width of our $2D$ sample. The Hall resistivity is :

$$\rho_{xy} = \frac{B}{qn} \tag{34}$$

Consequently, the Hall resistance is given by :

$$R_H = \frac{V_H}{I_x} = \rho_{xy} \tag{35}$$

The Hall resistance is independent of the geometry of the sample. By measuring the Hall resistance in graphene, information about the carrier density and also about the type of carriers that contribute to electronic transport can be obtained.

1.5.2 Integer Quantum Hall Effect in semiconductor-based 2D electron systems

In 1980, the effect called the Integer Quantum Hall effect was discovered by Klitzing,Dorda and Pepper [20] on a classical 2D electronic system . They found that, when a sufficiently high magnetic field **B** is applied, the Hall resistance exhibits plateaus for certain values of **B**. In the same regions, the longitudinal resistance vanishes and possesses peaks of non-zero resistance when the Hall resistance changes from one plateau to another. This is represented in figure 12.

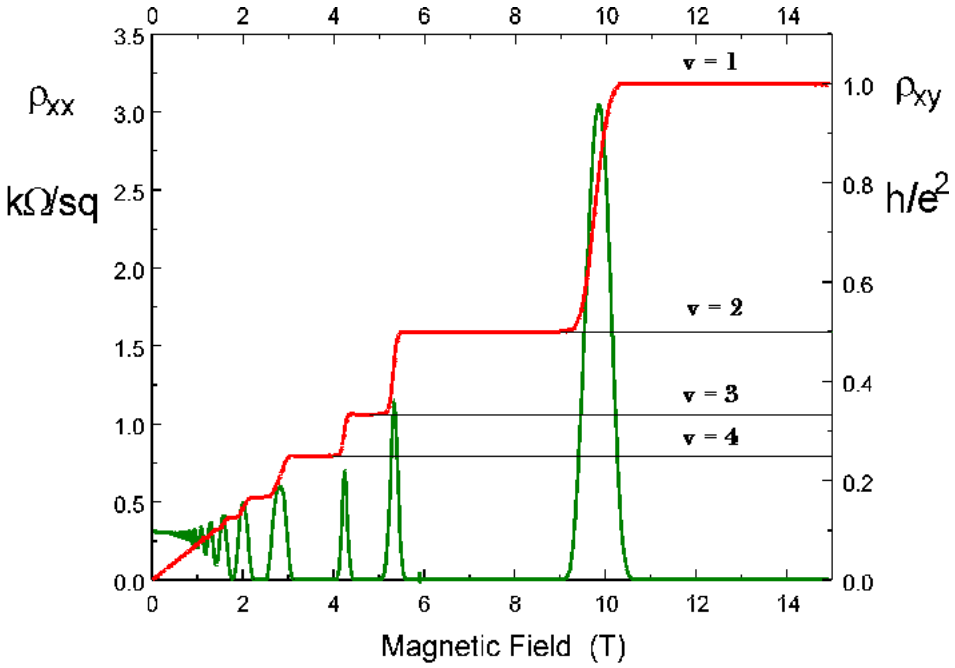

Figure 12: Typical measurement of the integer Quantum Hall effect from Ref. [21]. The Hall resistance presents plateaus for some intervals of magnetic field. The longitudinal resistance vanishes in the same intervals.

The plateaus are located at:

$$\rho_{xy} = \frac{1}{\nu}\frac{h}{e^2} \tag{36}$$

with ν, an integer equal to 1,2,3,... .

1.5.2.1 Electrons in a magnetic field: Landau Levels

When a magnetic field is applied, the electrons will execute a circular orbit with a frequency of

$$\omega_c = |\frac{eB}{m}| \tag{37}$$

To treat this problem in quantum mechanic, the Peirls substitution will be used, which allows to introduce the magnetic field in the Hamiltonian [19]:

$$H(\mathbf{p}) \rightarrow H(\Pi = \mathbf{p} + q\mathbf{A}) \tag{38}$$

with $\mathbf{A}$, the vector potential equal to $(0, Bx, 0)$, if a magnetic field is applied in the z-direction. In this case, the Hamiltonian for free electrons (the potential is assumed to be 0) is:

$$H = \frac{\hbar^2}{2m}(\mathbf{p} + e\mathbf{A})^2 \tag{39}$$

which gives:

$$H = -\frac{\hbar^2}{2m}\nabla^2 - \frac{ie\hbar Bx}{m}\frac{\delta}{\delta y} + \frac{(eBx^2)}{2m} \tag{40}$$

The eigenvalues of this Hamiltonian are:

$$E_n = \hbar\omega_c(n + \frac{1}{2}) \tag{41}$$

with $n = 0, 1, 2, ...$. These eigenstates are called Landau levels (LLs) and are represented in figure 13

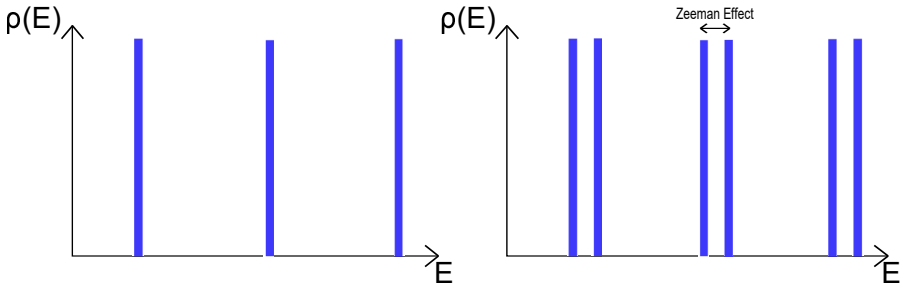

Figure 13: Effect of dispersion under a high magnetic field with and without spin-degeneracy.

Consequently, the energy spectrum, which was a constant for $2D$ electron gas, becomes quantized. We only expect to obtain a real discretization of the LLs at a high magnetic field, which allows electrons to realize a complete orbit [19]. The number of states in each LLs is:

$$n_B = \frac{eB}{h} \tag{42}$$

Consequently, the number of filled LLs is

$$\nu = \frac{n_e}{n_B} = \frac{hn_e}{eB} \tag{43}$$

Where ν is called the filling factor. When it is an integer, it represents the number of LLs filled. By increasing the magnetic field, we increase the space between two LLs and also the number of state per LLs. Equation 43 is obtained without considering the spin of

the electrons. At a low magnetic field, the Zeeman splitting is not enough to obtain two well separated LLs. This situation, neglecting the spin spilling is represented in figure 13. Only the even filling factors appear in equation 43. On the contrary, when a high magnetic field is applied, the degeneracy can be completely lifted via Zeeman interaction. Well separated LLs can be obtained.

1.5.2.2 Edge state and effect of disorder

In a classical description, the electrons experience an orbital motion. However, close to the edges, the orbit must collide with the boundaries. Then, the electrons bounce back to the sample leading to a skipping motion in which particles move along the one-dimensional boundary and in one direction. In a quantum description, when electrons are close to the edges, they experience a potential that increases slightly when they are closer and closer to the edges. This induces the upward bending of the LLs close to the edges [22]. When the Fermi Level is in the bulk of the band gap, it crosses the LLs at the edges as represented in figure 14 As shown in this figure, the number of states at each edge

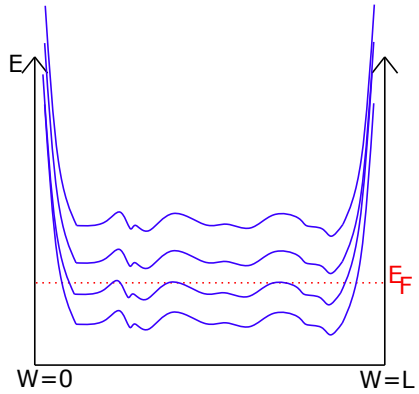

Figure 14: Bending of the Landau Levels close to the edge due to the potential experimented by electrons leading to the edges states when the Fermi Level is in band gap of the bulk. The red dotted line represents the Fermi Level and the blue line, the Landeau Level.

corresponds to the number of filled LLs, ν leading to the expression of the Hall resistance in equation 36. However, the presence of edge states can not explain how the Fermi Level can be maintained between two LLs and so, can not explain the presence of plateau in the Hall resistance. Indeed, it is impossible to keep the Fermi Level into the band gap when the density of electrons is changing. This is why the presence of disorder is necessary.

Without disorder, the LLs are present as Dirac-function (see figure 13). When disorder is present, the LLs broaden as shown in figure 15.

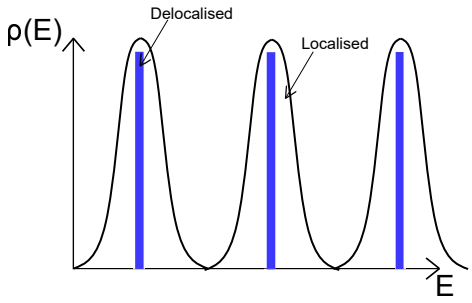

Figure 15: Effect of disorder on the Landau Levels. The blue lines represent the delocalised states and the rest represents the localised states.

The states that are due to the disorder, are localised. This means that the electrons that occupy these states can not participate in the electrical transport. The blue lines in figure 15 represents the delocalised states that are the only one, in the bulk, that can contribute to the transport. The localised states can keep the Fermi Level between two delocalised states and contrary to these localised states in the bulk, the edge states are delocalised and are not backscattered. They can contribute to the transport of charges leading to the presence of plateau in the Hall resistance [22].

1.5.3 Integer Quantum Hall Effect in graphene

In the case of graphene, the charge carriers behaves like massless Dirac fermions at low energy characterized by the Hamiltonian in a magnetic field around K given by [23]

$$H_K = v_f(\mathbf{p} + e\mathbf{A}) \cdot \sigma \tag{44}$$

and around K' given by

$$H_K = -v_f(\mathbf{p} + e\mathbf{A}) \cdot \sigma* \tag{45}$$

The LLs in this case are:

$$E_{LL} = \pm\hbar\omega_c\sqrt{n} = \pm v_f\sqrt{2\hbar enB} \tag{46}$$

with $n = 0, 1, 2, ...$. The same spectrum is obtained around K and K' leading to the degeneracy of each state of 2. As for the previous case, the energy spectrum becomes discrete. This result is by many aspects different than the one obtained for classical $2D$ electron gas. Some differences can be detected. The first one is the presence of a zero-energy state which is shared by electron and hole. The second is the energy separation between two LLs which does not growth linearly with the number of filled LLs. The third one is that there are positive and negative LLs which are respectively for electrons in the conduction band and holes in the valence band.

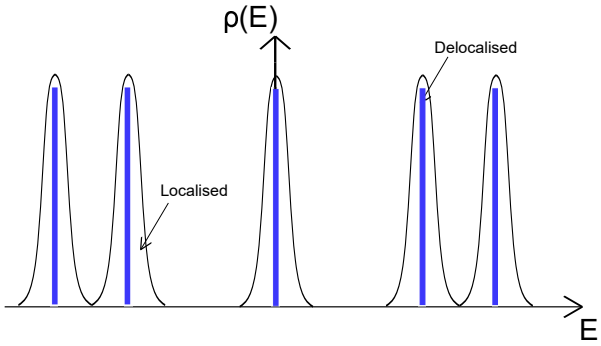

Figure 16: Energy dispersion of the graphene under a high magnetic field. The blue lines represent the delocalised states and the rest represent the localised states.

For low magnetic field, as for the previous case, the Zeeman splitting is to small to obtain two well-separated LLs for each spin. Consequently, the number of filled LLs is double. The filling factor, at low energy, is consequently 2 (Valley)+2 (spin)=4.

The new expression for the LLs leads to the quantization of the Hall resistance as follows Ref. [23]:

$$\rho_{xy} = \frac{h}{e^2}\frac{1}{4(n+1)} \tag{47}$$

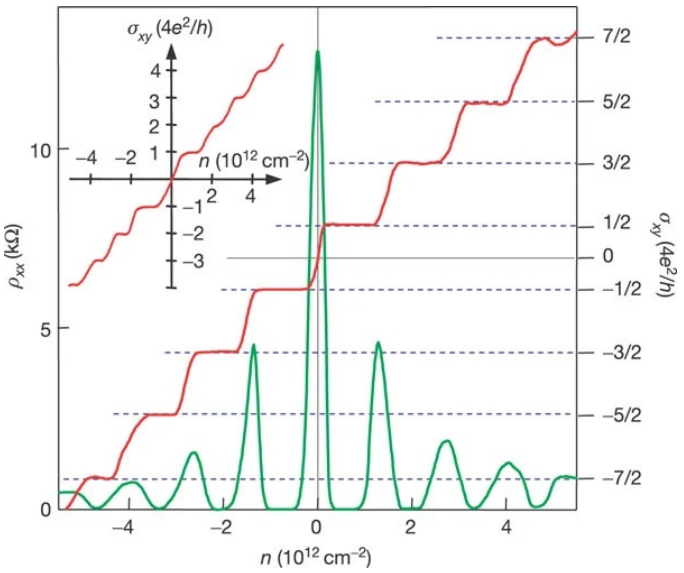

Figure 17: Typical measurement of the Quantum Hall effect from Ref.[23]. The Hall resistance presents plateaus for some intervals of magnetic field. The longitudinal resistance vanishes in the same intervals.

2 Topological Insulator

Topology is initially used in mathematics to define properties of three-dimensional objects. These properties are described by integers called topological invariants. The most famous example is the Gauss-Bonnet theorem given by the following equation:

$$\frac{1}{2\pi}\oint KdS = 2 - 2g \equiv n \tag{48}$$

with K, the Gauss curvature defined as $\kappa_1\kappa_2$, the two main curvatures at a given point of a surface, g the number of holes in the object (1 for a torus, 0 for a sphere, see figure 19), called the genus, and n the Euler characteristic.

The two main curvatures in K are obtained by slicing the surface of an object with a plane perpendicular to the normal plane at a given point. The intersection between the surface and this plane forms a curve. In every directions, a curvature is obtained. The largest and smallest ones are selected and are the two principle curvatures as represented in figure 18.

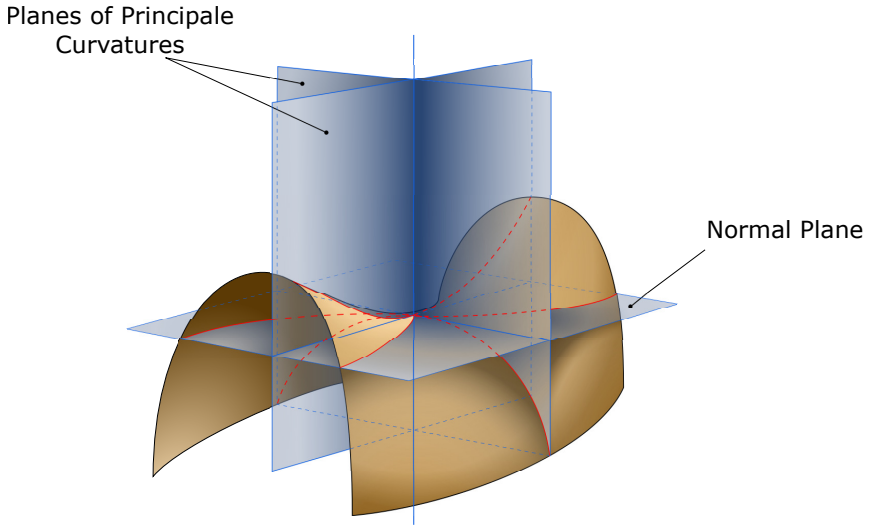

Figure 18: Two main curvatures that define the Gaussian curvature in equation 48.

The integral of the Gauss curvature over the whole surface divided by 2π is always an integer, n. This number represents a topological invariant, which means that it remains unchanged under continuous and smooth deformations of the object [24]. It allows to topologically differentiate a torus from a sphere. A simple smooth deformation from one to the other is not possible without closing the gap [24, 25] while it is possible between a torus and a cup. This is represented in figure 19.
In solid state physics, topology is used to tell the difference between two insulators. In an insulator, there are two different well-separated bands: the valence and conductive bands. In this context, the valence bands will be topologically characterized. In analogy with the example given before, two insulators are topologically equivalent if the band structure can be changed from one to the band structure of the other by smoothly changing the Hamiltonian without closing the gap. On the other hand, two topologically nonequivalent insulators that are put into contact lead to the creation of a new class of material: **the topological insulators**. These materials are insulators in the bulk while possessing a conducting channel at the interface with the other material due to the necessity to close the gap (example: change from a torus to a sphere required to close the hole leading to a change in the topology) [26, 27].

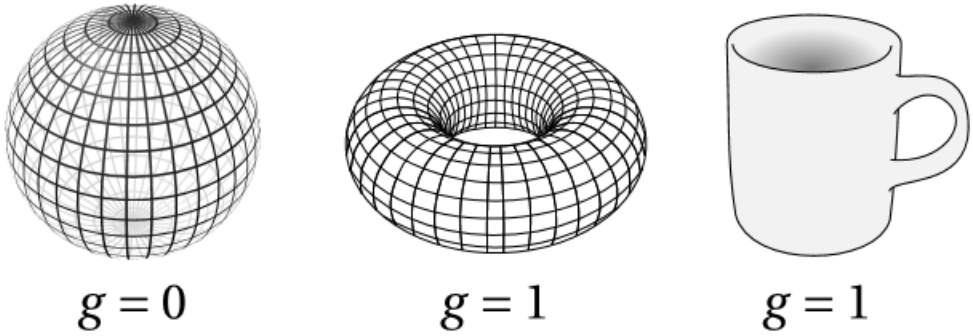

Figure 19: A donut and cup have the same topolgocial invariant,$n = 0$. A sphere with a genus, g, of 0, has a topological invariant of $n = 1$.

In analogy with equation 48 with the Euler characteristic, n, the parameter used to describe each insulator topologically is the Chern Number, C, a topological invariant that depends on the Berry curvature, $\boldsymbol{\Omega}$.

In this section, the Berry's phase and the Berry's curvature will be described to understand the direct link between topology and an insulator. Then, the integer quantum Hall effect(IQHE), which has already been presented in the previous section, will be explained topologically. Indeed, the presence of a magnetic field will change the topology of the material. The Haldane model [2], also called the first topological insulator, will then be developed. Haldane discovered that the only requirement to obtain a non-trivial insulator and, by consequence, to obtain edge states, is to break the time-reversal symmetry and not to apply a magnetic field. Then, the quantum spin Hall effect in graphene predicted by Kane and Mele [3] will be explained. Both these models are purely theoretical in the case of graphene and can not be observed directly but has been experimentally shown in other materials. For example, the quantum spin Hall effect was observed in HgTe Quantum Wells [28] or in monolayer of WTe_2[29]. However, they will be important to understand the case that we are interested in: the quantum anomalous Hall effect in graphene induced by magnetite nanoparticles.

2.1 Berry's Phase and Curvature

In this section, the Berry's phase and the Berry's curvature will be presented. Firstly, the general form of the phase will be given. Then, a short classical analogy, the Hannay angle, will be described. Finally, the role of the Berry's phase and curvature in the band structure will be detailed to understand the impact of this new phase in the topological description of insulator.

2.1.1 General form of the Berry's phase

Consider an initial Hamiltonian $H_i(\mathbf{R})$ with an eigenstate $\psi_i(\mathbf{R} = \mathbf{R}_i)$. The vector $\mathbf{R}$ represents a parameter space, which can be real space ($\mathbf{r}$), reciprocal space ($\mathbf{k}$), a magnetic field, a nuclear coordinate, etc. This vector is slowly changed into a new vector $\mathbf{R} = \mathbf{R}_f$ during a time T. When the new vector is equal to the initial one, the new eigenstate is equal to the initial one with an additional phase ϕ as represented in the following equation [30, 31]:

$$|\psi_f(\mathbf{R} = \mathbf{R}_f, t_f = T)\rangle = e^{i\phi} |\psi_i(\mathbf{R} = \mathbf{R}_i, t_i = 0)\rangle \tag{49}$$

Initially, the phase ϕ was equal to the dynamical phase obtained by solving the time dependant Schrödinger equation and that depends on the energy, as shown in the following

equation [32, 30]

$$\phi_{dynamic} = \int_0^T \varepsilon[\mathbf{R}]dt \tag{50}$$

In 1984, Berry proposed a new phase that appears when a system undergoes a cyclic and adiabatic evolution [32] in a parameter space along a path C. The phase, called the geometrical phase, is added to the already known dynamical phase. Consequently, the phase described in equation 49 becomes [32, 30]

$$\phi = \oint_C i \langle \Psi_i(\mathbf{R}) | \Delta_{\mathbf{R}} | \Psi_i(\mathbf{R}) \rangle \cdot d\mathbf{R} - \int_0^T \varepsilon[\mathbf{R}]dt \tag{51}$$

The details of the calculation are given in the annex 10.2 . The first term is the geometrical phase, called the Berry's phase and usually noted γ. The second one is the dynamical phase. As shown in this equation, the Berry's phase only depends on the geometry of the path C and not on how long it takes to perform the change. This is the manifestation of the failure of a parallel transport around a closed path, called holonomy. In other word, this phase is associated with the connection to the space itself. This is why, $i \langle \Psi_i(\mathbf{R}) | \Delta_{\mathbf{R}} | \Psi_i(\mathbf{R}) \rangle$ is called the Berry's connection, which is gauge independent and is noted $A[\mathbf{R}]$. This parameter allows to connect the two points $\mathbf{R}$ and $\mathbf{R} + d\mathbf{R}$ in the parameter space [33].

By applying the Stoke theorem, a new notion is defined, the Berry's curvature, noted $\boldsymbol{\Omega}$:

$$\boldsymbol{\gamma = \oint_C \mathbf{A}[\mathbf{R}] \cdot d\mathbf{R} = \oint_S \Omega[\mathbf{R}] \cdot d\mathbf{S}} \tag{52}$$

with $\boldsymbol{\Omega}$ equal to $\nabla_{\mathbf{R}}$ x $\mathbf{A}[\mathbf{R}]$. The Berry's phase is completely defined by the Berry curvature which can be seen as the 'Gaussian curvature in the parameter space ' (see resemblance with equation 48). In analogy with the Gauss-Bonnet theorem, a topological invariant can be defined, called the Chern Number, an integer, and represented by [27, 26, 24, 34, 35]:

$$\boldsymbol{C = \frac{1}{2\pi} \oint_S \Omega[\mathbf{R}] \cdot d\mathbf{S}} \tag{53}$$

This invariant is close to the Euler characteristic. A non-zero Chern number has its origin in the curvature of the parameter space.

2.1.2 Classical Analogy: the Foucault Pendulum

The Berry's phase has a classical equivalent, called the Hannay angle [36]. The most famous example is the Foucault pendulum. Consider that a pendulum initially oscillates in a direction represented by the blue arrow in figure 20.

The pendulum is slowly displaced to avoid to affect the direction of oscillations and follows the trajectory represented by the dotted red line. As shown in the figure, when the pendulum realizes a close loop, A$\rightarrow$ B $\rightarrow$ C $\rightarrow$ A, the direction of oscillation undergoes a phase shift due to the curvature of the Earth. This is the classical demonstration of the Berry's phase. This phase depends only on the close loop and not on the time it takes to realise it.
The Hannay angle between the initial and the final direction is given by the integral of the Gaussian curvature over the surface delineated by the trajectory. In the case of a sphere, the Gaussian curvature is $\frac{1}{r^2}$ with r the radius.

2.1.3 Berry phase in Bloch Bands theory

In this part, the parameter space $\mathbf{R}$ will coincide with the Bloch vector $\mathbf{k}$. The domain where the vector varies is the Brillouin zone (BZ).

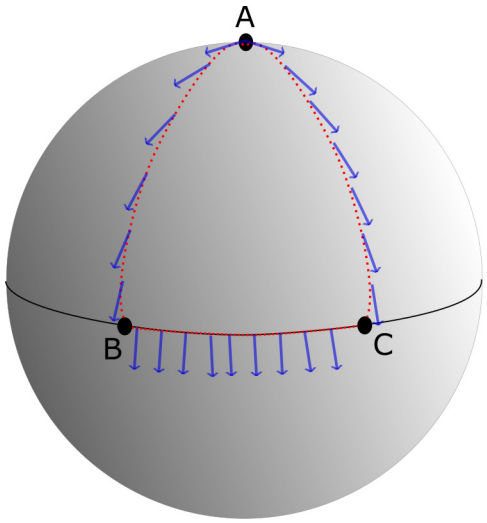

Figure 20: In red dotted line, the trajectory followed by a pendulum that oscillates in the direction of the blue arrows.

In a crystal structure, due to this periodic potential, it seems logical that the probability density varies in the same way in each unit cell. Consequently, the wavefunction of a charge carrier may be written as:

$$|\Psi_j(\mathbf{r})\rangle = e^{i\mathbf{k}\cdot\mathbf{r}}\,|u_j(\mathbf{r})\rangle \tag{54}$$

with u_j, a function that has the periodicity of the potential, j, the energy band index and $\mathbf{k}$ the wavevector in the first BZ. A reciprocal lattice vector, $\mathbf{G}$, can be defined that links two equivalent wavevectors from different unit cells of the crystal. In other words, $\mathbf{k}$ and $\mathbf{k'}$ are considered equivalent if

$$\mathbf{k} = \mathbf{k'} + m\mathbf{G} \tag{55}$$

with m, an integer.

Consider now a single and isolated band. By changing slowly $\mathbf{k}$(t) inside the BZ to explore the band, the Bloch state of a charge carrier will undergo a closed loop in the momentum space as represented in figure 21, which results in the apparition of a Berry's phase.

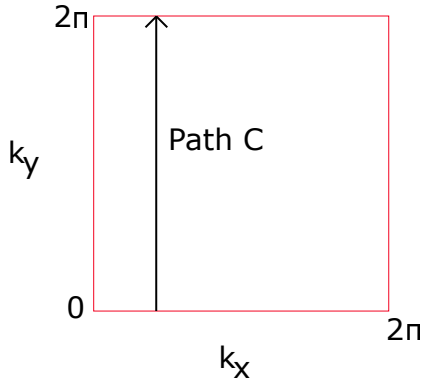

Figure 21: Example of close path in the Brillouin Zone that represents the variation of k_y from 0 to 2π with k_x constant.

The following equation gives the new state after a close loop along the n^{th} band [37]:

$$|\psi_n(\mathbf{k}_f, t_f = T)\rangle = e^{i\gamma_n} e^{-\frac{i}{\hbar}\int_0^T \varepsilon_n(\mathbf{k}(t))dt}\,|\psi_n(\mathbf{k}_i, t_i = 0)\rangle \tag{56}$$

with γ_n, the already presented Berry's phase of the n^{th} energy band presented in equation 52 and which is noted:

$$\boldsymbol{\gamma_n = \oint_C \mathbf{A_n[k]} \cdot \boldsymbol{d}\mathbf{k} = \oint_S \boldsymbol{\Omega_n[k]} \cdot \boldsymbol{d}\mathbf{S}} \tag{57}$$

When the crystal respects the time reversal symmetry ($t \to t'$) and the inversion symmetry, the Berry's curvature is limited by the following properties that lead to a zero Berry's curvature in the whole BZ:

$$\Omega_n(\mathbf{k}) = -\Omega_n(-\mathbf{k}) \text{ and } \Omega_n(\mathbf{k}) = \Omega_n(-\mathbf{k}) \tag{58}$$

Ungapped graphene respects these symmetries leading to a zero curvature. However, one interesting point about graphene is that its Berry's phase is equal to π. As explained in the theoretical part about pristine graphene, the eigenvectors obtained by solving the massless Dirac equation around K and K' are described by spinors:

$$\Psi = \begin{pmatrix} \Psi_A \\ \Psi_B \end{pmatrix} = \frac{1}{\sqrt{2}} \begin{pmatrix} \pm e^{\mp i\phi} \\ 1 \end{pmatrix} \tag{59}$$

It results that the Berry's connection is $\frac{1}{2}\frac{1}{q}$. For a closed path in the momentum space, the Berry phase is obtained by [33]:

$$\gamma = \oint_C \mathbf{A(q)} \cdot d\mathbf{q} = \int_0^{2\pi} \frac{1}{2}\frac{1}{q} d\phi = \pi \tag{60}$$

Experimentally speaking, this Berry's phase can be characterised by the suppression of the backscattering.

From equation 61, the Chern number associated to the n^{th} band becomes [27, 26, 24, 34, 35]:

$$C_n = \frac{1}{2\pi} \oint \Omega_n(\mathbf{k}) \cdot d\mathbf{S} \tag{61}$$

It remains invariant under small deformations of the Hamiltonian. This number will be used to topologically characterise the n^{th} band [38].

2.2 Charge Carriers in an electric field: Anomalous velocity

Charge carriers are represented by a superposition of waves that have individual phase velocity. The motion of the wave packet is characterized by the group velocity. When an electron is inside an electric field, the group velocity is firstly described by the following equation:

$$\mathbf{v}_n(\mathbf{k}) = \frac{\delta \varepsilon_n(\mathbf{k})}{\hbar \delta \mathbf{k}} \tag{62}$$

However, this description is uncomplete. Electrons can acquire an anomalous velocity, which comes directly from the Berry's Curvature. Indeed, Karplus and Luttinger proposed in 1954 an extra term called *anomalous velocity* [39]. This term was later linked with the Berry's curvature for an electron in an electric field as represented in the following equation [40]:

$$\boldsymbol{\mathbf{v_n}(\mathbf{k}) = \frac{\delta \varepsilon_n(\mathbf{k})}{\hbar \delta \mathbf{k}} - \frac{e}{\hbar} \mathbf{E} \times \Omega_n(\mathbf{k})} \tag{63}$$

with $\Omega_n(\mathbf{k})$ the already described Berry curvature of the n^{th} band. The anomalous velocity is always perpendicular to the electric field applied. This equation shows that in addition to the band energy, a description of the Berry's curvature of the band is also required. However, despite equation 62 is not complete, it accurately describes electrons subjected to an electric field in the case of crystal that respects both time-reversal and inversion symmetry, leading to a zero Berry's curvature over the whole BZ, as represented in equation 58. However, many systems can break one or both of these symmetries as ferromagnets or when a high magnetic field is applied leading to the quantum hall effect in $2D$ material, as will be explained in the next point.

2.3 Integer Quantum Hall effect: A topological description

In section 1.5.2, the integer quantum Hall effect obtained by solving the Schrodinger equation has been described. However, the bulk of the system can also be used to topologically describe this effect. The total current density is given by the contribution $e\mathbf{v}_n(\mathbf{k})$ (given in equation 63)of all the occupied states by omitting the first term of the group velocity(eq. 63):

$$\boldsymbol{J^n = \frac{e^2}{\hbar} \int (\Omega_n(k) \times E) f(\varepsilon_n) d\mathbf{k}} \tag{64}$$

with $f(\varepsilon_n)$, the occupation probability. At zero temperature, this probability is 0 or 1. As the electric conductance tensor, σ^n , comes from $\mathbf{J^n = \sigma^n E}$, the Hall conductivity for the n^{th} band, is given by [37]:

$$\sigma^n_{xy} = \frac{e^2}{h} \int \frac{d^2\mathbf{k}}{2\pi} \Omega_n(\mathbf{k}) = \frac{e^2}{\hbar} C_n \tag{65}$$

The integral corresponds to the Chern number described in equation 61 for the n^{th} filled band.

By considering all the filled bands under a high magnetic field for non-interacting electrons, the Hall conductivity is given by:

$$\sigma_{xy} = \sum_n \sigma^n_{xy} = \frac{e^2}{h} \sum_n C_n = \frac{e^2}{h} C \tag{66}$$

The band structure of electrons in a high magnetic field is split into LLs. By breaking the time-reversal symmetry, the Berry curvature is not zero, leading to a non-zero Chern number. Each LLs can be associated with a band structure carrying a Chern number of 1 [26]. The Chern number is only well defined in the case of an isolated band as for LLs where all levels are well separated from each other by a gap. Consequently, the total topological Invariant C that describes a material under a high magnetic field is just the sum of Chern numbers of each filled LLs, leading to a non-trivial insulator when the Fermi level is exactly in a band gap. As said before, the vacuum is a trivial insulator with a Chern number equal to zero. Consequently, at the spatial interface between the $2D$ material and the vacuum, the gap has to close, leading to the presence of edge states. By the bulk-edge correspondence principle, the number of edge states corresponds to the total Chern number C [41].

2.4 Haldane Model

By analyzing equation 66, Haldane realized that the only requirement to obtain edge states is to break the time-reversal symmetry leading to a non-zero Chern Number. In 1988, he proposed a theoretical model with graphene [2]. The spinless tight-binding model is given by the following equation:

$$H = t \sum_{<ij>} c_i^+ c_j + m \sum_i c_i^+ \sigma_z c_i + t' \sum_{<<ij>>} e^{i\phi_{ij}} c_i^+ c_j \tag{67}$$

The first term of this expression is the classical nearest-neighbour hopping of graphene. By adding the second term, Haldane breaks the inversion symmetry of graphene, implying that A and B sublattices are not equivalent anymore. In this term, σ_z represents the Pauli matrice for the pseudo-spin. However, only breaking the inversion symmetry is not enough to obtain a non-zero Chern number. As the time-reversal symmetry is still respected, the Berry's curvature at K and K' is not zero but has the same value with the opposite sign (equation 58). This is represented schematically in figure 22. The third term will break the time-reversal symmetry and will be described more precisely later in this section.

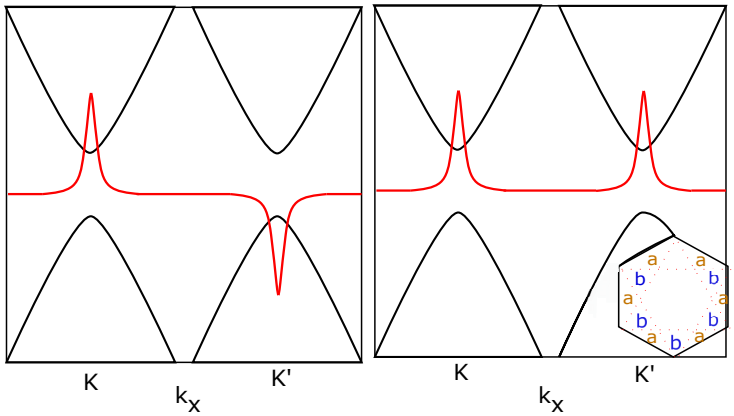

Figure 22: Representation of the Berry curvature at K and K' points of the Brillouin in the case of (a) breaking inversion symmetry and (b) breaking the time-reversal symmetry in graphene.

By calculating the eigenvalues of the massive low energy Dirac Hamiltonian of equation 67, the following expression is obtained [42]:

$$E = \pm\sqrt{\hbar^2 v_f^2 k^2 + m^2} \tag{68}$$

with '$\pm$' for the conduction and valence band respectively. Adding the massive term that breaks the inversion symmetry yields to a band gap of $2m$. The most famous example of this situation is the case of h-BN, which is a trivial insulator with a band gap of 6eV [43] and an hexagonal lattice. Boron and Nitrogen atoms respectively occupied the A and B sublattices leading to a difference of potential between the two sublattices. Consequently, a band gap is opened due to the inversion symmetry breaking.

The eigenvalues of the Hamiltonian of equation 67 have been computed using a tight binding model for different sets of parameters t, t' and m. The obtained band structure are presented in figure 23 for $t = -2.8eV$, $t' = 0eV$ and $m = 1eV$, leading to an absence of time-reversal symmetry breaking and a band gap of $2eV$.

The third term is the complex next-nearest neighbour hopping parameter. Haldane introduced this term in his model to break the time-reversal symmetry. By adding this new

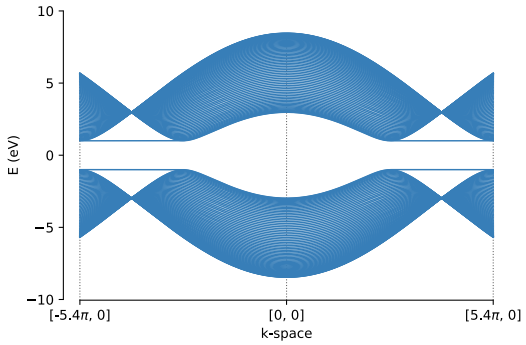

Figure 23: Band structure obtained by using Pybinding [44] for a zig-zag graphene nanoribbon with inversion symmetry breaking. The hopping parameter is$t = -2.8eV$, the m parameter is equal to 1 leading to a band gap of $2eV$. The width of the nanoribbon is $W = 15nm$. The lattice parameter is $0.24596nm$ with a carbon-carbon distance of 0.142 nm. The path in the BZ corresponds to $K \rightarrow \Gamma \rightarrow K'$ with k_y=0.

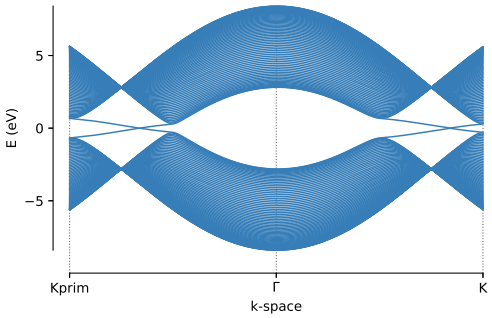

Figure 24: Band structure obtained by using Pybinding [44] for a zig-zag graphene nanoribbon with inversion symmetry breaking. The hopping parameter is $t = -2.7eV$, $m = 0.2eV$, $t' = 0.1t$ and $\phi = \frac{\pi}{2}$. The width of the nanoribbon is $W = 15nm$. The lattice parameter is $0.24596nm$ with a carbon-carbon distance of $0.142nm$. The path in the BZ corresponds to $K \rightarrow \Gamma \rightarrow K'$ with k_y=0.

term, Haldane proposes a model where the opposite magnetic field is applied in a and b regions (see right part of figure 22) with a zero net magnetic flux. This means that the nearest-neighbour hopping term is not affected[25]. As represented on the right part of figure 22, the integral of the Berry's curvature over the whole Brillouin zone is not zero anymore leading to a non-trivial Chern number. In the case of the Haldane model, the Chern number can be equal to ± 2 (due K and K' valley) depending on the value of the ratio $\frac{m}{t'}$ and the value of the phase ϕ.

Figure 24 represents the band structure when time-reversal symmetry is broken, obtained for $t = -2.8eV$, $t' = 0.1teV$, $m = 0.2eV$ and $\phi_{ij} = \frac{\pi}{2}$. As we can observe, there is a band gap in the bulk. However, at the edges, 2 states, one per valley, are present due to the non-trivial topology of the filled bands.

By using Kwant, a python-package, the presence of edge states can be confirmed by plotting the density of state which is given in figure 25(b). Figure 25(a) shows the conductance as a function of the energy. Due to the presence of edge states, when the Fermi level is located in the band gap, a non-zero conductance is observed, which corresponds to:

$$\sigma_{xy} = C\frac{e^2}{h} = 2\frac{e^2}{h} \tag{69}$$

with C the Chern number.
The Haldane model was difficult to obtain experimentally due to the difficult to apply a periodic potential. However, it was observed with ultracold fermions as presented in Ref. [45].

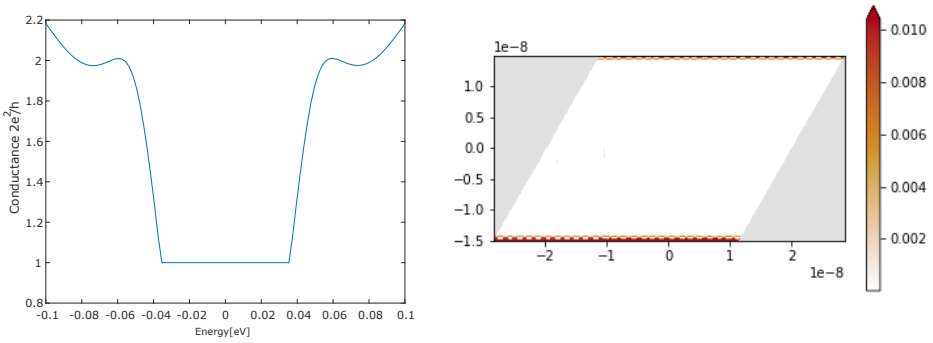

(a) (b)

Figure 25: (a) Conductance in function of the energy and (b) the density of state at the energy equal to $0.1teV$. The size of the system is $W = 30nm$ and $L = 22nm$ with a lattice parameter of $0.2459nm$ and a hopping term of $2.7eV$. The next-nearest hopping parameter,t', is equal to 0.6 eV and $m = 0.2$ eV with $\phi = \frac{\pi}{2}$.

2.5 Quantum spin Hall effect in graphene

In 2005, one year after the discovery of graphene by Andre Geim and Kostya Novoselov [46], a new phenomenon was theoretically described in graphene by Kane and Mele: the quantum spin Hall effect [3]. Figure 26 represents the principle of the quantum spin Hall effect compared to the quantum anomalous hall effect.

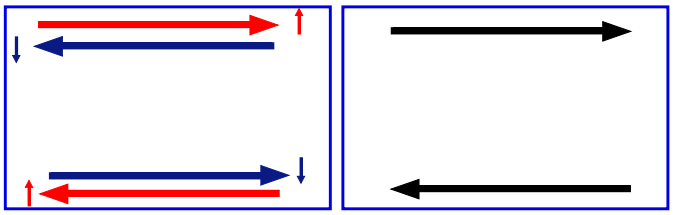

(a) (b)

Figure 26: Representation of (a) the quantum spin Hall effect and (b) the anomalous quantum Hall effect. In (a), on the top edge, the edge states correspond to the spin-up and spin-down move respectively forward and downward. On the bottom edge, it is the reverse situation.

As for the quantum anomalous Hall effect described by Haldane, quantum spin Hall effect is obtained with a zero magnetic flux. At each edge, one state per spin propagates in opposite directions. This surprising effect which shows a net transport of spin on both edges can be theoretically explained by introducing spin-orbit coupling in the Hamiltonian of the system.

The tight-binding Hamiltonian is:

$$\boldsymbol{H = -t \sum_{<ij>\alpha} c^{+}_{i\alpha} c_{j\alpha} + t_{in} \sum_{<<ij>>\alpha\beta} c^{+}_{i\alpha} i\sigma \cdot (d_{kj} \times d_{ik}) c_{j\beta}} \tag{70}$$

The second term describes a second neighbour tight-binding model. σ is the Pauli matrice for the real spin of the electron. However, the intrinsic spin-orbit coupling in graphene is too weak to observe this effect experimentally.

If the intrinsic spin-orbit interaction is taken into account, a band gap can be opened in

the bulk, which is topologically non-trivial, and spin filtered edge states that cross inside the band gap can lead to a quantum spin Hall effect as shown in figure 27. Indeed, charge carriers in graphene will experience a magnetic field due to their motion in the atomic electric field which will interact with their spins.

Figure 27 represents the band structure of the zig-zag nanoribbon of graphene for t_{in}=0.2t. This is not the real value calculated in graphene, which is very low (Ref. predicted a value of $12\mu eV$ [47] and Ref. [48] found experimentally a value of $20\mu eV$ for graphene on SiO_2) and which complicate the visualisation of edge states in the band structure.

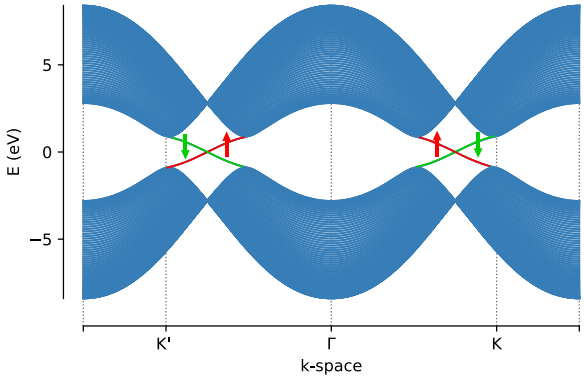

Figure 27: Band structure obtained by using Pybinding[44] for a zig-zag graphene nanoribbon by taking into account the intrinsic spin-orbit coupling. The hopping parameter is $t = -2.8eV$, t_{in} parameter is equal to $1eV$ leading to a bandgap of 2 eV. The width of the nanoribbon is $W = 15nm$. The lattice parameter is $0.24596nm$ with a carbon-carbon distance of 0.142 nm. The path in the Brillouin zone corresponds to $K \rightarrow \Gamma \rightarrow K'$ with k_y=0.

The robustness of the quantum spin hall effect is due to the conservation of the time-reversal symmetry since the conductance linked to one spin is opposite to the one of the other. A perfect transition is possible as for the previous Hall effect. Indeed, the charge carriers backscattering would require to flip their spin along the same edge or to occupy a state of the other edge.

2.6 Quantum Anomalous Hall Effect in Graphene induced by proximity effect with magnetic material

In the previous section, two different models implying topological effects in graphene have been presented: the Haldane model and the quantum spin Hall effect. Unfortunately, QSHE can not be experimentally observed in graphene due to a very weak intrinsic spin-orbit coupling. Indeed, Ref. [47] predicted a value of $12\mu eV$. In Ref. [48], a band gap of $42.2\mu eV$ was obtained for graphene on SiO_2. In addition, the Haldane model is also difficult to realize in graphene and has not been observed in graphene for the moment.

However, these models allow to understand how the topology of the material can induce edge states. In this section, the quantum anomalous Hall state in graphene induced by the proximity effect with magnetic material will be explained. In 2010, Qiao et al [49] investigated the possibility to obtain a non-zero Chern Number, implying edge states, without applying any external magnetic field. Indeed, they numerically obtained, by ab-initio calculations, that the Rashba spin-orbit coupling (RSOC) and the internal magnetisation induced by Fe adatoms can lead to a topological non-trivial band gap of $5.5meV$ in the bulk. A Chern number of 2 was found, meaning as explained in the section 2, a Hall conductivity of $2\frac{e^2}{h}$ when the Fermi Level lies in the band gap of the bulk graphene. Other publication numerically showed by ab-initio calculations the presence of a topologically

non-trivial band gap in the bulk like Ref. [4] by adding a film of graphene with $RbMnCl_3$, Ref. [50] with $MnPSe_3$.

2.6.1 Origin of the Rashba Spin-Orbit coupling and exchange field induced in graphene

2.6.1.1 Rashba Spin-Orbit Coupling

The Rashba Spin-Orbit coupling is a relativistic effect. When an electron with a momentum $\boldsymbol{p}$ moves in an electric field, it experiences an effective magnetic field in its rest-frame, which will interact with the real spin of the electron. Due to this effective magnetic field that is only felt by electrons, the spin-degeneracy is lifted by conserving the time-reversal symmetry. The Rashba spin-orbit effect is originated from breaking the inversion symmetry of material meaning that the sublattice A and B are not equivalent anymore. This can be achieved for example, by applying an external electric field or in a asymmetric quantum well as AlGaN/GaN/AlGaN [51], InAs/AlSb [52], InAlAs/InGaAs/InAlAs [53] resulting in an 'intrinsic' electric field.

The RSOC is also obtained at the surface between two materials by breaking the inversion symmetry at the interface [54]. Consequently, the requirement to generate a Rashba spin-orbit coupling is to break the inversion symmetry leading to an electric field resulting in a spin-orbit coupling of the charge carriers.

Compared to the very weak intrinsic spin-orbit coupling in graphene, the Rashba spin-orbit coupling can be greatly enhanced. This was already achieved numerically by depositing graphene on Ni(111) [55], by adding In, Sn, Sb, Te, I, La, Hf, Pt, Au, Hg, Tl, Pb and Bi on top of the surface [56] and was experimentally reported for Au in Ref. [57].

The tight-binding Hamiltonian of the RSOC in graphene in the real space is given by [58, 50, 59, 60]:

$$H_R = iV_R \sum_{<i,j>} c_i^+ \boldsymbol{e}_z \cdot (\boldsymbol{\sigma} \times \boldsymbol{d}_{ij}) c_j \tag{71}$$

with V_R, the strength of the RSOC, $\boldsymbol{\sigma}$, the Pauli matrices for the real spin and $\boldsymbol{d}_{ij}$, the unit vector pointing from the site j to site i. To obtain the band structure of graphene easily, one can express the Hamiltonian in the momentum space. By realizing the Fourier transformation developed in Ref. [58], the Hamiltonian is given by:

$$H_R(\boldsymbol{k}) = t_R \begin{bmatrix} 0 & f_R(\boldsymbol{k}) \\ f_R^*(\boldsymbol{k}) & 0 \end{bmatrix} \tag{72}$$

The 2×2 matrix is due to the presence of the A and B sublattices with $f_R(\boldsymbol{k})$ given by:

$$f_R(\boldsymbol{k}) = [(\cos\frac{\sqrt{3}k_x}{2}\sin\frac{k_y}{2} + \sin k_y)]s_x - \sqrt{3}\sin\frac{\sqrt{3}k_x}{2}(i\sin\frac{k_y}{2} + \cos\frac{k_y}{2})s_y \tag{73}$$

t_R is called the strength of the Rashba effect and is material dependent and $\boldsymbol{s}$ are the Pauli matrices for the real spin. This effect will lead to split the spin-degenerated energy level. This is mathematically visible in equation 72 by the presence of the Pauli matrices for the real spin. This effect was found to be very interesting to control the spin in graphene and, in the case of magnetic adatoms, makes graphene useable in spintronics. In this master thesis, we will explore the role that the magnetite nanoparticles have in breaking the inversion symmetry of graphene leading to a Rashba Spin-orbit coupling. As magnetite is magnetic, another phenomenon, the exchange field, has to be considered.

2.6.1.2 Exchange field

In addition to the RSOC, if the material used is magnetic, ferromagnetic order can be induced in graphene by proximity effect, due to the hybridization between the carbon π

states and the states of magnetic atoms. This leads to a natural time-reversal symmetry breaking and produces a macroscopic exchange field (the principle will be explained in the section 3 about magnetite.). By turning off the RSOC, the exchange field will lead to the lifting of the spin degeneracy. The spin-up bands are pushed upward and spin-down bands are pushed downward.

The tight-binding Hamiltonian of the exchange field induced in graphene in the real space is given by [49, 61, 59]:

$$H_{ex} = \lambda \sum_i c_i^+ s_z c_i \tag{74}$$

with λ, the strength of the exchange field and s_z, the Pauli matrice in z-direction for the real spin. By realizing the Fourier transformation developed in Ref. [58], the Hamiltonian in the momentum space of the exchange field in graphene is given by:

$$H_{ex} = \lambda \begin{bmatrix} s_z & 0 \\ 0 & s_z \end{bmatrix} \tag{75}$$

The spin-up and spin-down see respectively their energies change by a value of λ and $-\lambda$. This effect on graphene was already described in many papers. In Ref. [61], graphene/$BiFeO_3$ heterostructure was described. In addition to the already explained RSOC, an exchange field in graphene was observed due to the hybridization between Fe $3d$ state and $2p_z$ state of graphene. A value of $142meV$ for the exchange strength was obtained by ab-initio calculation. This effect was experimentally confirmed for this heterostructure in Ref. [62]. In Ref. [4] the graphene/$RbMnCl_3$ heterostructure was considered. Due to the hybridization of the Mn $3d$ state with the $2p_z$ state of graphene, an exchange strength of $280meV$ was obtained by ab-initio calculation.

2.6.2 General tight-binding Hamiltonian of graphene

The global tight-binding Hamiltonian in the real space for graphene is given by:

$$H_o + H_R + H_{ex} = -t \sum_{<ij>} c_i^+ c_j + iV_R \sum_{<i,j>} c_i^+ \boldsymbol{e}_z \cdot (\boldsymbol{\sigma} \times \boldsymbol{d}_{ij}) c_j + \lambda \sum_i c_i^+ s_z c_i \tag{76}$$

The combination of the two effects, leading to the inversion symmetry breaking and the time-reversal symmetry breaking, open a gap in the bulk graphene at points K and K'. The low-energy Hamiltonian in k-space is given by:

$$H = -\hbar v_f (\eta q_x \sigma_x + q_y \sigma_y) \mathbf{1}_s + \lambda \mathbf{1}_s s_z + \frac{V_R}{2} (\eta \sigma_x s_y - \sigma_y s_x) \tag{77}$$

with $\boldsymbol{\sigma}$ and $\boldsymbol{s}$, respectively the Pauli matrices of the pseudo and the real spin. The first term is the Dirac Hamiltonian described in section 1.2. By diagonalization of the low-energy Hamilatonian, the band gap induced by the presence of the Rashba spin-orbit coupling and the exchange field is equal to [63]:

$$\Delta = \frac{2V_R\lambda}{\sqrt{\lambda^2 + V_R^2}} \tag{78}$$

3 Magnetism in magnetite Fe_3O_4

In this section, the magnetic properties of magnetite (Fe_3O_4) will be discussed. Firstly, the crystal structure of the magnetite will be described. Secondly, the magnetism in the bulk magnetite will be developed. Finally, the differences in the magnetic properties due to the reduction of the particle size will be explained.

3.1 Crystal structure

The crystal structure of magnetite is represented in figure 28. It is part of the spinel family [64]. In general, spinel structure [64] is formulated by AB_2X_4, with A^{2+} and B^{3+} being cations that occupy tetrahedral and octahedral sites and X^{2-} being an anion. However, magnetite has an inverse spinel structure $B(AB)X_4$ that is formulated by $(Fe^{3+}[Fe^{3+}Fe^{2+}]O_4)$. The difference with the previous structure is that half of the B cations switch place. The AB ions between brackets occupy the octahedral sites and the B ions occupy tetrahedral sites as represented in figure 28 [65].

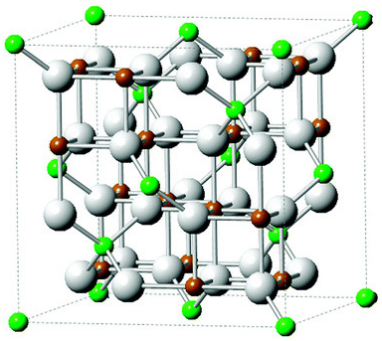

Figure 28: Structure of magnetite from Ref [65]. The oxygen, trivalent iron and divalent irons ions are respectively in grey, red and green.

The unit cell is a face-centered cubic structure with space group Fd_3m and its length is $a = 0.839nm$. Oxygen ions occupy the fcc closed packed sites [66]. This iron oxide is particular because it is composed of divalent and trivalent iron ions. These ions occupy the interstitial sites between the oxygen ions.

3.2 Ferrimagnetism in bulk magnetite

Magnetite is ferrimagnetic at a temperature lower than 850K [67], called the Curie temperature. The net magnetic moment is due to the Fe^{2+} ions present in the octahedral sublattice. Indeed, the magnetic moment of Fe^{3+} ions from the tetrahedral sublattice is compensated by the magnetic moment of Fe^{3+} ions from the octahedral sublattice [68].

The bulk magnetite is composed of different domains, called the Weiss domains, separated by Bloch walls as it can be seen in the left part of the figure 31. Each domain has its own uniform direction of spontaneous magnetization leading to a global non-magnetization at zero external magnetic field. There are six directions of easy magnetization corresponding to the three [111] axis [64]. The Bloch walls are used to separate the different domains. An example of Bloch walls, in red, are given in figure 29. Inside these walls, the magnetization direction changes between the two directions of the adjacent domains. The spontaneous magnetization is due to interactions between electrons from adjacent atoms which allows the alignment of the atomic moment in a certain direction [68]. In the case of magnetite, the exchange interaction leading to a ferrimagnetic behavior between the octahedral and tetrahedral sublattices is provided by the oxygen ions. This exchange is called superexchange interaction, which is different from the direct exchange.

The direct exchange is characterized by the Heisenberg Hamiltonian given by [69]:

$$H_{Hei} = -J \sum_{<i,j>} S_i \cdot S_J \tag{79}$$

with J, the exchange integral and $S_{i/j}$ the two spin angular momenta. The bracket "<>" means that only the coupling between electrons from the nearest neighbor atoms are considered. Indeed, to obtain a direct exchange interaction, it is crucial to have a direct hopping between the d-orbitals. Because they are localised, it is only happening between orbitals on different atoms that are very close, which is not the case in magnetite. However, to explain the ferrimagnetic behaviour of magnetite, the direct exchange is extended by taking into account the hopping with p-orbital of oxygen. Superexchange describes the interaction between two Fe-atoms that are too far to be connected by direct exchange but are connected through a non-magnetic entity [70].

The presence of different domains is the configuration that minimize magnetostatic energy. Indeed, if only one domain is considered, its magnetization will induce magnetic poles on its surface leading to an increase of the magnetostatic energy. The formation of different domains allows the reduction of this energy. However, forming different domains requires the presence of Bloch walls. Consequently, several terms have to be taken into account. These terms are given in the following equation which represents the total energy of the system [68].

$$E = E_{exch} + E_a + E_s + E_{ms} + E_h \tag{80}$$

E_{exch},the exchange energy, is due to the angular deviation of the magnetization direction in the Bloch Wall. To reduce this term, the walls have to be wide. E_a,the magnetocrystalline anisotropy, is due to the angular deviation from one easy-magnetization direction to another in the Bloch Walls. To reduce this term, the walls have to be the narrowest. E_s is the magnetoelastic energy due to a mechanical strain/deformation. E_{ms} is the the magnetostatic energy and causes the formation of domains. E_h is the magnetic energy due to the presence of an external magnetic field. The system at a given size, temperature and in a given external magnetic field which minimizes the total energy, will be the equilibrium system.

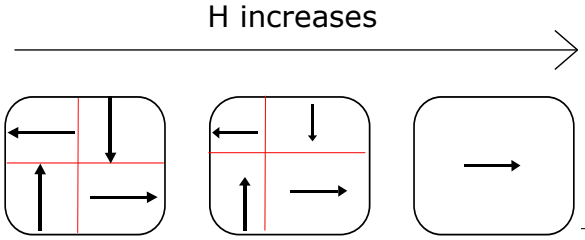

Figure 29: Representation of the evolution of domains by increasing the external magnetic field. The magnetization direction in every domains will start to rotate. If the external magnetic field is sufficiently high, the magnetization of all the domain will be in the direction of the external field.

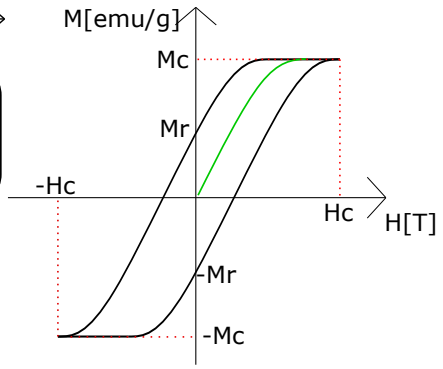

Figure 30: Representation of an hysteresis curve [71].

By applying a sufficiently large external magnetic field (H), the direction of magnetization in every domain is rotated from their easy axis of magnetization to an axis parallel to the external field[72]. This situation is represented in figure 29. Figure 30 represents the general M-H curve of a magnetic material. Before applying any external field, because of the different domains, the global magnetization is zero. Then, when the external field increases, the magnetization in the direction of the field increases as well, by following the green curve in figure 30, until it reaches a saturation value (M_c). This corresponds

to the case where all the domains have the same direction of magnetization. At room temperature, the value of the saturated magnetization is $92 emu/g$ [73]. The decrease in the field initially applied induces rotations towards the easy directions closest to those of H. However, it can be seen that the magnetization does not return to the curve of the first magnetization; in particular, for a zero field, the magnetization keeps a positive value called the remanent magnetization M_r. The field must be reversed to cancel M.

3.3 Size-dependent magnetic behaviour

In the previous part, the magnetism in bulk magnetite was described. When the dimension of the material decreases until it reaches the range of a few nanometers up to hundreds of nm, the magnetic properties in magnetite change and become strongly size-dependent. Two diameters are important to understand the changes in magnetic properties: the critical diameter, D_c and the threshold diameter, D_t. These diameters induce three different behaviors [74]:

- If $D_{NPs} > D_c$: In this case, the nanoparticles are composed of several, as explained in the previous point in the case of bulk magnetite. The coercivity field of the particle increases when the size of the particle is reduced, until it obtains its maximum value at D_c.
- If $D_t < D_{NPs} \leq D_c$: In this case, the nanoparticles are only composed of one domain. Indeed, the presence of Bloch Walls and multi-domains are not energetically favorable. Consequently, the magnetization is already saturated even without any external magnetic field. When the diameter becomes close to D_t, the magnetization of the nanoparticles becomes more and more unstable.
- if $0 < D_{NPs} < D_t$: In this case, the nanoparticles become superparamagnetic. Indeed, the magnetization is completely unstable and can be reversed to 180° due to thermal activation.

Figure 31 represents the evolution of the magnetization when the size of the nanoparticle reduces.

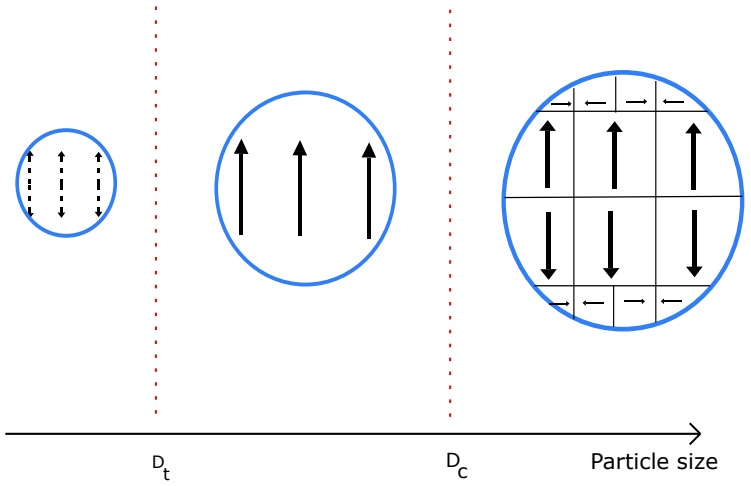

Figure 31: Domains in nanoparticles in function of their diameter.

These three behaviors are directly related to the minimization of the energy represented in equation 80. The value of the two diameters are material and temperature-dependant. In the case of magnetite, at room temperature, D_c is in the range of 80 to 100nm and D_t is in the range of 20 to 30 nm [75].

In general, as for bulk material with the Curie temperature, nanoparticles exhibit a superparamagnetic behavior above a specific temperature called the blocking temperature

which is smaller than the Curie temperature. However, contrary to bulk material that becomes paramagnetic due to the spins disorder, the superparamagnetic behavior is due to spins reversal. Indeed, above the blocking temperature, the energy barrier,K_{eff}V, which separates the easy directions of magnetization, with K_{eff} the effective anisotropy and V the volume of the nanoparticle, is lower than the thermal energy, k_BT. Consequently, the spins reverse many times, leading to a magnetization close to zero.

The time between two spin reversals is given by the Arrhenius formula [76]:

$$\tau = \tau_0 e^{\frac{K_{eff}V}{k_BT}} \tag{81}$$

with $\tau_0 = 10^{-9}$s, the expected time of spin reversal [72]. The value of the blocking temperature depends on the size of the nanoparticle, the experimental time scale and the effective anisotropy.

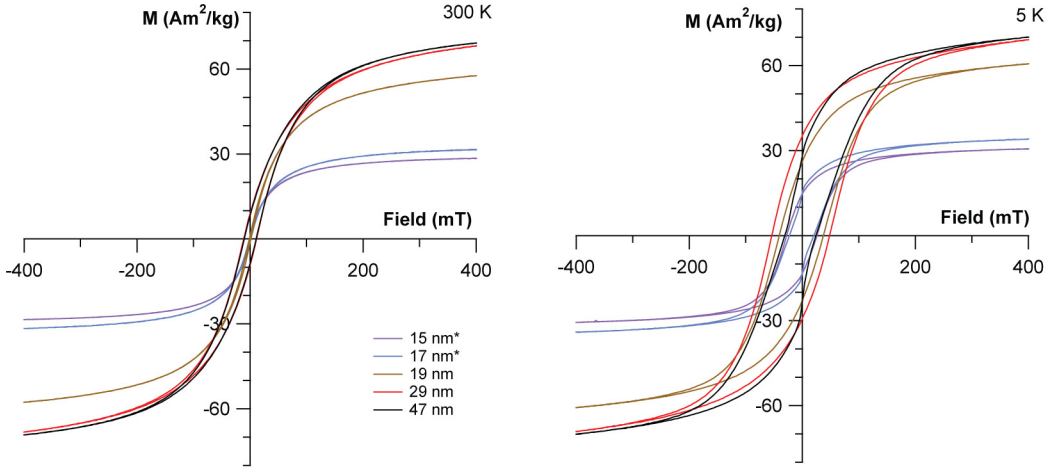

Figure 32: Magnetic properties at 300K and 5K. M-H curbe obtained by changing the size of the nanoparticles from Ref.[75]

Figure 32 represents the M-H curve for different sizes of nanoparticles at two different temperatures obtained by Baumgartner et al. [75]. When the temperature is lower than the blocking temperature, the M-H curve does not have any hysteresis. At zero external field, for nanoparticles in the superparamagnetic state, the magnetization is zero.

3.3.1 Saturated magnetization of ferrimagnet nanoparticles

To conclude this section, the effect of using nanoparticles in the saturated magnetisation will now be explained. Indeed, if we consider a system composed of nanoparticles and another bulk one with the same volume, the same saturated magnetization should be observed. However, it is experimentally not true [77, 78] . In the case of oxide nanoparticles, surface effect can lead to reduce the magnetization of the nanoparticle systems compared to the one in bulk material. As long as the size of the nanoparticles reduces, these surface effects become more and more important due to an increase of the ratio between surface and volume. Indeed, at the surface, the spins are not ordered as in the core [74]. The spin disorder is due to the modification of the exchange interaction between surface magnetic ions. Consequently, if the oxygen is not present or if there is another ion as

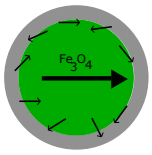

Figure 33: Representation of a magnetite nanoparticle composed of a core of Fe_3O_4 surrounded by a organic shell. The saturated magnetisation was reached and the arrow represent the direction of magnetisation.

impurity, this can lead to the breaking of the exchange interaction between the magnetic ions leading to spins disorder at the surface [79]. This is represented in figure 33.

This section concludes the theoretical part of this work. The primary objective of this master thesis is to explore the emergence of the quantum anomalous Hall effect induced by nanoparticles of magnetites deposited on graphene via simulations. Indeed, the presence of nanoparticles of magnetites should induce a RSOC and an exchange field in graphene and should therefore induce, as explained in section 2.6, the opening of a topologically non-trivial bandgap in bulk graphene. The first simulation technique will use Kwant, a python package for quantum transport calculations based on tight-binding model. The second simulation technique will use ab-initio computation. A Fe atom on top of the hollow position of a 4×4 supercell of graphene of graphene was considered to determine the value of the band gap in the bulk of graphene. The second objective is to explore what can be done experimentally to highlight the quantum anomalous Hall effect.

4 Simulation Results

4.1 Tight-binding simulation

In this section, the results obtained with Kwant and Pybinding will be presented and discussed. Firstly, the system composed of graphene with a uniform RSOC and exchange field will be considered. The band structure of bulk graphene will be given to highlight the presence of a band gap. Then, the density of states (DOS) and the conductance obtained by Kwant will be analyzed. The effect of the disorder on the system will then be considered. As the purpose of this master thesis is to cover graphene with magnetite nanoparticles, the effect of a non-uniform RSOC and exchange field on the conductance will be shown. The parameter, already presented in equation 76, will be fixed to the generic values: $V_R = 0.2eV$ and $m = 0.1eV$. These values are only used to qualitatively determine the effect of the RSOC and exchange field on graphene and do not represent the physical reality. During this simulation, we do not take into account the intrinsic spin-orbit coupling of graphene. However, due to its low value, we do not expect that it would affect our results.

4.1.1 Band Structure

Figure 34 represents the band structure of the bulk graphene obtained by using Pybinding when the RSOC and/or the exchange field are applied. Pybinding is a scientific Python package for numerical tight-binding calculations in solid state physics. The tight-binding model given in equation 76 was implemented for an infinite graphene sheet. Figure 34

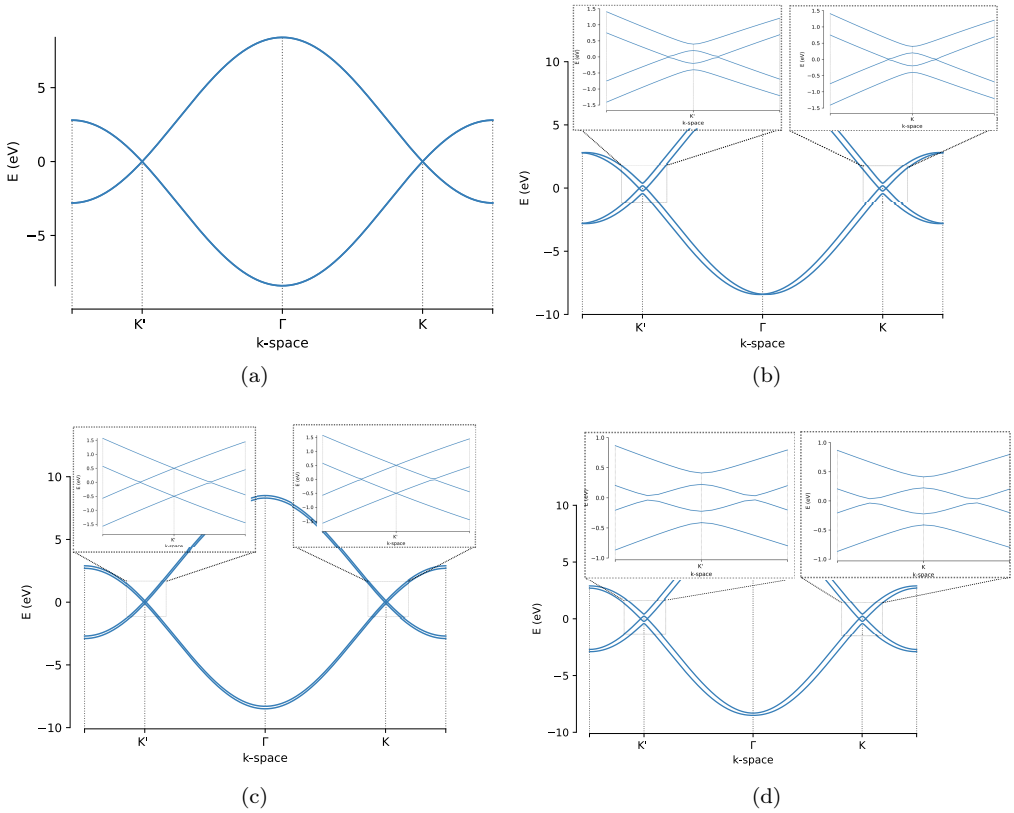

Figure 34: Band structure of bulk graphene obtained with Pybinding with the hopping parameter $t = -2.8eV$ and (a) $V_R = 0.0eV$ and $\lambda = 0.0eV$, (b) $V_R = 0.2eV$ and $\lambda = 0.0eV$,(c) $V_R = 0.0eV$ and $\lambda = 0.1eV$, (d) $V_R = 0.2eV$ and $\lambda = 0.1eV$. The path in the Brillouin zone is $K \rightarrow \Gamma \rightarrow K'$ with $k_y = 0$.

(a),(b),(c) represents the band structure in the case of pristine graphene, graphene with RSOC and graphene with exchange field.

As shown in figure 34(d), a band gap is opened when both RSOC and exchange field are present, which highlights an insulator state as confirmed in Refs. [49, 63, 59, 80]. The band gap is equal to $0.18eV$, which corresponds to the value obtained by using the equation 78.

4.1.2 Conductance and density of state

In this section, a system with a width and a length of $150nm$ was used with two vertical leads. Figure 35 represents the conductance as a function of the Fermi level. As can be seen, in the band gap of the bulk graphene, the conductance is equal to $2\frac{e^2}{h}$.

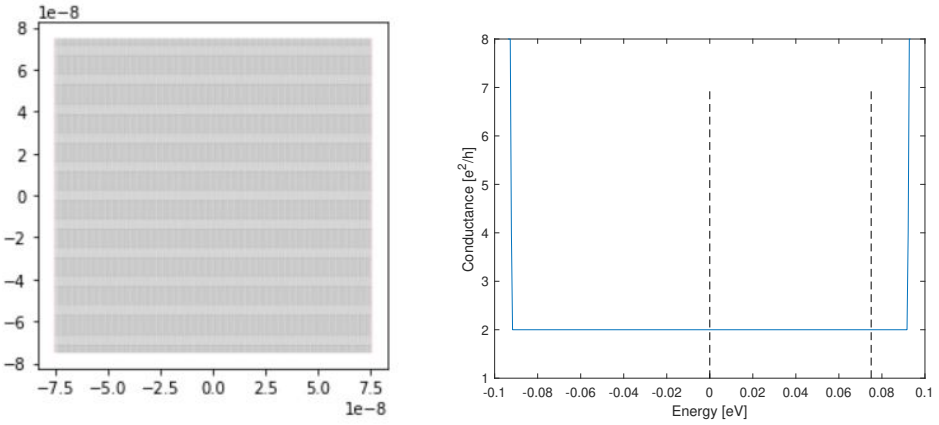

(a) (b)

Figure 35: (a)System used to obtain conductance. The leads are represented in red. The system has a width and a length of $150nm$. (b)Conductance as a function of the position of the Fermi Level. The hopping parameter is $t = -2.8eV$, the RSOC strenght is $0.2eV$ and the exchange field strength is $0.1eV$. The number of points used to obtain this curve is 300 for energies between -0.01 and $0.01eV$.

Indeed, the insulator state obtained by plotting the band structure in figure 34 is topologically non-trivial. Consequently, as expressed in the section 2, this leads to the presence of edge states. In this situation, there are two states per edge, one per valley. The states from different edges propagate in the opposite direction. Figure 36 highlights the presence of these edges states. Indeed, when the Fermi level is in the band gap, as in figure (a) to (d), the edge states can be observed which is not the case when the Fermi level is outside the band gap. In addition, the band gap obtained with Pybinding in figure 34(d) correspond to the interval of energy where the edge state are obtained with the Kwant simulation.

These edges states induced by the RSOC and exchange field without the application of any magnetic field were also highlighted in a general case in Ref [58], by considering Fe atoms adsorbed on top of graphene in Refs [49, 50] or by covering the graphene with a real antiferromagnetic insulator $RbMnCl_3$ in Ref. [4].

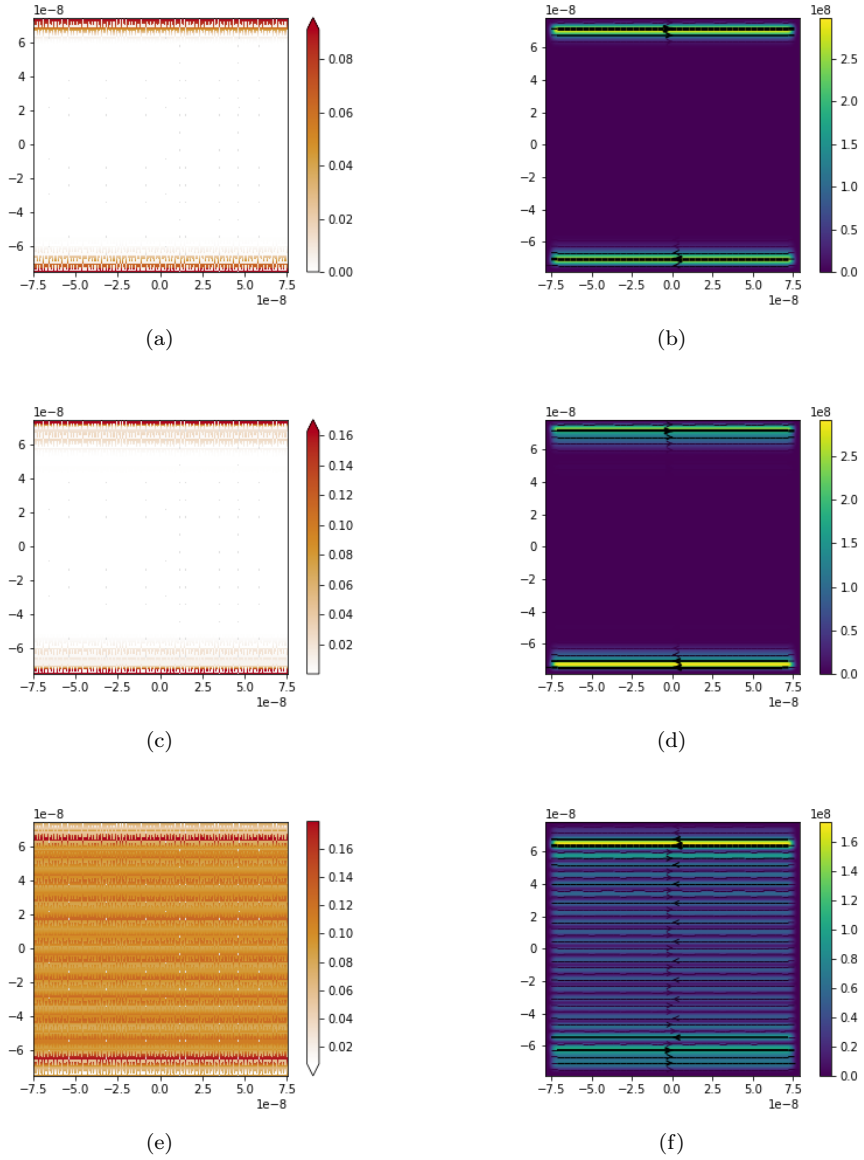

Figure 36: Density of states and current in arbitrary units for energy of $0.0eV$ for (a) and (d), $0.075eV$ for (b) and (e) and $0.12eV$ for (c) and (f). The system used is a nanoribbon of graphene with a width and a length of 150nm. The hopping parameter is $t = -2.8eV$, the RSOC strenght is $0.2eV$ and the exchange field strength is $0.1eV$.

4.1.3 Hall and longitudinal resistivity

To represent a more realistic situation, three more horizontal leads will be added as represented in figure 37(a). The upside right lead is grounded. With this configuration, it is now possible to calculate the Hall and longitudinal conductivity. The result is shown in figure 37(b). Again, as long as the Fermi Level is located in the band gap, the Hall conductivity will be equal to $\frac{1}{2}\frac{h}{e^2}$ and the longitudinal resistivity will be zero.

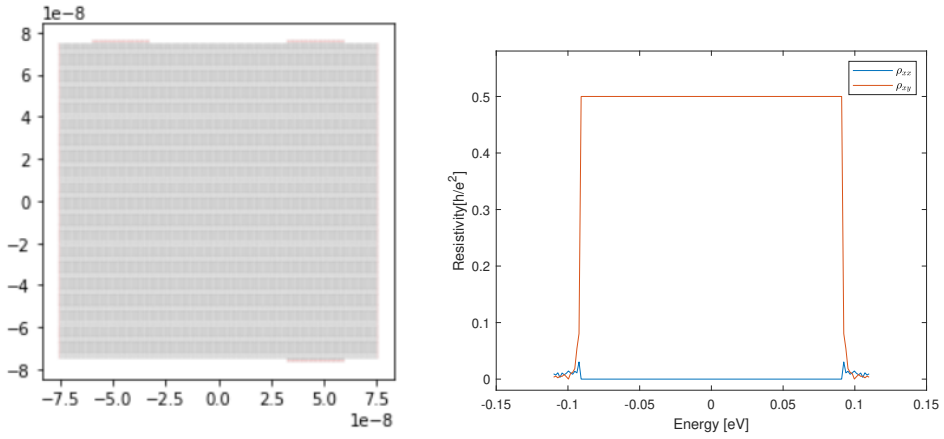

(a) (b)

Figure 37: (a) System used to obtain the Hall and longitudinal resistivity. The leads are represented in red. The system has a width and a length of $150nm$ and (b) Resistivity as a function of the position of the Fermi Level. In red, the Hall resistivity, ρ_{xy} and in blue, the longitudinal resistivity, ρ_{xx}.The hopping parameter is $t = -2.8eV$, the RSOC strenght is $0.2eV$ and the exchange field strength is $0.1eV$.

4.1.4 Effect of disorder

In this section, the effect of disorder on the quantum anomalous Hall effect is studied. A new term is added to the tight-binding model described in equation 76, due to the presence of disorder:

$$\sum_i E_i c_i^+ c_i \tag{82}$$

The disorder is included by varying the onsite energies E_i randomly in the interval $[-U_0, U_0]$. It is important to note that the disorder used in this section corresponds to local variations in potential related to non-magnetic impurities such as PMMA or charges in SiO_2. Figure 38 represents the conductance as a function of the Fermi level for different disorder strengths.

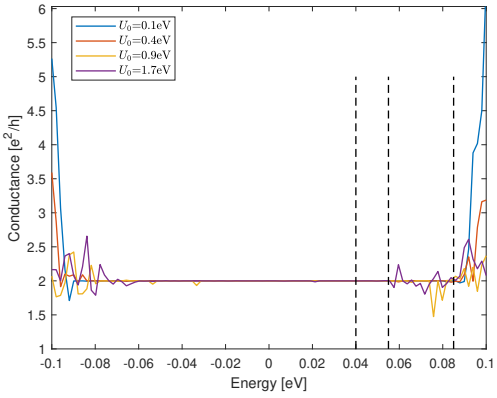

Figure 38: Conductance as a function of the Fermi level for four different disorder strengths. The hopping parameter is $t = -2.8eV$, the $RSOC$ strenght is $0.2eV$ and the exchange field strength is $0.1eV$.

The quantum anomalous Hall effect seems robust even with a disorder strength of $1.7eV$. However the range of energy where the edge states are observable reduce when the disorder strength increases. Few examples of the density of states and density of current are given

in figures 39, 40 and 41. When the conductivity is not $2e^2/h$, the quantum anomalous Hall effect is not present which is observable for example in figures 41 (e)/(f) and (g)/(h).

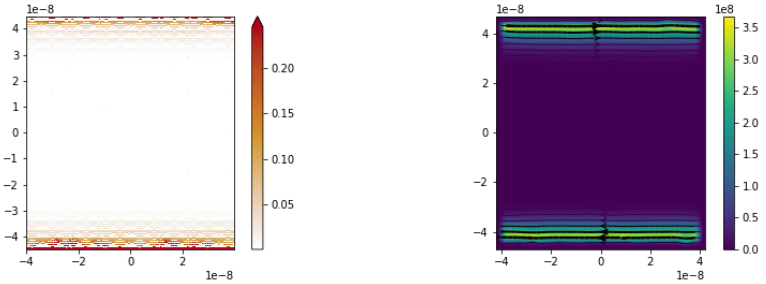

(a)

(b)

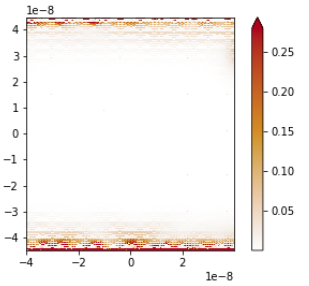

(c)

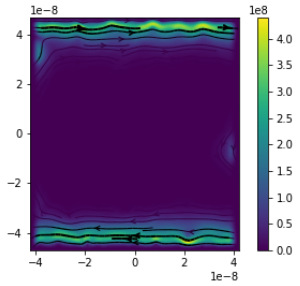

(d)

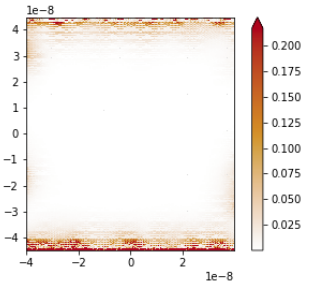

(e)

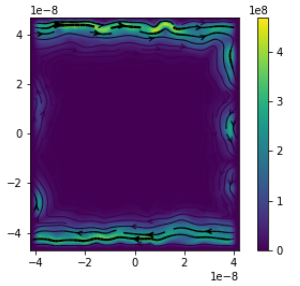

(f)

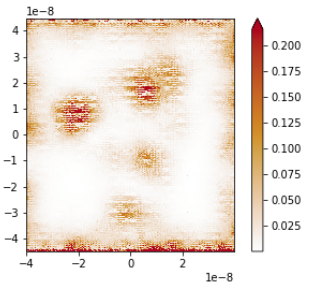

(g)

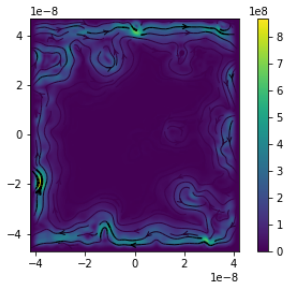

(h)

Figure 39: Density of states and current in arbitrary units for energy of $0.04eV$ with (a) and (b) $U_0 = 0.1eV$, (c) and (d) $U_0 = 0.4eV$, (e) and (f) $U_0 = 0.9eV$, (g) and (h) $U_0 = 1.7eV$. The system used is a nanoribbon of graphene with a width and a width of $90nm$ and a length of $80nm$. The hopping parameter is $t = -2.8eV$, the RSOC strength is $0.2eV$ and the exchange field strength is $0.1eV$.

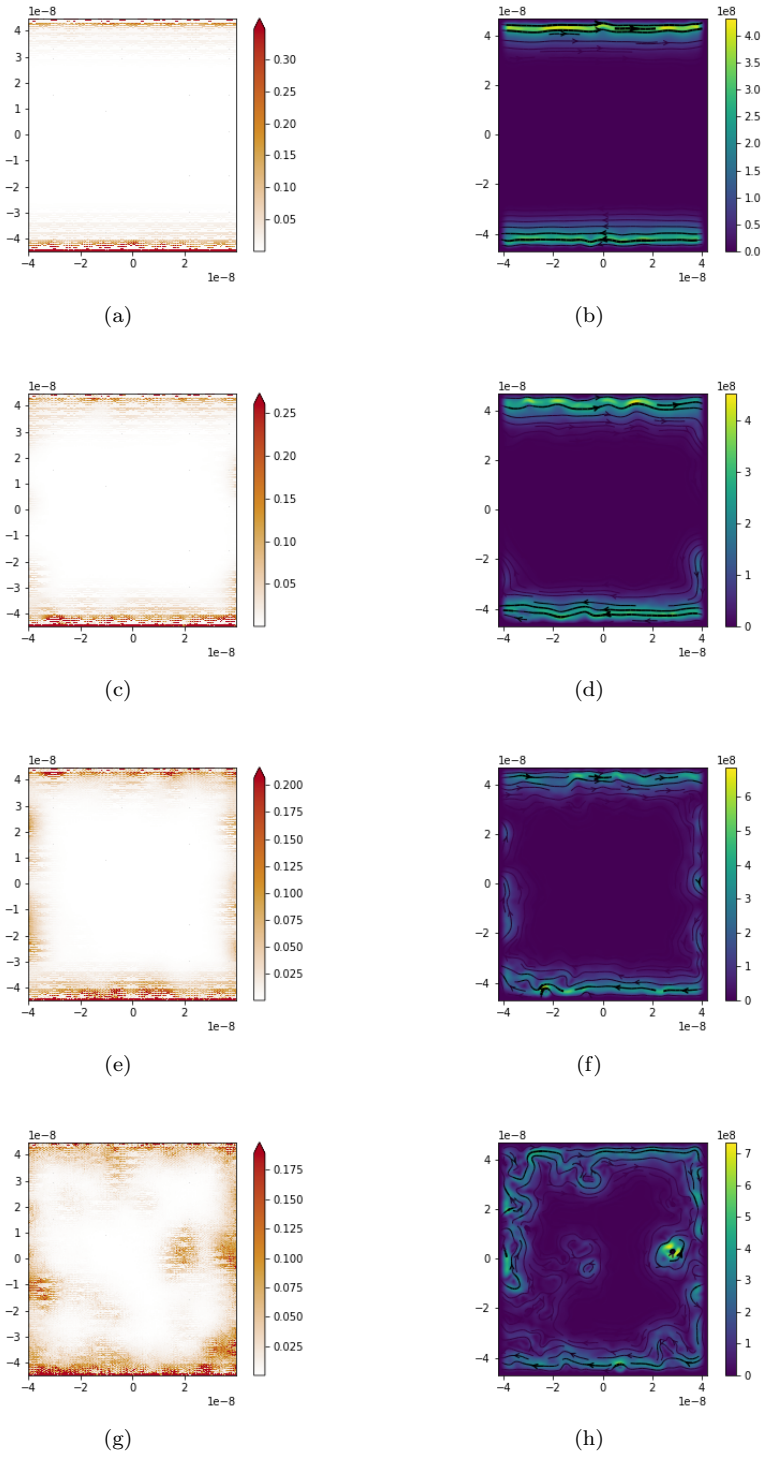

Figure 40: Density of states and current in arbitrary units for energy of $0.055eV$ with (a) and (b) $U_0 = 0.1eV$, (c) and (d) $U_0 = 0.4eV$, (e) and (f) $U_0 = 0.9eV$, (g) and (h) $U_0 = 1.7eV$. The system used is a nanoribbon of graphene with a width and a width of $90nm$ and a length of $80nm$. The hopping parameter is $t = -2.8eV$, the RSOC strenght is $0.2eV$ and the exchange field strength is $0.1eV$.

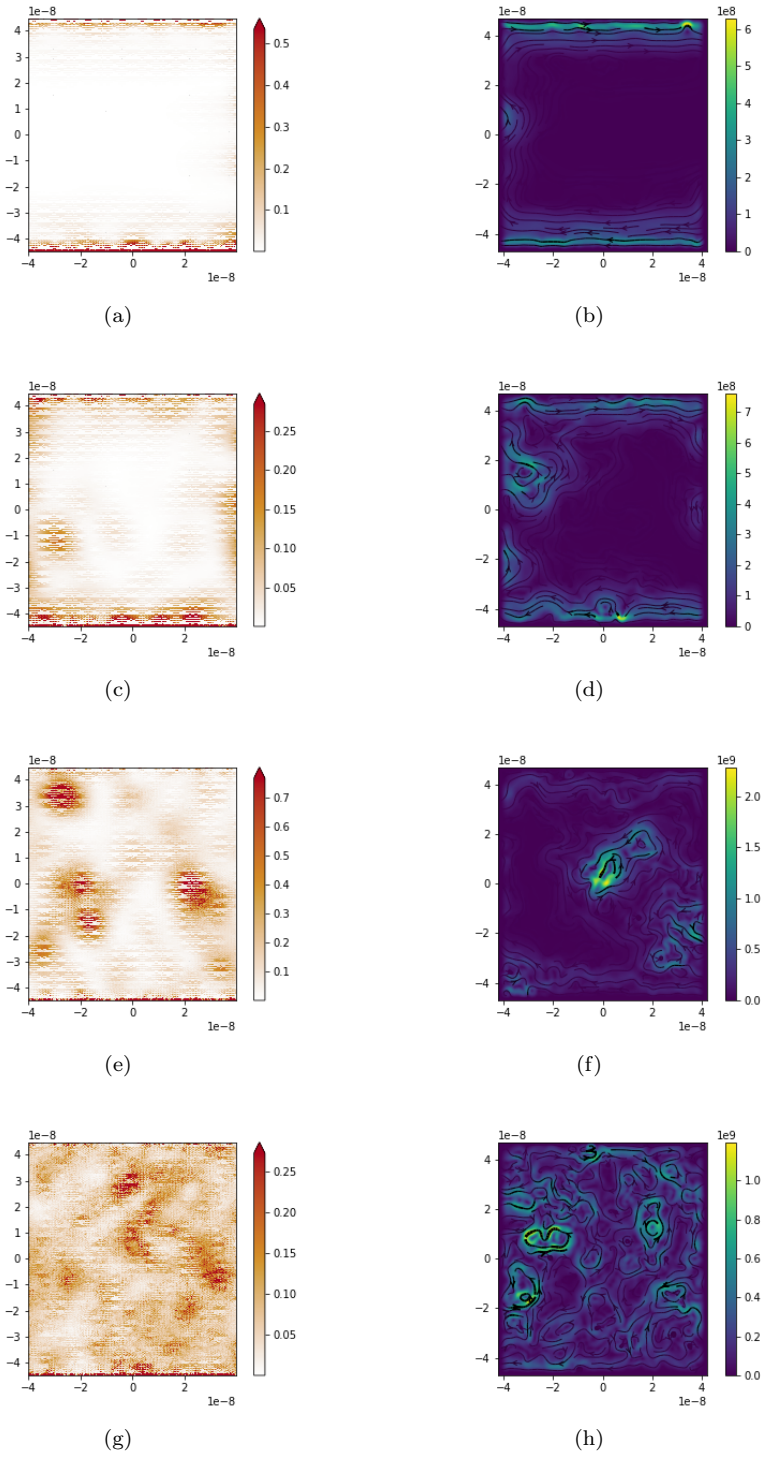

Figure 41: Density of states and current in arbitrary units for energy of $0.085eV$ with (a) and (b) $U_0 = 0.1eV$, (c) and (d) $U_0 = 0.4eV$, (e) and (f) $U_0 = 0.9eV$, (g) and (h) $U_0 = 1.7eV$. The system used is a nanoribbon of graphene with a width and a width of $90nm$ and a length of $80nm$. The hopping parameter is $t = -2.8eV$, the RSOC strenght is $0.2eV$ and the exchange field strength is $0.1eV$.

4.1.5 Effect of a non-uniform Rashba spin-orbit coupling and exchange field

A non-uniform RSOC and exchange field will now be applied at the surface of graphene. Due to the time required by the simulation, a smaller system than the one used in the previous section was used. An example of system used for the simulation is represented in figure 42(a). The dark part on this figure represents the region where the graphene felt the RSOC and the exchange field. Their sizes are $10nm$ and mimic the presence of nanoparticles at the surface which are geometrically homogeneously dispersed. In these regions, the tight-binding model given in equation 76 was implemented. In the rest, the tight-binding model presented in section 1.2 was implemented. Figure 42(b) represents the conductance as a function of the position of the Fermi level in system with different density of nanoparticles.

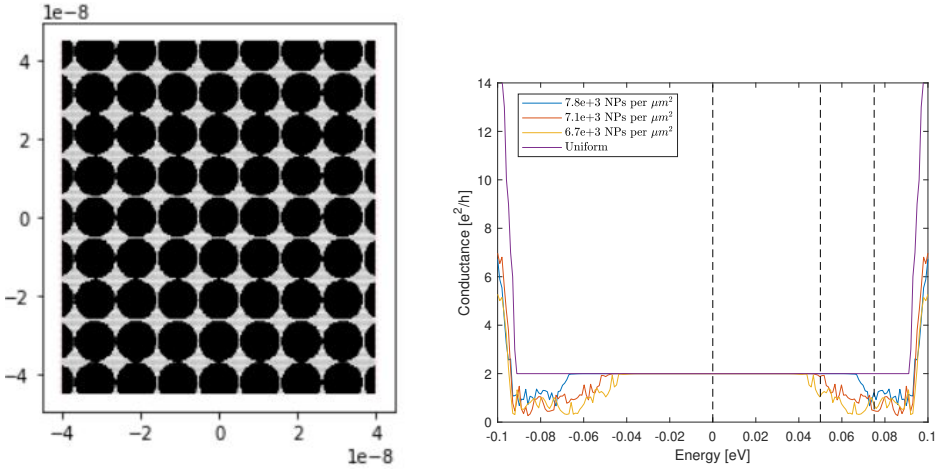

(a) (b)

Figure 42: (a)Example of system used for the simulation which corresponds to the density of nanoparticles of 7800 $NPs/\mu m$. It has a width of $90nm$ and a length of $80nm$. In dark, the region that feels the effect of the $RSOC$ and the exchange field.(b) Conductance as a function of the Fermi level for three different densities of $10nm$-diameter nanoparticles and the case of a uniform $RSOC$ and exchange field. The hopping parameter is $t = -2.8eV$, the $RSOC$ strenght is $0.2eV$ and the exchange field strength is $0.1eV$.

As can be seen, a conductance of $\frac{2e^2}{h}$ is still observable. However, the range of energy in which the edge states are obtained reduced with the density of the nanoparticles. Figure 43, 44 and 45 represent the density of states and the density of current at, respectively, the Fermi level equal to $0eV$, $0.05eV$ and $0.075eV$ for the different densities of nanoparticles used in figure 42. When the Fermi Level is in the region where the conductance is not equal to $2\frac{e^2}{h}$, the quantum anomalous Hall effect can not be obtained anymore as shown, for example, in figures 45(c) to (h).

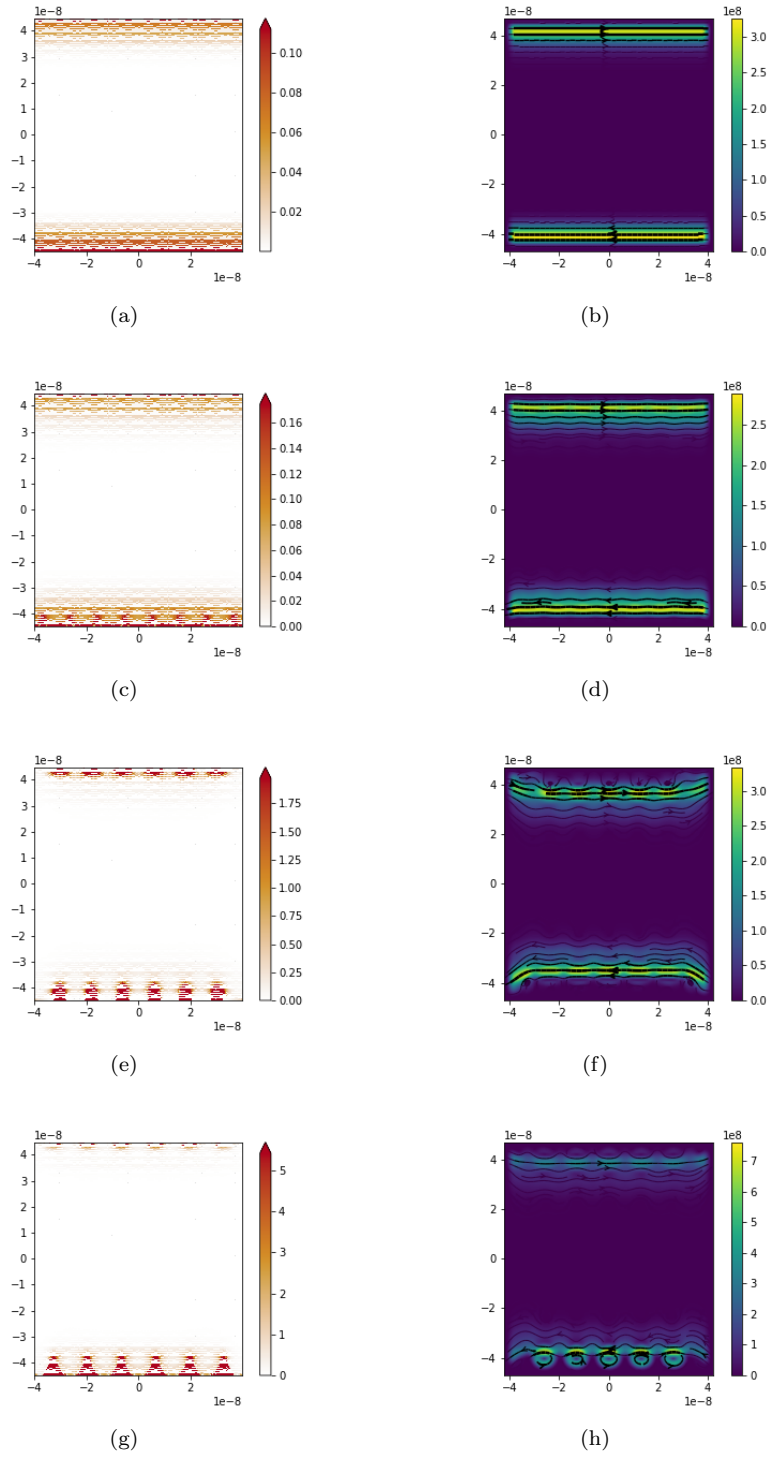

Figure 43: Density of states and current in arbitrary units for energy of $0.0eV$ with (a) and (b) Uniform $RSOC$ and exchange field, (c) and (d) $7800NPs/\mu m^2$, (e) and (f)$7100NPs/\mu m^2$, (g) and (h) $6700NPs/\mu m^2$. The system used is a nanoribbon of graphene with a width and a width of $90nm$ and a length of $80nm$. The hopping parameter is $t = -2.8eV$, the RSOC strength is $0.2eV$ and the exchange field strength is $0.1eV$.

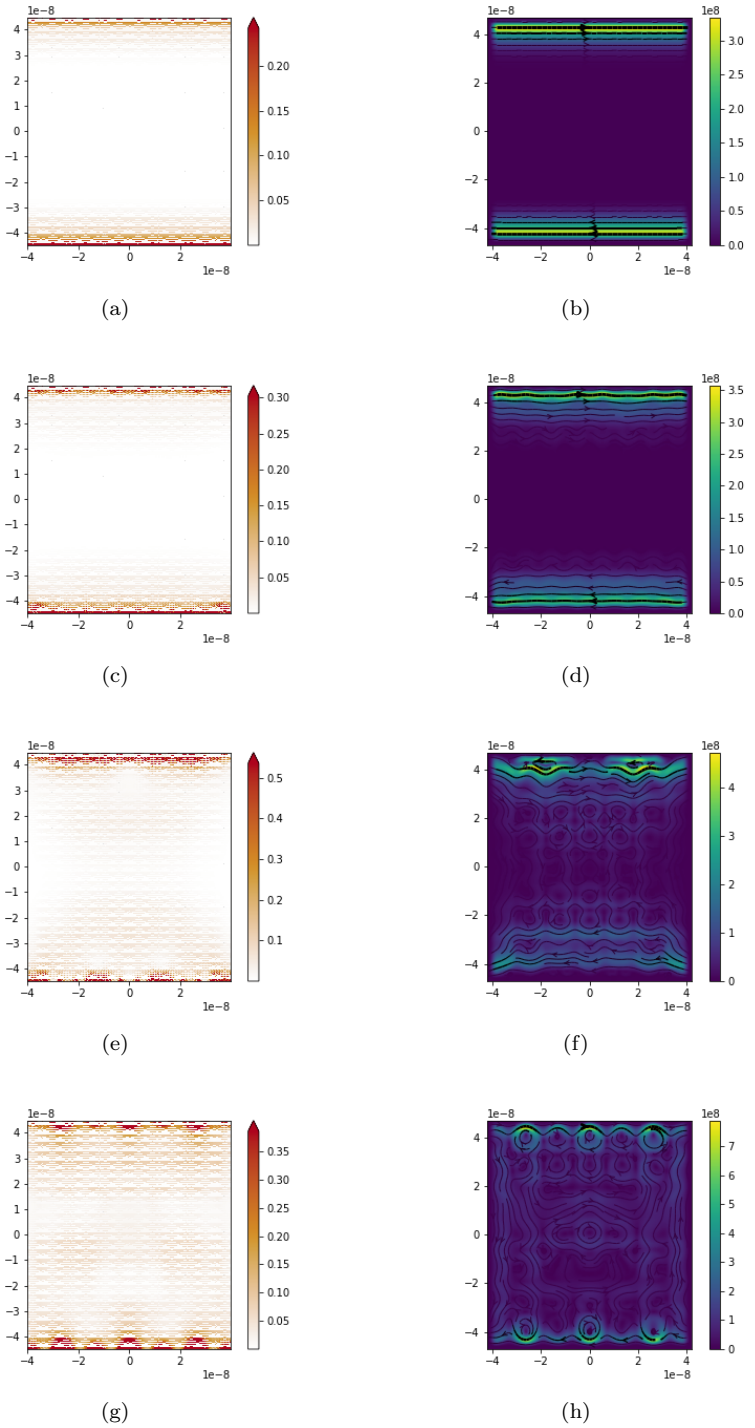

Figure 44: Density of states and current in arbitrary units for energy of $0.05eV$ with (a) and (b) Uniform $RSOC$ and exchange field, (c) and (d) $7800NPs/\mu m^2$, (e) and (f)$7100NPs/\mu m^2$, (g) and (h) $6700NPs/\mu m^2$. The system used is a nanoribbon of graphene with a width and a width of $90nm$ and a length of $80nm$. The hopping parameter is $t = -2.8eV$, the RSOC strength is $0.2eV$ and the exchange field strength is $0.1eV$.

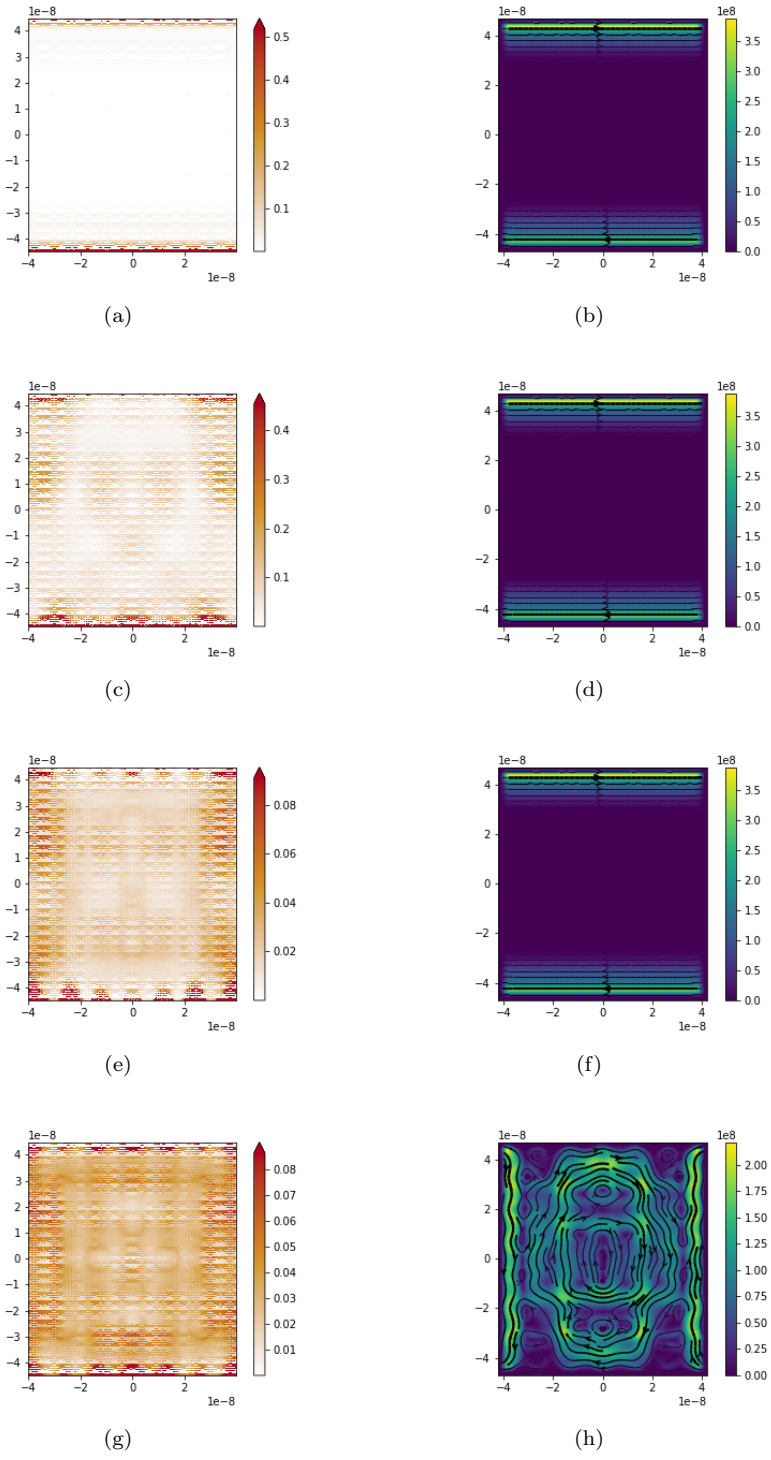

Figure 45: Density of states and current in arbitrary units for energy of $0.075eV$ with (a) and (b) Uniform $RSOC$ and exchange field, (c) and (d) $7800NPs/\mu m^2$, (e) and (f)$7100NPs/\mu m^2$, (g) and (h) $6700NPs/\mu m^2$. The system used is a nanoribbon of graphene with a width and a width of $90nm$ and a length of $80nm$. The hopping parameter is $t = -2.8eV$, the RSOC strength is $0.2eV$ and the exchange field strength is $0.1eV$.

4.1.6 Conclusion

As it can be seen from the results of the simulation, the presence of the RSOC and the exchange field leads to a topologically non-trivial band gap, as shown in figure 34. Indeed, when the Fermi level is in the band gap, edge states are observable (figure 36), which means that there is a quantum anomalous Hall effect in graphene. In addition, by adding two additional leads, a Hall resistivity of $\frac{1}{2}\frac{h}{e^2}$ and a zero longitudinal resistivity is obtained when the Fermi level is in the bulk band gap. As the purpose is to use the magnetite nanoparticles, the effect of a non-uniform RSOC and exchange field was studied. As it can be seen in figure 42, the conductivity, when the Fermi Level is in the bulk band gap, is still $2\frac{e^2}{h}$ meaning that even with a non-uniform RSOC and exchange field, the quantum anomalous Hall effect is observable.

Two important comments about these simulations need to be added. Firstly, an effect that was not taken into account in these simulations is the presence of a magnetic field. Indeed, to align all the magnetization direction of the magnetite nanoparticles, a small magnetic field (in the range of $100mT$ as shown in figure 32) has to be applied. Consequently, a combined effect of the classical Hall effect and the quantum anomalous Hall effect should be observed. Secondly, it is important to note that the results obtained in these simulations can not qualitatively compare with the experimental datas. Indeed, the RSOC and exchange field parameters are not determined experimentally and the density of nanoparticles used is relatively high and homogeneous, which has to be experimentally checked.

4.2 Ab-initio calculation

Density function theory (DFT)-based calculations were performed to determine the topologically non-trivial band gap induced in graphene due to the presence of magnetite. The principle of DFT is described in annex 10.5. In this case, the purpose of this simulation is to determine if the topologicaly non-trivial band gap is large enough to experimentally observe the quantum anomalous Hall effect. As we wanted to obtain an order of magnitude only, it was decided to only consider a Fe atom on top of the hollow position of a 4×4 supercell of graphene. This is represented in figure 46. The calculations were performed by using the Abinit software and the generalised gradient approximation exchange-correlation potential was used.

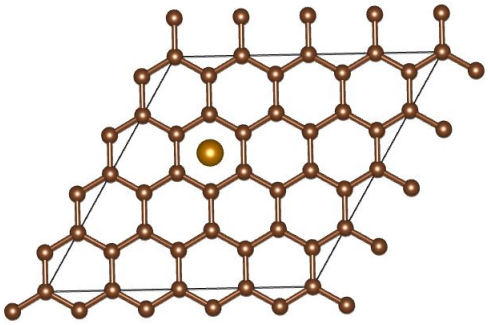

Figure 46: Representation of a Fe atom on top of the hollow position of a 4×4 supercell of graphene.

The first step of these calculations was the convergence study of, respectively, the unit cell of graphene and Fe with body center cubic structure. These results were obtained by using a norm-conserving fully relativistic pseudo-potential from Ref. [81] and are described in annex 10.6. The value of the cut-off energy was $42Ha$ and the grid of k-points was $5 \times 5 \times 1$. Then, the distance of the Fe atom obtained by structural relaxation is approximately 1.53Å, which is close to the value obtained in Ref. [49, 82]. From Ref. [49], which simulated the same system, it was expected to get a band gap of 5.5meV. Consequently, a smearing temperature of $4meV$ was used for the simulations.

Figure 47 represents the band structure and the density of state of the 4×4 supercell of graphene without iron atom.

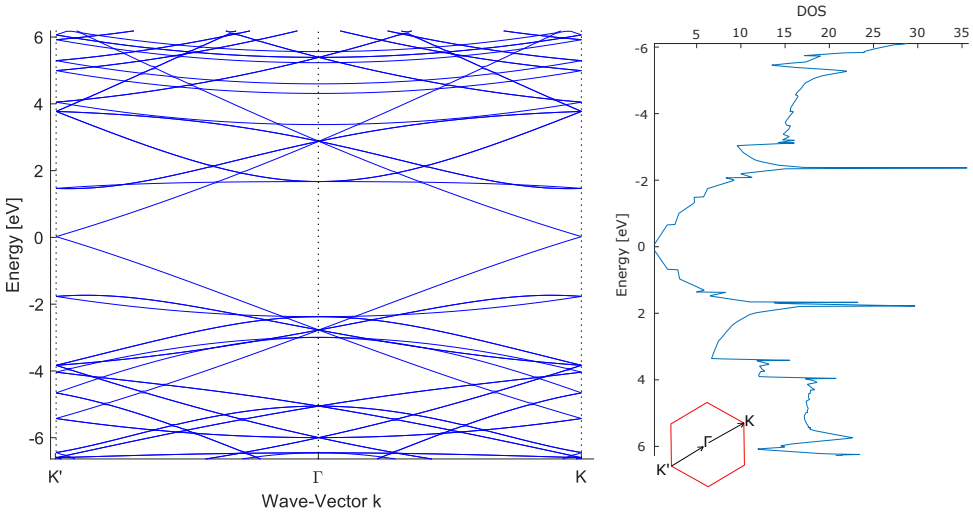

Figure 47: Band structure and density of states obtained for a 4×4 supercell of graphene.

The iron atom was then added at the hollow position. Figure 48 is obtained without taking into account the spin-orbit coupling, which leads to a band structure without band gap.

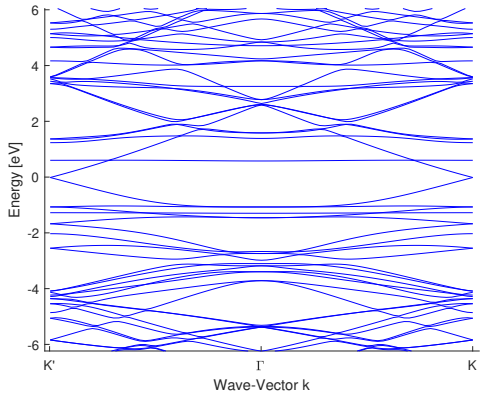

Figure 48: Band structure obtained for a 4×4 supercell of graphene with a iron atom at the hollow position without spin-orbit coupling.

Figure 49 is obtained including the spin-orbit coupling. Unfortunately, this band structure is not correct. Due to self-consistend field (SCF) convergence problems, it was decided to firstly calculate the wavefunctions for $0.27eV$ smearing temperature and, secondly use this wavefunctions file as a start point to facilitate the SCF convergence and obtain the band structure with $0.004eV$. However, with this technique, the same band structure was obtained with and without magnetization. The problem comes probably from the fact that the magnetization is particularly sensitive to the smearing temperature as explained in Ref. [83]. Consequently, the whole calculation has to be realized with $0.004eV$. At this point, we could not solve the problem.

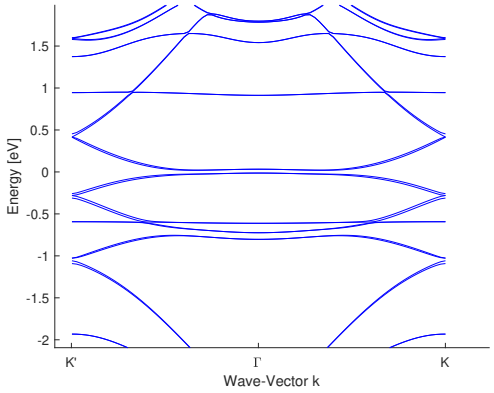

Figure 49: Band structure obtained for a 4×4 supercell of graphene with a iron atom at the hollow position by including the spin-orbit coupling.

By considering that the band gap obtained in Ref. [49], $5.5meV$, is the correct one, we can compare this value with the thermal energy kT, with k, the Boltzmann constant and T, the temperature. In order to expect to observe the quantum anomalous Hall effect, kT has to be lower than the band gap which is the case if the temperature is below 50 Kelvin.

In our case, the magnetite nanoparticles are composed of core made of oxygen and iron surrounded by an organic shell, which avoids the agglomerations and short-circuit. The exchange field, due to the hybridization between carbon π states of graphene and the

localised d-states of iron atom, and the Rashba spin-orbit coupling will be strongly reduced leading to a smaller band gap. Consequently, to expect to observe the QAHE, it is important to realize the measurement well below 50 Kelvin. In addition, a small magnetic field is still required in order to align all the magnetization of the nanoparticles in the same direction.

5 Experimental methods

5.1 The Raman Spectroscopy

5.1.1 Principle

The Raman spectroscopy is an non-destructive method used to characterize a sample. A monochromatic laser beam is applied to a sample and only the scattered photons are detected. In this case, the photon is absorbed by the sample due to the transition from the ground state to a virtual state. A new photon is immediately created and scattered because of a transition from the virtual state. Two different processes lead to the scattering of the incident light: Rayleigh scattering and Raman scattering[84].

The first one is due to the elastic interaction between the photon and the sample. Consequently, the energy of the scattered photon is the same as the energy of the incident photon. The second one is due to an inelastic scattering process. The scattered photon has a different energy from the energy of the incident photon [85]. With a Raman spectroscopy, this shift of the scattered photon is measured. This kind of scattering process can lead to two different families of peaks [86]:

- The Stokes peak: In this case, the frequency of the scattered photon is lower than the frequency of the incident photon. Indeed, a part of the energy of the initial photon is transferred to a vibrational mode of the crystal. This molecule occupies a higher vibrational energy state. In other words, the incident photon generates a phonon with a energy given by the difference between the energy of the scattered photon and initial photon.
- The anti-Stokes peak: In this case, the frequency of the scattered photon is higher than the frequency of the incident photon. Indeed, a part of the energy of the scattered photon comes from a vibrationally excited molecule, which ends up in a lower vibrational state. In other words, a phonon is annihilated and its energy contributed to the energy of the scattered photon.

In general, the x-axis of the Raman spectrum represents the Raman shift. The intensity of the peak depends strongly on the monochromatic laser used and on the acquisation parameters. Consequently, the y-axis is in arbitrary units.

5.1.2 Analysis of the Raman spectrum of graphene

In this section, the Raman spectrum of graphene will be shown and analyzed. In the case of this master thesis, four main peaks are useful and are called G, G',D and D' [87]. Figure 50(a) shows the spectra of a perfect mechanically exfoliated graphene without any structural defects. Only the peaks G and G' are observed.
Figure 50(b) represents the phonon dispersion in the high symmetry line of the hexagonal lattice. As the unit cell of the graphene is composed of two carbon atoms, there are 6 phonon dispersion bands. However, the presence of the other peaks, which are given in figure 51, is due to defects.
The different mechanisms which are responsible for the different peaks are presented in figure 52.

5.1.2.1 The G peak

As represented in figure 52 for the G peak, a incident photon is absorbed. This generates an electron-hole pair. They can recombine, leading to the emission of a photon of the same energy or they can create a phonon before recombination, which is represented by the dark arrow. The Raman frequency shift is situated at $1581cm^{-1}$ for single monolayer graphene. This peak is the only one associated to a first-order Raman scattering process [87].

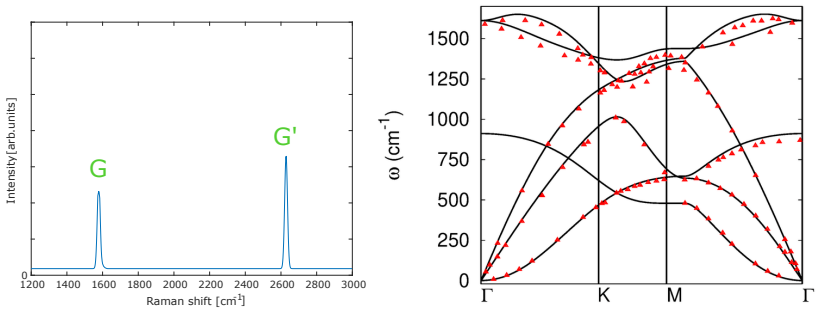

(a) (b)

Figure 50: (a)Example of a Raman spectrum in the case of perfect graphene with $\lambda = 514nm$ for the laser. (b) Phonon dispersion in the high symetry line of the hexagonal lattice obtained in Ref. [88] by using the experimental data of Ref. [89] represented by the red triangles.

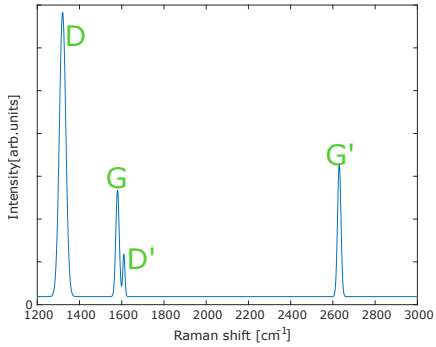

Figure 51: Example of a Raman spectrum in the case of graphene with structural defects with $\lambda = 514nm$ for the laser.

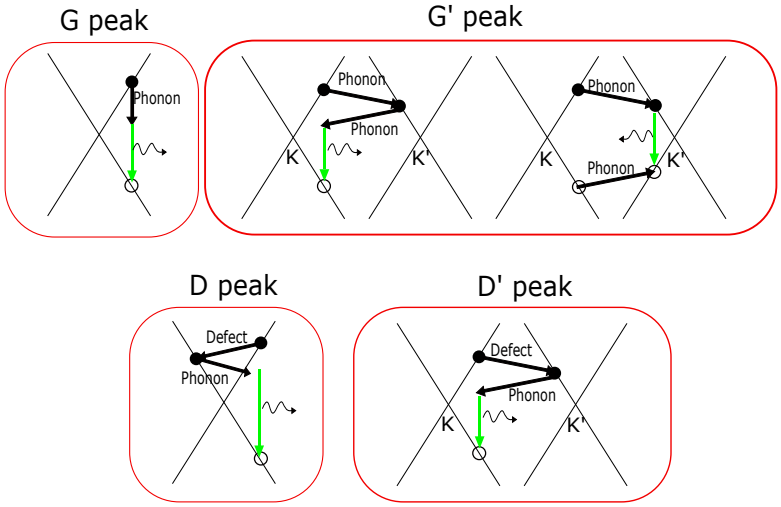

Figure 52: Schematic representation of the different scattering processes responsible for the main peaks present in the graphene Raman spectrum.

5.1.2.2 The G' peak

The G' peak is due to a second-order inter-valley Raman scattering [87] and is represented in figure 52. Two situations can explain this peak:

- A double resonance process: this process starts with the excitation of an electron around K by absorbing the incident photon with a wavevector $\boldsymbol{k}$. The electron is then inelastically scattered by a ITO phonon with a certain energy and a wavevector $\boldsymbol{q}$ around the K'. Consequently, the wavevector of the electron is $\boldsymbol{k}+\boldsymbol{q}$. The electron and hole are in different valleys. They can not recombine. The electron is then scattered back to its initial wavevector by another ITO phonon with a wavevector -$\boldsymbol{q}$ and then recombines with the hole by emitting a photon.

- A triple resonance process: this process is basically the same as the first. However, the hole will scatter in the same valley as the electron before the electron scattered back. Consequently, they will recombine in the other valley.

The Raman frequency shift is situated at $2630cm^{-1}$. For single monolayer graphene, the full width at half maximum (FWHM) is approximately $30cm^{-1}$ [90, 87, 91]. In addition, if this peak can not be fitted by a single Lorentian, the graphene is multilayer.

Consequently, the Raman spectrum can determine whether the graphene is monolayer or not. Indeed, if:

- FWHM of the G' peak is approximately equal to $30cm^{-1}$; and

- G' peak can be fitted by one Lorenztian [87] (indeed, adding several layers of graphene will split the G' peak into different modes); and

- the ratio $\frac{I_{G'}}{I_G}$ is higher than 1;

then, the graphene is monolayer.

5.1.2.3 The D peak

The D peak is due to a second-order inter-valley Raman scattering [87] and is also represented in figure 52. This process is exactly the same as the Double resonance process involved in the G' peak. However, the first scattering of the electron is due to a defect present in the graphene lattice. The Raman frequency shift is situated at $1320cm^{-1}$.

5.1.2.4 The D' peak

The D' peak is due to a second-order intra-valley Raman scattering. Firstly, the electron is scattered by defect. Secondly, the electron is scattered by a phonon. The Raman frequency shift is situated at $1610cm^{-1}$.

5.1.3 Structural defect in Raman spectroscopy of monolayer graphene

Structural defects represent anything that can lead to an inversion symmetry breaking in graphene like vacancy sites, grain boundaries, interstitial atoms, substitutional atoms or adatoms [91].

The Raman spectroscopy can be used to determine the level of disorder in graphene by analyzing the ratio between the D and G peaks, $\frac{I_D}{I_G}$. Two different regimes are identified [91]. The first one, called *low density defect regime*, refers to the nanocrystalline graphene phase. The second one, called *high defect density regime*, refers to the amorphous carbon phase. These two regimes derive from the presence of two specific radius. The first one, r_s, represents the direct structural disorder area. The second one, r_a, represents the area close enough to the defect to be activated. As the D peak is weakly influenced by the the first one, the "low defect density" is generally obtained when $L_D > 2r_a$ with L_D the average distance between two defects [92].

In the first regime, when the density of the defect increases, a D peak appears that increases the ratio $\frac{I_D}{I_G}$. The other peak, G', broadens and decreases in intensity. In the case

of rare defects, the I_D peak is proportional to the total number of defects probed by the laser. Indeed, the D peak is only produced in the region close to a defect. Consequently, if the laser spot size is L_L, the average number of defects is $(\frac{L_L}{L_D})^2$ leading to:

$$I_D \propto (\frac{L_L}{L_D})^2 \tag{83}$$

As the G peak intensity is proportional to the area of the graphene covered by the laser spot, the ratio becomes:

$$\frac{I_D}{I_G} = \frac{C}{L_D^2} \tag{84}$$

with C, a constant that depends on the wavelength of the laser used. This formula was firstly obtained by Tuinstra and Koenig in graphite [93] and was extended to graphene [94]. In Ref. [95], an empirical expression of C was obtained, leading to a direct expression of the concentration of structural defects in graphene:

$$n_D(cm^{-1}) = \frac{(1.8 \pm 0.5) \times 10^{22}}{\lambda_L^4} \frac{I_D}{I_G} \tag{85}$$

with λ_L, the laser wavelength in nm.

When the number of defects becomes important, the D peak reaches a maximum value and any further increase of the defects will reduce the intensity of the D peak. Indeed, graphene is now dominated by a structural disorder area. Consequently, equation 85 is no longer correct. Instead, Ferrari's formula from Ref. [96] can be used:

$$\frac{I_D}{I_G} = C' L_D^2 \tag{86}$$

with C', a constant depending on the wavelength of the laser. In the case of $\lambda_L = 514nm$, $C' = 0.0055$.

Figure 53 represents the evolution of the ratio $\frac{I_D}{I_G}$ as a function of the average distance between defects obtained in Ref. [95]. To change the average distance, they bombarded graphene with Ar^+ ions with different doses. The same kind of results were obtained in Ref. [97].

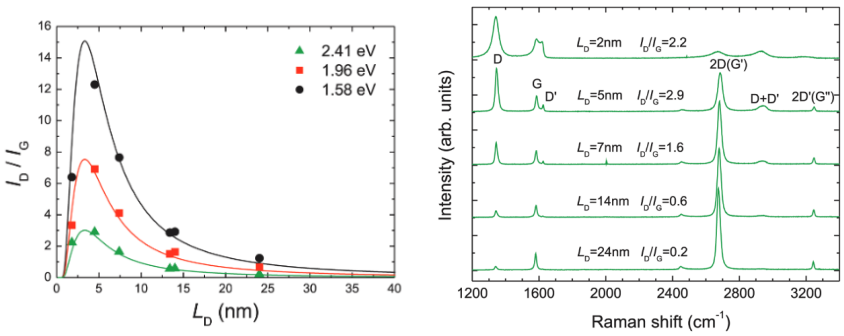

(a) (b)

Figure 53: (a) $\frac{I_D}{I_G}$ for single monolayer graphene for different laser energies in function of the average distance between defects. The datas were obtained by bombarding graphene with Ar^+ ions with a dose varying from $10^{11} Ar^+/cm^2$ to $10^{15} Ar^+/cm^2$.(b) Raman spectrum obtained for single monolayer of graphene for different doses of Ar^+ ion. The measures were obtained by using a laser with a wavelength of $\lambda_L = 514.5nm$. The data are from Ref. [95].

5.2 The Atomic Force Microscopy

The Atomic Force Microscopy (AFM) is based on the interaction between a probe and a sample leading to a topographic image of the sample. A conventional AFM consists in a sharp tip, a micro spring cantilever and a 4-quadrant position sensitive photo-diode. Tips used are generally made of silicon or silicon nitride. The cantilever is used as a sensor to detect the probe-sample interaction.

When the tip approaches the surface, the Van Der Waals force leads to the attraction between the tip and the surface. In this case the effective force is attractive and the cantilever bends downward. When the distance becomes shorter, in the magnitude of a few angstroms, the repulsive Colombic forces become dominant and the cantilever bend upward. The force-distance curve is represented in figure 54 [98].

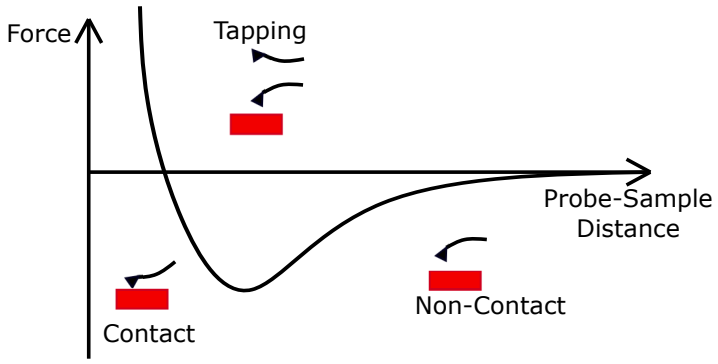

Figure 54: Force in function of the distance between the probe and the sample. Three different modes are used, depending on the distance: contact, tapping and non-contact modes.

The normal force between the probe and the sample is calculated using the Hooke's Law:

$$F = k\Delta z \tag{87}$$

with k, the spring constant of the cantilever and Δz, the bending in z-direction. To measure the bending of the cantilever, a laser beam is focused onto the end of the cantilever. Then, the laser is reflected and hit the position sensitive photo-diode. When the cantilever is bent, the reflected laser beam will move and the bending of the cantilever can be measured precisely. This information is sent to a piezoelectric material which will move the probe to maintain a constant force between the probe and the sample. The displacement in the z-direction is used to form a topography image of the sample [98].

As presented in figure 54, three different modes can be used in function of the distance between the tip and the sample:

- Contact mode;
- Tapping mode;
- Non-Contact mode.

In contact mode, the tip is in soft physical contact with the surface. Consequently, as the forces involved are repulsive, the cantilever will bend away from the surface. A constant deflection is maintained using a feedback loop. The main disadvantage of this technique is that the tip can damage or deform the surface of the sample. However, this technique allows a better resolution than in non-contact mode.

In non-contact mode, the forces are dominated by the Van der Waals forces. The tip is not in contact with the surface of the sample but oscillates above the surface. A feedback

loop is again used to detect the change in deflection of the cantilever. Despite the fact that it does not damage the surface of the material, this technique leads to a lower resolution than the first one.

In tapping mode, the tip is intermittently in contact with the sample. Indeed, the cantilever oscillates at its resonance frequency. In this case, the feedback loop is used to maintain a constant amplitude of oscillation. This technique prevents the damages of the surface induced by the tip.

6 Synthesis of graphene

In this section, two techniques of graphene synthesis will be briefly presented. The first one is the mechanical exfoliation of graphene from higly oriented pyrolytic graphite (HOPG) and the second one will be the chemical vapor deposition of graphene on a Cu foil.

6.1 Mechanical Exfoliation

Mechanical exfoliation of graphene is realised from HOPG. An adhesive tape is used to transfer flakes of graphite onto a substrate [99]. Then, flakes of graphene are identified. The different steps are given in figure 55.

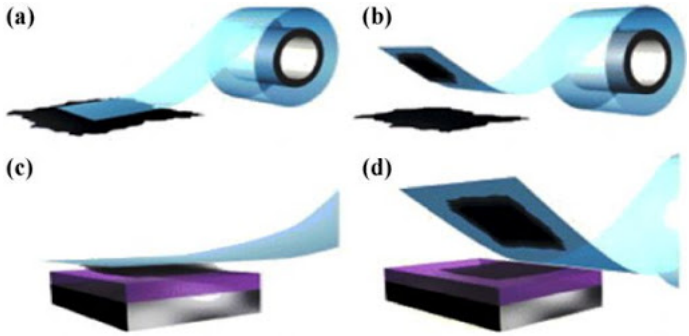

Figure 55: Steps of the mechanical exfoliation of graphene. (a) A tape is pressed onto the high quality graphite crystal. (b) The tape is removed and graphite layers are sticked on it. (c) The tape is pressed against a Si/SiO_2 substrate and (d) removed softly. Figure from Ref. [100]

The main advantages of these techniques are: its low cost and a high quality of the obtained graphene, which is the best at this moment. However, the films obtained are irregular and cannot exceed a few μm making them difficult to use for the large-scale productions.

6.2 Chemical Vapor Deposition

Chemical vapor deposition (CVD) is a large-area deposition compared to the previous technique [101]. The precursors used to form graphene are methane, hydrogen and argon, which are inserted inside a quartz tube containing a Cu substrate. The general set-up used is represented in figure 56, which is the case of a thermal chemical vapor deposition.

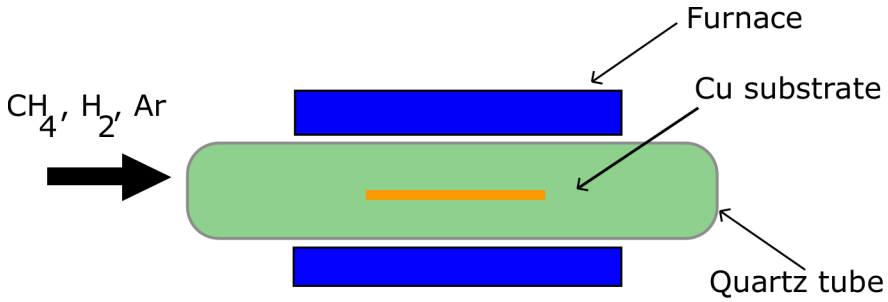

Figure 56: Representation of the CVD set-up. The precursors are introduced inside quartz tube. They will react at the surface of a Cu substrate to form graphene.

The graphene is obtained by decomposition of the methane gaz at 1000°C, which will be the source of the elemental carbon that will crystallize on the surface of the copper

to give graphene. Graphene will first grow in different domains that will eventually join. With this technique, it is indeed not rare to find domains with different orientations that can lead to inter-domain defects. The resulting graphene must now be transferred to the surface of an Si/SiO_2 substrate. To do this, a PMMA layer is generally deposited on the surface by spin-coating to protect and support the graphene. The copper is then etched. Different solutions can be used such as: $FeCl_3$, HCl, HNO_3, $Fe(NO_3)_3$. The graphene can then be deposited on the substrate and the PMMA is coated with acetone [102]. All these steps are represented in figure 57.

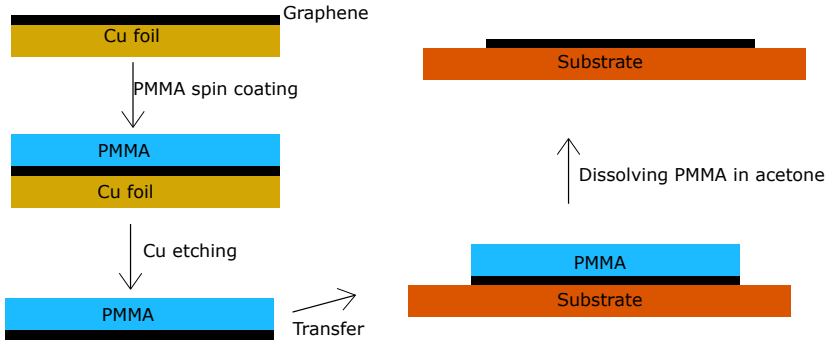

Figure 57: Steps of the transfer of graphene on Si/SiO_2 substrate.

The advantage of this technique is the possibility to produce graphene samples significantly larger than those obtained by mechanical exfoliation and allows a larger scale production. However, the quality is not so good compared to mechanically exfoliated one. Due to boundaries during the growth and all transfer steps which add contamination on the surface of graphene.

7 Sample preparation

In this section, the sample used will firstly be presented. Then, the different treatments of the samples will be detailed. Indeed, as explained in section 1.3.2, the contaminants present at the surface of graphene and at the interface between the oxide and the graphene can lead to shift the Dirac point. As the purpose of this master thesis is to deposit nanoparticles, we wanted to ensure that the surface of graphene was clean of contaminants to avoid any perturbations of the future measured characteristics. All measurements presented below were performed at room temperature and at $1e^{-6}mbar$ using the lock-in amplifier technique.

7.1 Sample Presentation

The chips used for the measurements were realised by Graphenea[1]. Each graphene device has either 6 contacts, allowing 4-probes measurements, or 2 contacts as represented in figure 58 from the website of Graphenea [2].

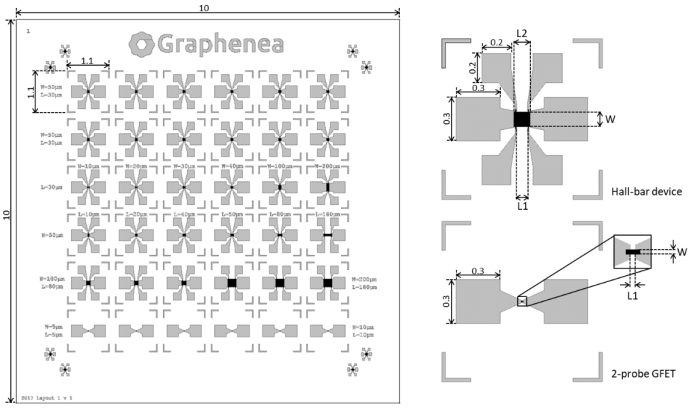

Figure 58: Chip fabricated by Graphenea. Each Graphene device possesses 6 or 2 contacts and possesses a width of W and a length of L_2 .

Graphene has been obtained by chemical vapor deposition on copper foil with a dominant orientation of (100) and a surface rougness around $100nm$. Then, to transfer the graphene on top of a silicon-silicon dioxide substrate, a sacrificial layer of $60nm$ of polymethyl methacrylate (PMMA) was deposited to protect the graphene. Copper is then etched in a ferric chloride solution. The stack PMMA/graphene is then deposited on the Si/SiO_2 substrate. The PMMA is removed with the acetone. The chip thickness is $675\mu m$ with a gate oxide of $90nm$. The contacts are in Cr/Au. The device is presented in figure 59.

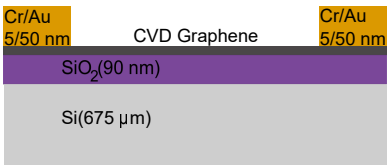

Figure 59: Side-view of the graphene device produced by Graphenea.

To connect a gold wire to the back gate, a cotton swab previously immersed in hydrofluoric acid was used to etch the thin film of oxide under the chip.

We measured the ambipolar effect of the studied sampled. Figure 60 gives the result

[1] https://www.graphenea.com/

[2] https://www.graphenea.com/collections/buy-gfet-models-for-sensing-applications/products/gfet-s10-for-sensing-applications-10-mm-x-10-mm

obtained for one of our samples. The Dirac point is between 50 and 65V, which was the case for all the samples measured.

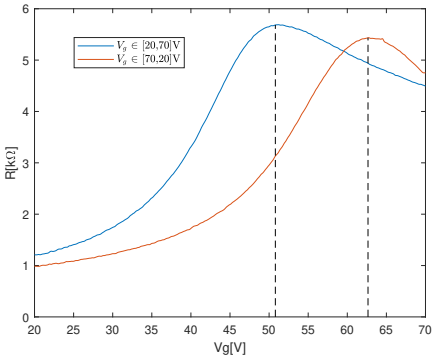

Figure 60: Measurement realized on a Hall Bar of $30 \times 50\mu m$ before cleaning. An alternative current of $10nA$ with a frequency of $413Hz$ flowed between the two contacts. The blue and the red lines were obtained by varying the back gate voltage V_g from 20 to $70V$ and from 70 to $20V$ with a jump and an acquisition time of $0.05V$ and $300ms$ respectively.

As represented in this figure, the Dirac point is significantly shifted from $0V$ expected for pristine graphene. This can be explained by the presence of water [103], oxygen, carbon dioxide[104], organic residues adsorbed at the surface of graphene or at the interface between graphene and the substrate during the fabrication process. Indeed these impurities can be physically adsorpted and can play the role of acceptors. Consequently, some free electrons in graphene can be trapped, thereby leading to a change in the balance between the holes and the electrons [105, 106, 107, 108]. The graphene is p-doped and, as explained in section 1.3.2, the Dirac point is shifted to a positive value. Cleaning the surface of graphene can allow us to remove all the dopants and bring Dirac point closer to 0V. All the cleaning steps are presented in the next section

An hysteresis can be also observed in figure 60. This effect can be explained by the injections of charges into the trap centers present at the graphene/oxide interface or in the bulk of the oxide. Indeed, when the back gate voltage starts at a negative value and is increased, the holes are slowly trapped by the trap centers. The potential feels by the graphene is higher than the one from the back gate. Consequently, the Dirac point is shifted down. On the other hand, when the back gate voltage changes after the Dirac point, electrons start to be injected into the trap centers. Consequently, when the sweeping is in the opposite direction, the Dirac point is shifted up [106, 109].

7.2 Cleaning of the sample

7.2.1 24 hours in acetone

In this section, two samples and their characteristic curves will be presented. The first one called G_1 has dimensions of 30×50 μm. The second one, called G_2, has dimensions of 50×50 μm.

The first step of the cleaning process was to put the sample in acetone during 24 hours to remove a maximum of impurities at the surface of graphene which could induce a shift of the Dirac point. Figure 61 is obtained using AFM in tapping mode on the sample G_2 after cleaning with acetone. In figure 61(b), ripples and impurities can be observed.
As shown in figure 62, this first cleaning step allows to significantly shift down the Dirac point.

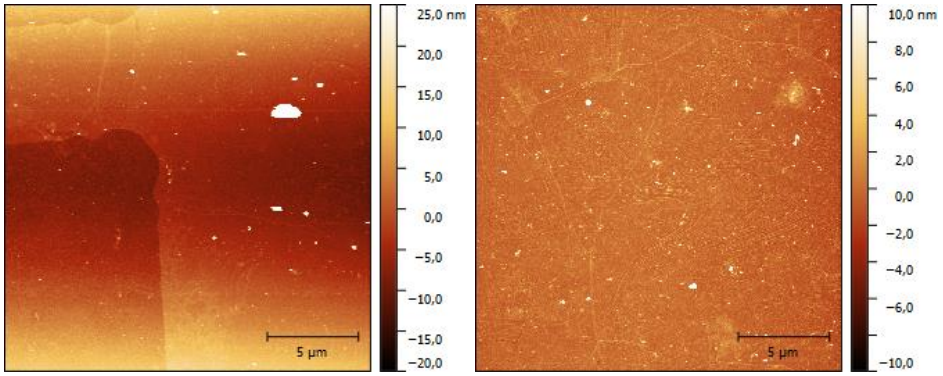

(a) (b)

Figure 61: Images obtained by AFM in tapping mode on G_2.

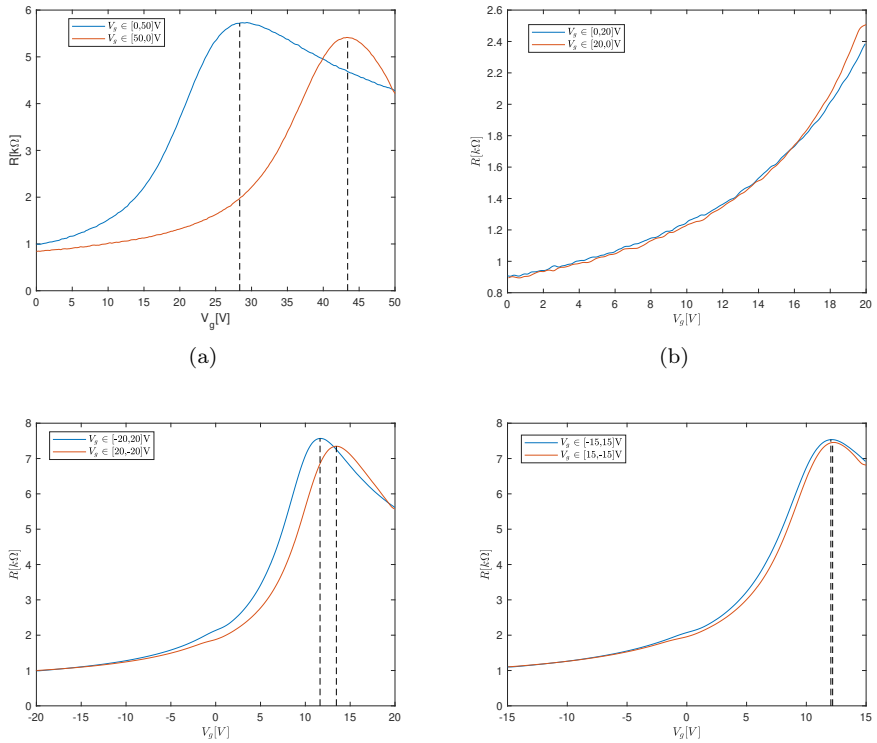

(a) (b)

(c) (d)

Figure 62: (a) and (b) are realised on G_1 after cleaning with acetone. An alternative current of $10nA$ with a frequency of $413Hz$ flowed between the two contacts. In (a), the blue and red curves are respectively obtained by varying the back gate from 0 to $50V$ and from 50 to $0V$. In (b), the blue and red curves are respectively obtained by varying the back gate from 0 to $20V$ and from 20 to $0V$. (c) and (d) are realized on G_2. An alternative current of $20nA$ with a frequency of $413Hz$ flowed between the two contacts. In (c), the blue and red curves are respectively obtained by varying the back gate from -20 to $20V$ and from 20 to $-20V$. In (d),the blue and red curves are respectively obtained by varying the back gate from -15 to $15V$ and from 15 to $-15V$.

As presented in figures 62 (b) and (d), applying a lower gate voltage allows to reduce the hysteresis. This is also experimentally demonstrated in Ref. [106]. Indeed, the charge carriers are injected into the interface trap centers at every back gate voltage. However,

to fill the bulk oxide traps, a higher voltage is required. By decreasing the interval, only interface traps are filled, leading to a lower hysteresis.

The sample G_2 with a Dirac point at approximately $12V$ was different compared to the other one we used and was kept under vacuum without any additional cleaning steps, to be used for the functionalization with magnetite nanoparticles. The other samples, after a cleaning with acetone, had a Dirac point between 30 and $42V$ as represented in figure 62(a) for the sample G_1.

From measurements in figure 62 (d), the mobility of charge carriers was calculated using equation 23 in the linear parts. The mobility of the holes is $970cm^2/Vs$ and the mobility of the electrons is $145cm^2/Vs$. These mobilities correspond to the specifications of Graphenea.

7.2.2 Mechanical cleaning with Atomic Force Microscopy in contact mode

In this section, two samples, G_1 and G_3 already cleaned with acetone are used. The dimensions of G_3 are $50 \times 50\mu m$.

After cleaning in acetone, AFM in contact mode was used to mechanically clean the surface of graphene to shift down the Dirac point. This has already been presented in many references such as Ref. [110, 111]. The principle of Atomic Force Microscopy was explained in section 5.2. The purpose of this technique at this step is to push away the impurities present that were not removed by acetone. Figure 63 is an image obtained by the optical microscope before and after the mechanical cleaning.

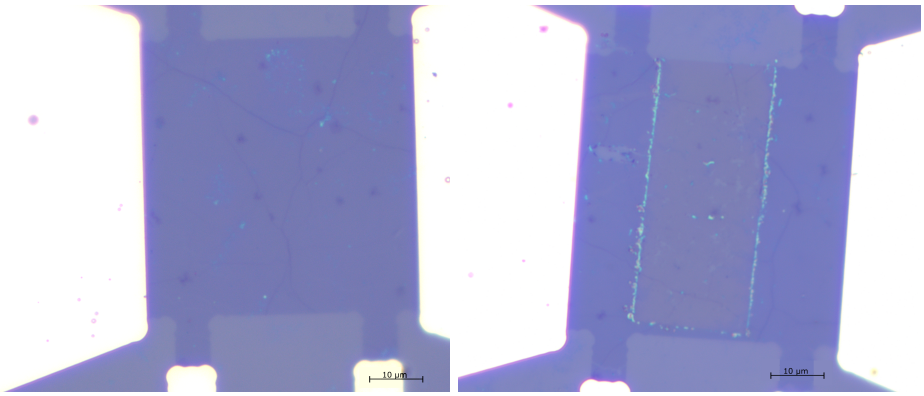

(a) (b)

Figure 63: Optical microscope image taken (a) before and (b) after the mechanical cleaning with AFM for a sample of G_3.

As shown in these figures, many impurities were pushed away and formed walls. Unfortunately, the Hall bar was too large to clean up the entire surface of the graphene without bringing back the impurities in the cleaned areas.

The graphene is still present as can be seen with the contrast between the silicon dioxide and graphene in figure 63(b). In addition, a Raman spectroscopy was realized and the spectrum is given in figure 64. The raw data are in annex 10.7.
As explained in section 5.1, the Raman spectrum presented in figure 64 is a signature of monolayer graphene. The FWHM of G' peak at $2694cm^{-1}$ is approximately $45cm^{-1}$ and the ratio $\frac{I_{G'}}{I_G}$ is equal to 1.39. A larger FWHM than $30cm^{-1}$, as represented in section 5.1, is explained by the presence of defects that broadens the G' peak. The presence of defects is highlighted by the presence of the D peak at $1347cm^{-1}$ inducing a ratio $\frac{I_D}{I_G}$

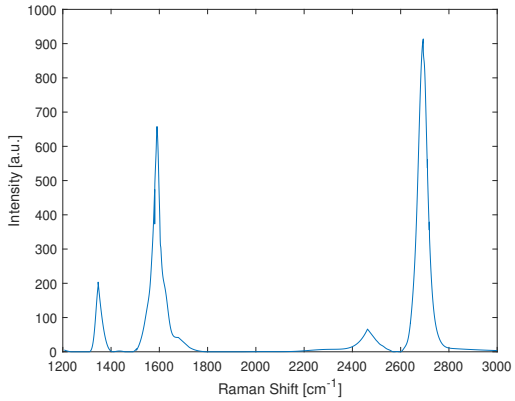

Figure 64: Raman spectrum obtained with $514.5nm$ laser of mechanically cleaned part of the G_3 by AFM in contact mode.

equal to 0.31. By considering that we are in the regime of low density of defects, the equation 85 can be used. Consequently, the concentration of structural defects is:

$$n_D = 7.96 \times 10^{10} cm^{-1} \tag{88}$$

Then, electrical measurements were realized. The results for G_1 and G_3 are given in figure 65.

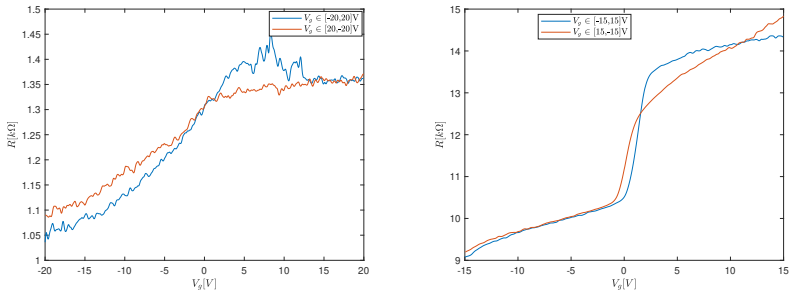

(a) (b)

Figure 65: (a) was realized on G_1 after cleaning with AFM. An alternative current of $10nA$ with a frequency of $413Hz$ flowed between the two contacts. The blue and red curves are respectively obtained by varying the back gate from -20 to $20V$ and from 20 to $-20V$. (b) was realised on G_3 after cleaning with AFM. An alternative current of $20nA$ with a frequency of $413Hz$ flowed between the two contacts. The blue and red curves are respectively obtained by varying the back gate from -15 to $15V$ and from 15 to $-15V$.

These results do not highlight the ambipolar electric field effect in graphene as explained in section 1.3.2. Indeed, the resistance increases slowly until it reaches a voltage of zero. The resistance makes a jump and then continues to increase slowly. Until now, the origin of this peculiar behaviour is not understood. One theory is that the walls create a channel inducing a short circuit when the gate voltage varies. This should mean that most of the impurities pushed away by the AFM are metallic which may be explained by the fact that, during the wet transfer of CVD graphene, the copper is not totally etched and iron particles are still present after the transfer. However, the walls are probably composed of some residual PMMA. Of course, more characterizations of the surface are required.

7.3 Etching by Focused-Ion Beam

The Focused-Ion Beam (FIB) technique uses a beam of ions of gallium to image a sample or, if a high current is used, to sputter material in a controlled fashion, for example to etch away different layers with a geometric pattern. Indeed, ions will hit the surface and sputters a small amount of material.

In this section, two other samples, called G_4 and G_5, were used. Their dimensions are respectively $50 \times 50\mu m$ and $180 \times 50\mu m$.

The first reason to use FIB in this master thesis is to reduce the size of the used Hall bar. The smaller area can afford us an easier enumeration of deposited nanoparticles. The second reason is to reduce the region to be cleaned by AFM and push all the contaminants out of the surface of graphene. Figures 66 (a) and (c) show two different samples after applying the FIB with gallium-ions.

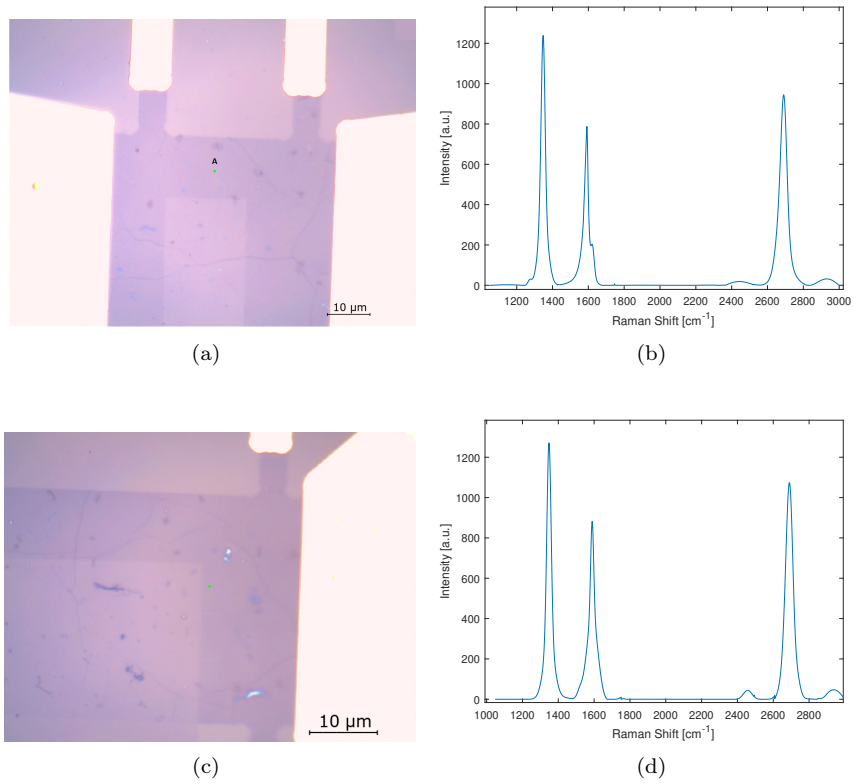

(a) (b)

(c) (d)

Figure 66: (a) and (c) are optical microscope images after FIB on (a) G_4 and (c) G_5. The Ga-ions energy is $50keV$ with a current of (a) $120pA$ and (c) $50pA$. (b) and (d) are the Raman spectra obtained with a laser of $514nm$ on the Hall bar.

To confirm the presence of graphene in the Hall bar, a Raman spectrum was recorded for each sample. The spectra where the background is removed, are given in figure 66 (b) and (d) (see raw data in annex 10.7). As for figure 64, monolayer of graphene is still present. Indeed, for G_4, the FWHM of G' peak at $2690cm^{-1}$ is approximately $48cm^{-1}$ and the ratio $\frac{I_{G'}}{I_G}$ is equal to 1.19 and for G_5 ,the FWHM of G' at $2690cm^{-1}$ is approximately $50cm^{-1}$ and the ratio $\frac{I_{G'}}{I_G}$ is equal to 1.22. However, the density of defects increased, leading to a ratio $\frac{I_{D'}}{I_G}$ equal to 1.579 and 1.45 for G_4 and G_5 respectively. Larger FWHM than $30cm^{-1}$, as represented in section 5.1, is explained by the presence of defects that broadens the G' peak.

Firstly, the defect peak comes from the tail of the Ga-ions beam. Indeed, unwanted area were exposed to Ga-ions inducing structural defects. Secondly, this is due to the image taken with the FIB. Indeed, it was necessary to take images to determine the area we wanted to remove graphene, leading to gallium-ions exposition over the whole surface of graphene . This also led to structural defects. The defects in graphene due Gallium ions were also studied in Ref. [112, 113].

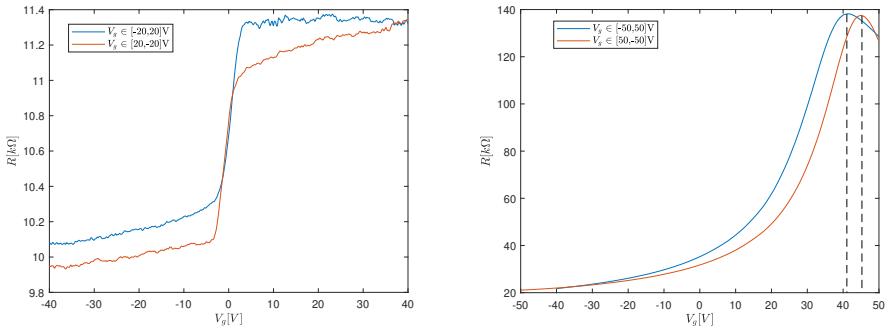

(a) (b)

Figure 67: Measurements realized (a) G_4 and (b) G_5 after the FIB. The Ga-ions energy is $50keV$ with a current of (a) $120pA$ and (b) $50pA$. An alternative current of $20nA$ with a frequency of $413Hz$ flowed between two contacts. The blue and red curves are respectively obtained by varying the back gate voltage (a) from -40 to $40V$ and 40 to $-40V$, (b)from -50 to $50V$ and 50 to $-50V$.

Figure 67 give the measurements realized with the samples shown in figure 66.

Figure 67(a) is exactly the same as the one obtained after the AFM cleaning. In this case, there are no channels created by the impurities as it was the case after the cleaning with AFM. We could not find any theories that could explain this result.

Figure 67 (b) shows a Dirac point between 41 and $45V$. In addition, using the equation 23, the hole and the electron mobility are respectively 15 and 2 $\frac{cm^2}{Vs}$. This low value compared to the ones obtained before is directly due to important number of structural defects due to Ga-ions. This sample can also be used for functionalization to determine the effect of disorder on the quantum anomalous Hall effect and see the difference in the deposition of the nanoparticles on the surface with structural defects.

8 Synthesis of magnetite nanoparticles

In this section, the synthesis of magnetite nanoparticles (NPs) will be presented. In the first subsection, the materials and the methods used will be described. In the second subsection, the results will be presented. The synthesis method is based on Ref. [114] and Ref. [115].

8.1 Materials and methods

The setup used for the synthesis of the nanoparticles is presented in figure 68.

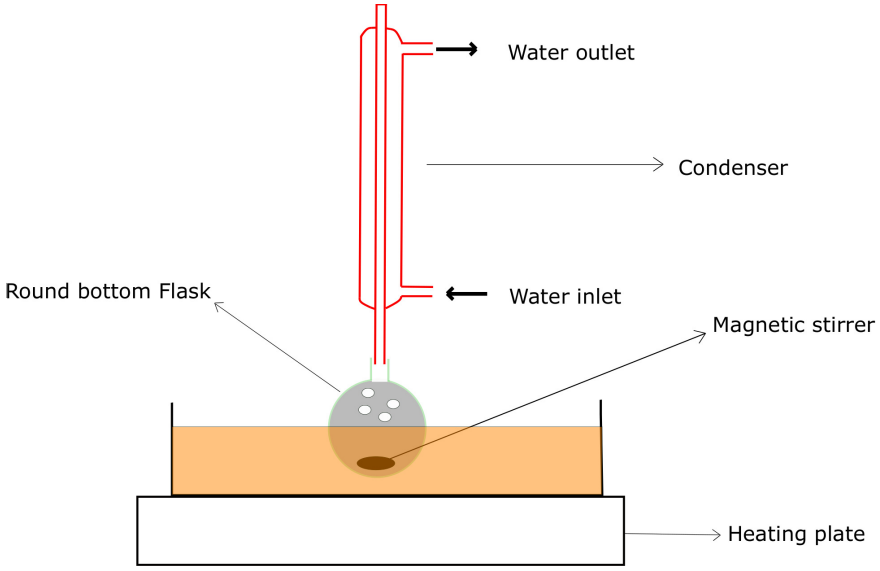

Figure 68: Setup used for the synthesis of nanoparticles. In red, the condenser, in green the round bottom flask and in dark, a magnetic stirrer which allows to stirr the solution to obtain a uniform temperature.

The formation of the magnetite is based on the thermal decomposition of iron acetylacetonate, $Fe(acac)_3$. In addition, the adsorption of the oleylamine, $C_{18}H_{35}NH_2$, at the surface of the iron oxide, leads to the formation of well separated nanoparticles which are illustrated in figure 69. Dioctyl ether is used as a solvent due to its high boiling point (268 °C). For this procedure, 0.35 g of $Fe(acac)_3$, 5ml of $C_{18}H_{35}NH_2$ and 5ml of dioctyl ether were used.

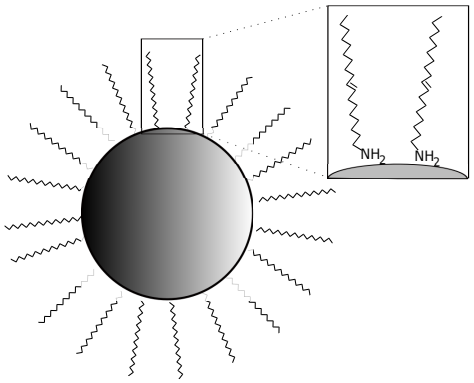

Figure 69: Magnetite core surrounded by a shell of oleylamine modified from Ref. [114].

The first step of the process was to put the whole setup under vacuum and subsequently

fill it with argon. This step was repeated three times to remove as much air as possible. The three products were then added in the round bottom flask represented in figure 68 and the bath was heated. When the temperature of the bath reached $110°C$, the system was stirred during one hour. Then, the temperature of the oil was increased until $300°C$. The water flux through the condenser was activated at this moment to avoid loosing vapors of the solvent. After one hour of reaction, the system was left to cool down. Finally, ethanol was added to precipitate the nanoparticles. Finally, the nanoparticles are stored in hexane.

The solution was introduced in a centrifuge during four minutes at 6000 rpm. The nanoparticles sedimented at the bottom of the tube. It was then easy to discard the supernatant and replace this removed-volume by ethanol. This step was repeated three times to wash the nanoparticles.

8.2 Result

Figure 70 shows the result obtained at the end of the synthesis.

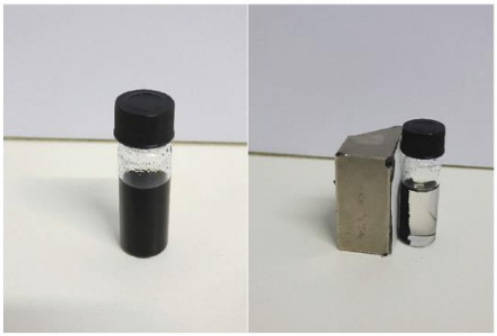

Figure 70: Nanoparticles, in dark, obtained at the end of the synthesis procedure. In grey, a magnet allowing to conclude that the nanoparticles are magnetic.

Figures 71 are obtained using the transmission electron Microscopy(TEM). The dark spheres represent the magnetite nanoparticles. The largest one are probably obtained by the agglomeration of small nanoparticles.

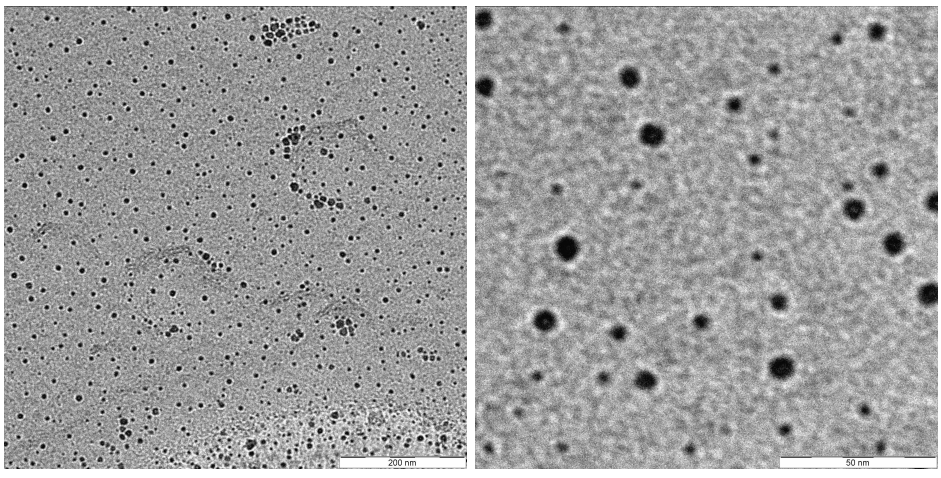

(a) (b)

Figure 71: TEM image obtained by depositing a droplet of hexane containing the nanoparticles on a lacey carbon film on copper grid.

9 Deposition of magnetite on graphene

It was decided to use the sample G_2 to deposit the nanoparticles. A small droplet of hexane containing the nanoparticles was deposited on the sample. The sample was then rapidly rinsed with acetone and isopropanol to remove the solvent residue. Figures 72 are obtained by using the scanning electron microscopy (SEM). The nanoparticles are in white in the images and the graphene in dark. In figure 72(b), a nanoparticle with a diameter of $20nm$ is observable. Smaller nanoparticles are also present below this $20nm-$diameter nanoparticle. We concluded that the small particles are the elementary particles and that they have formed, by agglomeration, larger particles such as the one visible in the figure 72(b).

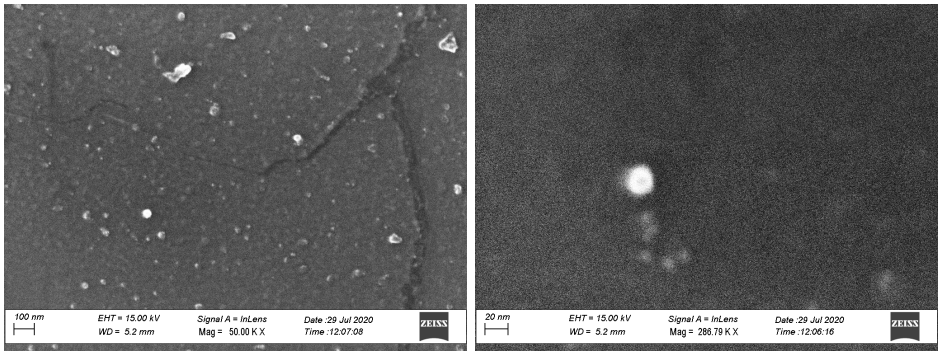

(a) (b)

Figure 72: SEM images of the sample G_2 with electrons of energy $15keV$.

To confirm the presence of iron on the graphene surface, X-ray photoelectron spectroscopy (XPS) was performed. This technique is commonly used to analyze the chemical composition of a sample and is based on the photoelectric effect. An incoming X-ray with sufficiently high energy can be absorbed by an atom leading to the ejection of an electron with a certain kinetic energy.

The XPS bases its principle on the conservation of incident photon energy, which can be expressed as follows:

$$h\nu = E_{kinetic} + E_{binding} + \phi \tag{89}$$

with $h\nu$, incident photon energy, $E_{kinetic}$ kinetic energy, $E_{binding}$, the binding energy and ϕ, the work function. The work function and the photon energy are known parameters. The work function of a material is the minimum energy required to remove an electron from a solid to a point in the vacuum. By measuring the kinetic energy of the ejected electrons, it is possible to determine the value of the binding energy. Indeed, this energy depends on the element and the orbit from which the electron is ejected [116].

Figure 73 is the result of the XPS measurements on the sample G_2 after deposition of nanoparticles with (a)/(b) and (c)/(d) are respectively obtained for a surface of analysis of $1.4mm^2$ and $250\mu m^2$. Figures (b) and (d) are the Fe_{2p} spectra from figures (a) and (c) respectively.

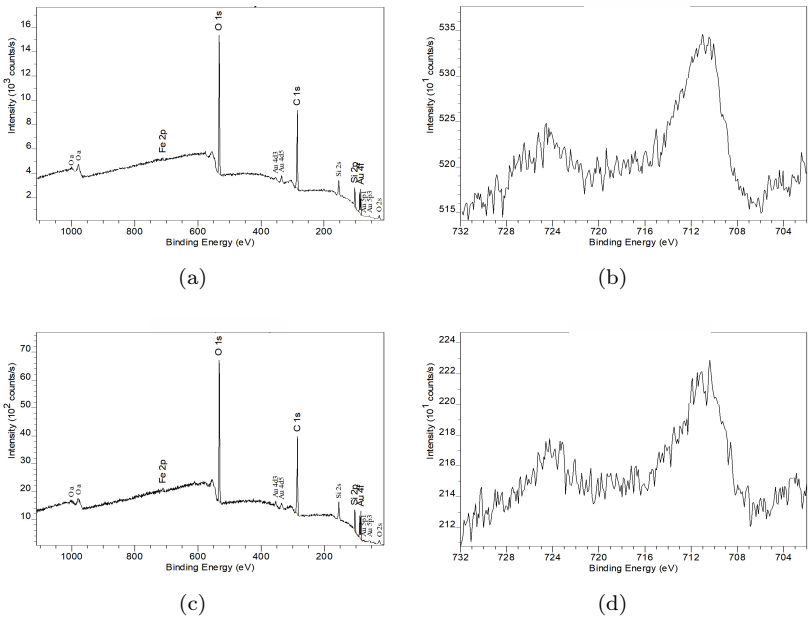

Figure 73: XPS results on the sample G_2.

With these figures, we can conclude that iron is present. Indeed, the position of the main peaks at $711.2eV$ and $710.6eV$ for figures 73(b) and (d) respectively, corresponds to iron with the atomic concentration of 0.4% for both cases. However, we have to take into account a possible presence of iron which comes from the etchant solution of copper during the wet transfer of the CVD graphene. To prove the presence of iron before the deposition, the XPS analysis has to be performed before the fuctionalization

Figure 74 gives the result of the electrical measurement realized on G_2 after the deposition of the nanoparticles and after putting the sample in vacuum at room temperature. The Dirac point is located at $6V$ compared to $12V$ before deposition. The mobility of the electrons and the holes are not affected by the presence of magnetite nanoparticles and are respectively $237cm^2/Vs$and $992cm^2/Vs$ compared to $145cm^2/Vs$ and $970cm^2/Vs$ before deposition.

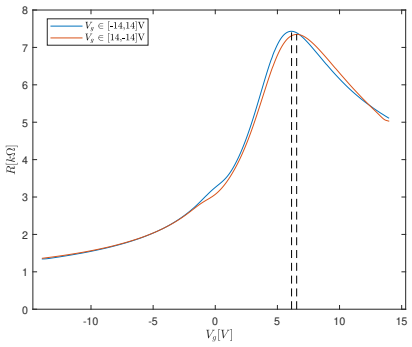

Figure 74: Measurement was realized on G_2. An alternative current of $20nA$ with a frequency of $413Hz$ flowed between the two contacts. The blue and red curves are respectively obtained by varying the back gate from -20 to $20V$ and from 20 to $-20V$.

An important parameter that can explain the shift of the Dirac point is the relative work function between the magnetite nanoparticle and the graphene.

The work function of graphene is $4.5eV$ [117]. A work function of $5.20eV$ for magnetite was obtained in Ref. [118]. Consequently, the graphene is n-doped due to the presence of the magnetite nanoparticles which can explain the shift of the Dirac point compared to the one obtained in figure 62(d).

Conclusion and perspectives

In the first part of this master thesis, the quantum anomalous Hall effect was highighted by using Kwant and Pybinding. Indeed, by adding the Rashba spin-orbit coupling and exchange in the tight-binding model of graphene, it was possible to show that it opened a topologically non-trivial band gap. Thus, by simulating a graphene nanoribbon, a Hall resistivity of $\frac{1}{2}\frac{h}{e^2}$ was obtained with a zero longitudinal resistivity in the bulk band gap. Moreover, as the main objective was to deposit magnetite nanoparticles, a system with a Rashba spin-orbit coupling and a non-uniform exchange field was implemented allowing to realize that the quantum anomalous Hall effect was still observable with a decrease of the band gap in the bulk graphene with a decrease of the density of the nanoparticles. However, these simulations did not take into account the presence of a weak magnetic field necessary to orient the magnetization directions of the nanoparticles. A combined classical hall effect and quantum anomalous hall effect should be experimentally observed. Moreover, these results were realized using Rashba spin-orbit coupling and exchange field strengths that did not represent physical reality. These simulations should therefore allow a qualitative analysis.

In the second part of this paper, the first experimental results were reported. The samples received by Graphenea were contaminated leading to a significant shift of the Dirac point. It was, therefore, necessary to clean them. Indeed, the purpose was to deposit nanoparticles and it was therefore important to limit the presence of other contaminants that could disrupt future measurements. For this purpose, different cleaning techniques and their effects were described. First of all, the samples were immersed in acetone for 24 hours. This step made it possible to reduce the position of the Dirac point. However, except for the sample G_2, the Dirac point was always at too high a value, meaning still a significant contamination. It was therefore decided to clean with the AFM in contact mode to push back the impurities. However, after the electrical measurement, all samples cleaned with AFM did not highlight the ambipolar electrical effect. To reduce the size of the Hall bar, firstly to facilitate cleaning by AFM allowing to push impurities out of the graphene and secondly to facilitate the enumeration of the deposited nanoparticles, we used a FIB with gallium-ions. However, this step created important defects in graphene. It was then decided to use the G_2 sample for the deposition of nanoparticles. This part stopped with the measurement of the Dirac point after deposition. The Dirac point of the sample G_2 shifted from $12V$ to $6V$. Moreover, the deposition of the nanoparticles did not seem to have decreased the quality of the graphene because the mobilities of the electrons and holes were of the same order of magnitude before and after deposition.

The different results obtained in this master thesis, open different future perspectives. First of all, it would be interesting to use the magnetic force microscope to visualize the presence of nanoparticles and their dispersions (unless their density is too high) easily. Then, the effect of changing the density of nanoparticles on the transport in graphene could be analyzed. Finally, measurements at low temperatures under a weak magnetic field would perhaps make it possible to highlight the anomalous Hall effect in graphene. However, as obtained in the Kwant simulations, the presence of a too high disorder, or a non-uniform Rashba spin-orbit coupling and exchange field can reduce the bulk band gap of graphene making it difficult to highlight this phenomenon. Moreover, the magnetite nanoparticles are composed of a core made of oxygen and iron surrounded by an organic shell, which avoids the agglomerations and short-circuits. The exchange field, due to the hybridisation between carbon π states of graphene and the localised d-states of iron atoms, and the Rashba spin-orbit coupling will be strongly reduced, leading to a smaller band gap.

10 Annex

10.1 Development of the secular equation

The two terms presented in equation 11 are:

$$H_k = \begin{pmatrix} \Psi^{(A)*}(\mathbf{r},\mathbf{k})H\Psi^{(A)}(\mathbf{r},\mathbf{k}) & \Psi^{(A)*}(\mathbf{r},\mathbf{k})H\Psi^{(B)}(\mathbf{r},\mathbf{k}) \\ \Psi^{(B)*}(\mathbf{r},\mathbf{k})H\Psi^{(A)}(\mathbf{r},\mathbf{k}) & \Psi^{(B)*}(\mathbf{r},\mathbf{k})H\Psi^{(B)}(\mathbf{r},\mathbf{k}) \end{pmatrix} \tag{90}$$

and

$$S_k = \begin{pmatrix} \Psi^{(A)*}(\mathbf{r},\mathbf{k})\Psi^{(A)}(\mathbf{r},\mathbf{k}) & \Psi^{(A)*}(\mathbf{r},\mathbf{k})\Psi^{(B)}(\mathbf{r},\mathbf{k}) \\ \Psi^{(B)*}(\mathbf{r},\mathbf{k})\Psi^{(A)}(\mathbf{r},\mathbf{k}) & \Psi^{(B)*}(\mathbf{r},\mathbf{k})\Psi^{(B)}(\mathbf{r},\mathbf{k}) \end{pmatrix} \tag{91}$$

The eigenvalues given by E from equation 11, are obtained by solving the secular equation:

$$det[H_k - ES_k] = 0 \tag{92}$$

Consequently, we should first calculate the different parts of the matrix H_k and S_k. Each terms of the matrix H_k are equal to :

$$\Psi^{(i)*}(\mathbf{r},\mathbf{k})\Delta U\Psi^{(j)}(\mathbf{r},\mathbf{k}) = \frac{1}{N}\sum_{\mathbf{R}_j}\sum_{\mathbf{R}_i} e^{i\mathbf{k}\cdot(\mathbf{R}_j-\mathbf{R}_i)}\int \phi^{(i)*}(\mathbf{r}+\boldsymbol{\delta}_i-\mathbf{R}_i)\Delta U_i\phi^{(i)}(\mathbf{r}+\boldsymbol{\delta}_j-\mathbf{R}_j)dr^2 \tag{93}$$

In the case of $i = j = A$ or B, as we consider only the interaction between the nearest-neighbors, $\mathbf{R}_1 = \mathbf{R}_2$. The diagonal terms of the matrix H_k vanish. On the other hand, if $i = A$ and $j = B$, or if $i = B$ and $j = A$, the terms do not vanish anymore and a hopping parameter can be defined:

$$t = \int \phi^{(A)*}(\mathbf{r}-\mathbf{R}_A)\Delta U\phi^{(B)}(\mathbf{r}+\boldsymbol{\delta}_B-\mathbf{R}_B)dr^2 = \int \phi^{(B)*}(\mathbf{r}+\boldsymbol{\delta}_B-\mathbf{R}_B)\Delta U\phi^{(A)}(\mathbf{r}-\mathbf{R}_A)dr^2 \tag{94}$$

which is a constant approximately equal to 2.7-3eV. Consequently,

$$\Psi^{(A)*}(\mathbf{r},\mathbf{k})H\Psi^{(B)}(\mathbf{r},\mathbf{k}) = t(1 + e^{-i\mathbf{k}\cdot\mathbf{a}_1} + e^{-i\mathbf{k}\cdot\mathbf{a}_2}) = tf^*(k) = [\Psi^{(B)*}(\mathbf{r},\mathbf{k})H\Psi^{(A)}(\mathbf{r},\mathbf{k})]^* \tag{95}$$

with

$$f(k) = 1 + e^{-i\mathbf{k}\cdot\mathbf{a}_1} + e^{-i\mathbf{k}\cdot\mathbf{a}_2} = \sqrt{1 + 4cos\frac{\sqrt{3}k_x a_{cc}}{2}cos\frac{k_y a_{cc}}{2} + 4cos^2\frac{k_y a_{cc}}{2}} \tag{96}$$

Each term of the matrix S_k are given by:

$$\Psi^{(i)*}(\mathbf{r},\mathbf{k})\Psi^{(j)}(\mathbf{r},\mathbf{k}) = \frac{1}{N}\sum_{\mathbf{R}_j}\sum_{\mathbf{R}_i} e^{i\mathbf{k}\cdot(\mathbf{R}_j-\mathbf{R}_i)}\int \phi^{(i)*}(\mathbf{r}+\boldsymbol{\delta}_i-\mathbf{R}_i)\phi^{(i)}(\mathbf{r}+\boldsymbol{\delta}_j-\mathbf{R}_j)dr^2 \tag{97}$$

In the case of i=j, the equation 97 is equal to 1. In the other hand, if i=A and j=B, the equation 97 is equal to zero if we consider no overlap. The equation 92 becomes:

$$det\begin{bmatrix} E & tf^*(k) \\ tf(k) & E \end{bmatrix} = E^2 - t^2f^2(k) = 0 \tag{98}$$

Consequently, the eigenvalues of the Hamiltonian are:

$$\boxed{E = \pm t\sqrt{1 + 4cos\frac{\sqrt{3}k_x a}{2}cos\frac{k_y a}{2} + 4cos^2\frac{k_y a}{2}}} \tag{99}$$

10.2 Berry phase: Time-dependant Schrodinger equation

The state given in equation 49 can be inserted into the time-dependant Schrodinger equation:

$$i\hbar\frac{d}{dt}e^{i\phi_i(t)}\left|\Psi_i(\boldsymbol{R})\right\rangle = H_f(\boldsymbol{R}[t/T])e^{i\phi_i(t)}\left|\Psi_i(\boldsymbol{R})\right\rangle \tag{100}$$

The second part of the equation is just $e^{i\phi_i(t)}\left|\Psi_i(\boldsymbol{R})\right\rangle$ $\mathrm{E}_i(\boldsymbol{R})$.
The simplification of the first one is described below:

$$\frac{d}{dt}e^{i\phi_i(t)}\left|\Psi_i(\boldsymbol{R})\right\rangle = i\frac{d\phi_i(t)}{dt}e^{i\phi_i(t)}\left|\Psi_i(\boldsymbol{R})\right\rangle + e^{i\phi_i(t)}\frac{d}{dt}\left|\Psi_i(\boldsymbol{R})\right\rangle \tag{101}$$

The derivative as a function of time of the eigenstate is given by :

$$\frac{d}{dt}\left|\Psi_i(\boldsymbol{R})\right\rangle = \frac{d}{dR_1}\left|\Psi_i(\boldsymbol{R})\right\rangle\frac{R_1}{dt} + \frac{d}{dR_2}\left|\Psi_i(\boldsymbol{R})\right\rangle\frac{dR_2}{dt} + ... = \Delta_{\boldsymbol{R}}\left|\Psi_i(\boldsymbol{R})\right\rangle\cdot\frac{d\boldsymbol{R}}{dt} \tag{102}$$

We can now introduce all the parameters in equation 100 and multiply by $e^{i\phi_i(t)} < \Psi_i(\boldsymbol{R})|$.
By isolating the phase $\phi_i(t)$, we obtain:

$$\frac{d\phi_i(t)}{dt} = i < \Psi_i(\boldsymbol{R})|\Delta_{\boldsymbol{R}}|\Psi_i(\boldsymbol{R}) > \cdot\frac{d\boldsymbol{R}}{dt} - \frac{1}{\hbar}E_i(\boldsymbol{R})]dx \tag{103}$$

Consequently:

$$\phi_i(t)-\phi_i(0) = \int_0^t dt'[i < \Psi_i(\boldsymbol{R})|\Delta_{\boldsymbol{R}}|\Psi_i(\boldsymbol{R}) > \cdot\frac{d\boldsymbol{R}}{dt} - \frac{1}{\hbar}E_i(\boldsymbol{R})] = \int_{\boldsymbol{R}[0]}^{\boldsymbol{R}[t]} < \Psi_i(\boldsymbol{R})|i\Delta_{\boldsymbol{R}}|\Psi_i(\boldsymbol{R}) > \boldsymbol{R} - \frac{1}{\hbar}\int_0^t dt' E_i(\boldsymbol{R}) \tag{104}$$

10.3 Kwant: A python package for quantum transport simulations

Kwant is a free and user-friendly python package used for quantum transport caluclations. It can simulate any system of any size that can be described with tight binding models and allows to solve the scattering problem of particles in a system coupled to semi-infinite leads. Transport properties as the conductance, the density of state or the density of current can be obtained.

To describe how an Hamiltonian is implemented in Kwant, consider a continuous Hamiltonian of a 2-dimensional square system as the one presented in the first tutorial in the Kwant website:

$$H = -\frac{\hbar^2}{2m}(\delta_x^2 + \delta_y^2) + V(x,y) \tag{105}$$

with m, the effective mass and $V(x,y)$, the local potential energy. This continuous Hamiltonian can only be implemented in Kwant if it is discritised into a tight binding model. Each site of the square lattice corresponds to an integer with a lattice coordinate (i,j). This coordinate is linked to the real coordinate by $(x,y) = (ai, aj)$ with a the lattice parameter of the square lattice. A discretised positional state can be defined as:

$$|i,j\rangle = |ai, aj\rangle = |x,y\rangle \tag{106}$$

Consequently,

$$\delta_x^2 = \frac{1}{a^2}\sum_{i,j}(|i+1,j\rangle\langle i,j| + |i,j\rangle\langle i+1,j| - 2\,|i,j\rangle\langle i,j|) \tag{107}$$

An equivalent expression can be obtained for δ_y^2. The Hamiltonian becomes:

$$H = \sum_{i,j}[(V(ai,aj)+4t)\,|i,j\rangle\langle i,j| - t(|i+1,j\rangle\langle i,j| + |i,j\rangle\langle i+1,j| + |i,j+1\rangle\langle i,j| + |i,j\rangle\langle i,j+1|)] \tag{108}$$

t is the nearest-neighbor hopping and is defined by $\frac{\hbar^2}{2ma^2}$. It is important to note that this model is only valid if all the quantum states have a wavelength larger that the lattice paramater. In other words, the model is valid if $\lambda_F >> a$.

10.4 Code Kwant

10.4.1 Exchange Field

```
def onsite(site_i,V_R=0.1*(-t),m=0.3*(-t)):
    return m*sigma_z
```

Figure 75: Implementation of the exchange field in code using Kwant package with t, the hopping parameter, m, the exchange field parameter and $\boldsymbol{\sigma}_z$, the Pauli matrice.

10.4.2 Rashba Spin orbit Coupling

```
def rashba(site_i,site_j,V_R=0.1*(-t),m=0.3*(-t)):

    d_ij1 = site_i.pos-site_j.pos

    d_ij=d_ij1/(np.sqrt(d_ij1[0]**2+d_ij1[1]**2))#Unitary Vector

    rashbal = 1j * V_R* (sigma_x * d_ij[1] - sigma_y * d_ij[0])

    return -t*sigma_0+rashbal
```

Figure 76: Implementation of the Rashba spin-orbit coupling in code using Kwant package with t, the hopping parameter, V_R, the RSOC parameter and d_{ij}, the unit vector between two atoms and $\boldsymbol{\sigma}$, the Pauli matrices.

10.4.3 System implementation

```
def systemeComplet(W=1000e-9,L=1000e-9,boolean=True):
    syst1 = kwant.Builder()
    lat1 = kwant.lattice.general([(np.sqrt(3)*a, 0), (0, 3*a)], [(a*np.sqrt(3)/2, 0), (0, a/2), (0, 3*a/2)\
                                                                 , (a*np.sqrt(3)/2, 2*a)],norbs=2)
    A, B, C, D = lat1.sublattices

    hoppings = (((0, 0), B, A), ((0, 0), C, B), ((0, 0), D, C), ((-1, 0), A, B), ((-1, 0), D, C),\
                ((0, 1), A, D))

    syst1[lat1.shape(geom,(0,0))]=onsite
    syst1[[kwant.builder.HoppingKind(*hopping) for hopping in hoppings]] = rashba


    sym0 = kwant.TranslationalSymmetry(lat1.vec((-1, 0)))
    lead0 = kwant.Builder(sym0)
    lead0[lat1.shape(lead_shape,(0,0))]=onsite
    lead0[[kwant.builder.HoppingKind(*hopping) for hopping in hoppings]] = rashba


    sym1 = kwant.TranslationalSymmetry(lat1.vec((1, 0)))
    lead1 = kwant.Builder(sym1)
    lead1[lat1.shape(lead_shape,(0,0))]=onsite
    lead1[[kwant.builder.HoppingKind(*hopping) for hopping in hoppings]] = rashba

    sym3 = kwant.TranslationalSymmetry(lat1.vec((0, 1)))
    lead3 = kwant.Builder(sym3)
    lead3[lat1.shape( VertiLead1,(-posL,0))]=onsite
    lead3[[kwant.builder.HoppingKind(*hopping) for hopping in hoppings]] = rashba

    sym5 = kwant.TranslationalSymmetry(lat1.vec((0, 1)))
    lead5 = kwant.Builder(sym3)
    lead5[lat1.shape( VertiLead2,(posL,0))]=onsite
    lead5[[kwant.builder.HoppingKind(*hopping) for hopping in hoppings]] = rashba

    syst1.attach_lead(lead0)
    syst1.attach_lead(lead1)

    syst1=syst1.finalized()

    return syst1
```

Figure 77: Example of implementation of the system including the Rashba spin-orbit coupling and the exchange field.

10.5 Density functional theory (DFT)

10.5.1 Fundamental principle

The purpose of the DFT is to solve the time-independant, non-relativistic Schrödinger equation of a system with M nuclei and N electrons:

$$H\Psi(\{\boldsymbol{r}_i\},\{\boldsymbol{R}_e\}) = E\Psi_i(\{\boldsymbol{r}_i\},\{\boldsymbol{R}_e\}) \tag{109}$$

with r_i the parameters linked to the electrons and R_e linked to the nucleus. $H$is the Hamiltonian and is equal to the sum of two operators: T and $V_{coulomb}$. The first one is the kinetic energy of the electrons and nuclei. The second one is the Coulomb potential due to the interactions between electrons, between nucleus and between electrons and nucleus. This equation is difficult to solve without doing some approximations.

The first approximation is called the "Born-Oppenheimer approximation". Nuclei are much heavier and slower than electrons. Consequently, the wavefunction can be decoupled into a electronic and a nuclear part:

$$\Psi(\{\boldsymbol{r}_i\},\{\boldsymbol{R}_e\}) = \Psi_n(\{\boldsymbol{R}_e\})\star\Psi_e(\{\boldsymbol{r}_i\}) \tag{110}$$

Now, only the ground state of electrons can be obtained by solving the following equation:

$$H_e\Psi_e(\{\boldsymbol{r}_i\}) = E\Psi_e(\{\boldsymbol{r}_i\}) \tag{111}$$

The electronic Hamiltonian is composed of three terms:

$$H_e = -\frac{\hbar}{2m_e}\sum_i^{N_e}\nabla_i^2 - \sum_i^{N_e}V_{ext} + \sum_{i=1}^{N_e}\sum_{j>i}^{N_e}U(\boldsymbol{r}_i,\boldsymbol{r}_j) \tag{112}$$

with the first term, the kinetic energy, the second one, the potential due to the interaction between electron and nucleus and the last one the electron-electron repulsion.

The DFT is based on two important theorems:

- The ground state energy E is a unique functional(=function of a function) of the electron density:

  $$E = E[n(\boldsymbol{r})] \tag{113}$$

  with $n(\boldsymbol{r})$ the electron density given by :

  $$n(\boldsymbol{r}) = \Psi_e(\{\boldsymbol{r}_i\})^*\Psi_e(\{\boldsymbol{r}_i\}) \tag{114}$$

- The electron density that minimizes the energy of the overal functional is the ground state electron density:

  $$E[n(\boldsymbol{r})] > E[n_o(\boldsymbol{r})] \tag{115}$$

This energy can be divided into two parts:

$$E[\{\Psi_i\}] = E_{cl} + E_{XC} \tag{116}$$

The first part is known and is given by:

$$E_{cl} = \frac{-\hbar}{m_e}\sum_i^{N_e}\Psi_i(\{\boldsymbol{r}_i\})^*\nabla^2\Psi_i(\{\boldsymbol{r}_i\}) + \int V(\boldsymbol{r})n(\boldsymbol{r})d^3\boldsymbol{r} + \frac{e^2}{2}\int\int\frac{n(\boldsymbol{r})n(\boldsymbol{r'})}{\boldsymbol{r}-\boldsymbol{r'}}d^3\boldsymbol{r}d^3\boldsymbol{r'} + E_{ion} \tag{117}$$

The first one is the kinetic energy, the second one is due to the interaction between nucleus and electrons, the third one is due to electron-electron interactions and is also called the Hartree energy and the last one is the nuclei-nuclei interaction. The second term of the equation 116 is called the exchange correlation functional. It takes into account all the quantum mechanical interactions between electrons. Unfortunately, this terms is unknown and needs to be approximated. The two simplest exchange correlation functionals are:

- Local density approximation(LDA): Consider that the exchange correlation potential depends only on the electron density
- Generalized gradiant approximation(GGA): Consider that the exchange correlation potential depends also on the gradient of the electron density

To simplify the problem, Kohn and Sham found a way to obtain practically the ground state electron density. They solve a set of single-electron wavefunctions that do not interact:

$$[-\frac{\hbar^2}{2m_e}\nabla^2 + V(\boldsymbol{r}) + V_H(\boldsymbol{r}) + V_{XC}(\boldsymbol{r})]\Psi_i\boldsymbol{r} = \epsilon_i\Psi_i\boldsymbol{r} \tag{118}$$

They used a self-consistency principle divided into 3 steps:

- Choosing some electron density
- Introducing into the Kohn and Shame equation and solving all the equations (one per electron) to determine the wavefunctions
- Determining the electron density.

If the new electron density is the same as the initial one, it means that we are in the ground state. If it is not the case, we need to repeat the last two steps.

10.5.2 Important numerical parameters

An import concept in DFT calculation is called the cutoff energy. Electrons in a periodic potential induced by a periodic arrangement of atoms(a crystal) are represented by Bloch waves:

$$|\Psi_{j\boldsymbol{k}}(\mathbf{r})\rangle = e^{i\mathbf{k}\cdot\mathbf{r}}\,|u_{j\boldsymbol{k}}(\mathbf{r})\rangle \tag{119}$$

with u_j, a function that possesses the periodicity of the potential, j, the energy band index and **k** the wavevector in the first Brillouin zone. One can define a reciprocal lattice vector, **G**, which links two equivalent wavevectors from different unit cells of the crystal. In other words, **k** and **k'** in the following equation are considered equivalent if:

$$\mathbf{k} = \mathbf{k'} + m\mathbf{G} \tag{120}$$

with m, an integer. As $u_{j\boldsymbol{k}}$ is periodic, it can be represented by Fourier series:

$$e^{i\mathbf{k}\cdot\mathbf{r}}\,|u_{j\boldsymbol{k}}(\mathbf{r})\rangle = e^{i\mathbf{k}\cdot\mathbf{r}}\sum_{\boldsymbol{G}} c_{\boldsymbol{k}}e^{i\boldsymbol{G}\cdot\boldsymbol{r}} \tag{121}$$

Consequently, the Bloch waves can be represented as an infinite sum of plane-waves $e^{i(\boldsymbol{G}+\boldsymbol{k})\cdot\boldsymbol{r}}$. Each plane wave has a kinetic energy given by:

$$E = \frac{\hbar^2}{2m}[\boldsymbol{k}+\boldsymbol{G}]^2 \tag{122}$$

However, in numerical calculations, it is impossible to manage a infinite sum. A so-called cutoff energy needs to be defined. Plane waves with an energy higher than the cutoff energy will not be considered. To determine this value, convergence study in function of the total energy of the system must be realised.

Another import concept is the number of k-points used in the first Brillouin zone. Indeed, numerically, we need to choose a finite number of k-points to sample the Brillouin zone. Again, to determine this number, a convergence strudy in function of the total energy must be realised.

10.6 Convergence study

In this section, the different results of the convergence study will be shown. Firstly, the convergence study in the graphene unit cell will be developed. Finally, the convergence study for the iron face-centered-cubic structure will be given.

10.6.1 Graphene Unit Cell

10.6.1.1 Cutoff energy

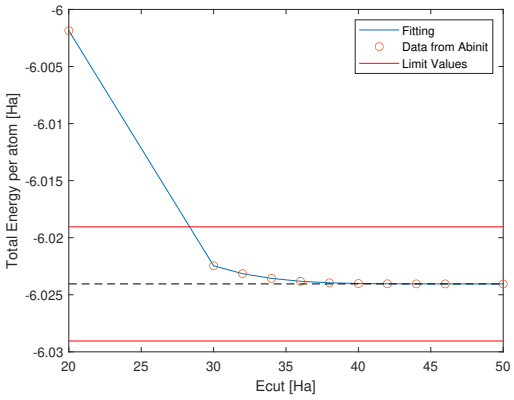

Figure 78: Convergence study of the cut-off energy for the unit cell of graphene with the grid of k-points (5x5x1) with a numerical accuracy better than 0.5 mHa/atom for the total energy.

10.6.1.2 Number of k-points

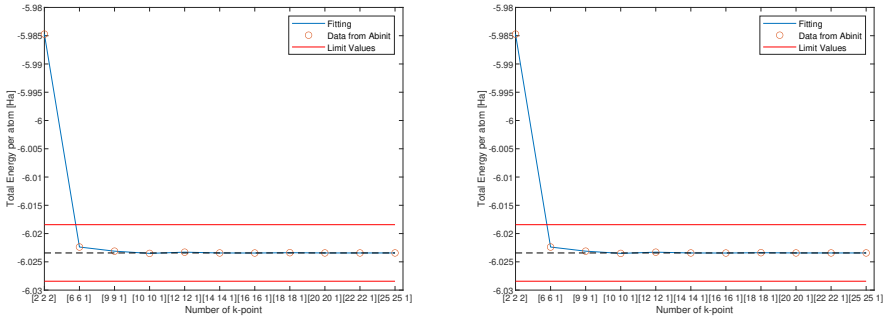

(a) (b)

Figure 79: Convergence study of the number of k-points as a function of the total energy per atom in the unit cell of graphene with a temperature of smearing equal to (a)0.004eV, (b) 0.005eV with an energy cut-off of 35 Ha and a numerical accuracy better than $0.5 mHa/atom$ for the total energy.

10.6.1.3 Lattice parameter Acell(1) and Acell(2)

10.6.1.4 Acell(3)

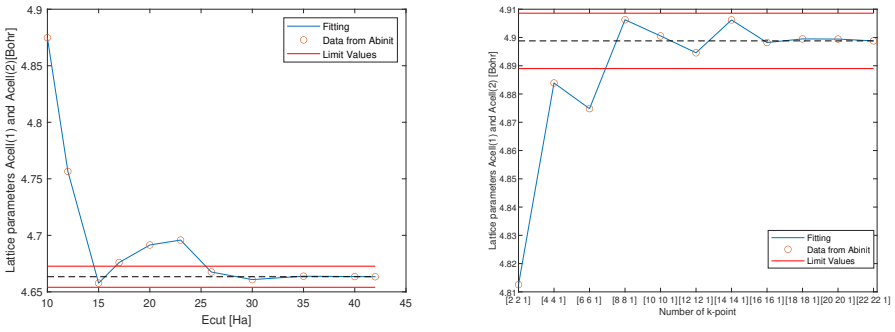

(a) (b)

Figure 80: Convergence study of the lattice parameters acell(1) and acell(2) in function of the (a) cut-off energy (b) grid of k-points numerical accuracy better than 0.2%.

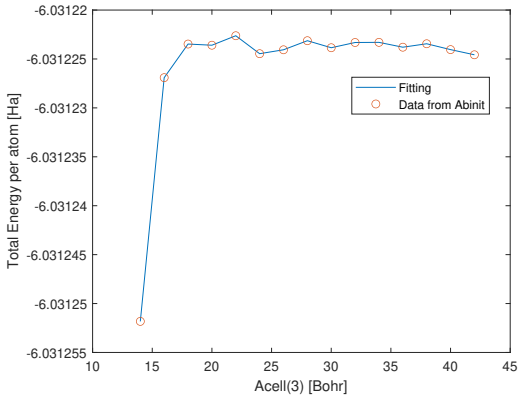

Figure 81: Convergence study of the lattice constant acell(3) in function of the total energy per atom with the energy cut-off equal to 35Ha.

10.6.2 Iron face-centered-cubic structure

10.6.2.1 Acell(1) and Acell(2)

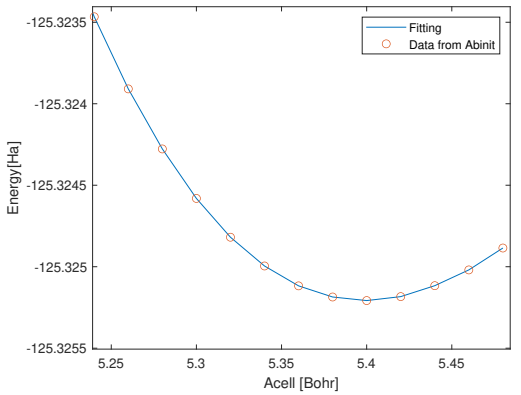

Figure 82: Convergence study of the lattice parameters acell(1), acell(2) and acell(3) in function of the total energy with a cut-off energy of 45 Ha.

10.6.2.2 Ecut in function of the total magnetization

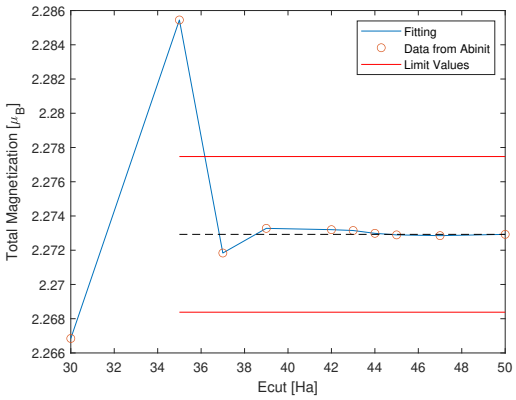

Figure 83: Convergence study of ecut in function of the total magnetisation.

10.7 Raman sprectra: Raw Data

In this section, the raw data obtained by Raman spectroscopy will be presented. To determine the baseline of each set of data, the model presented in Ref. [119] was used.

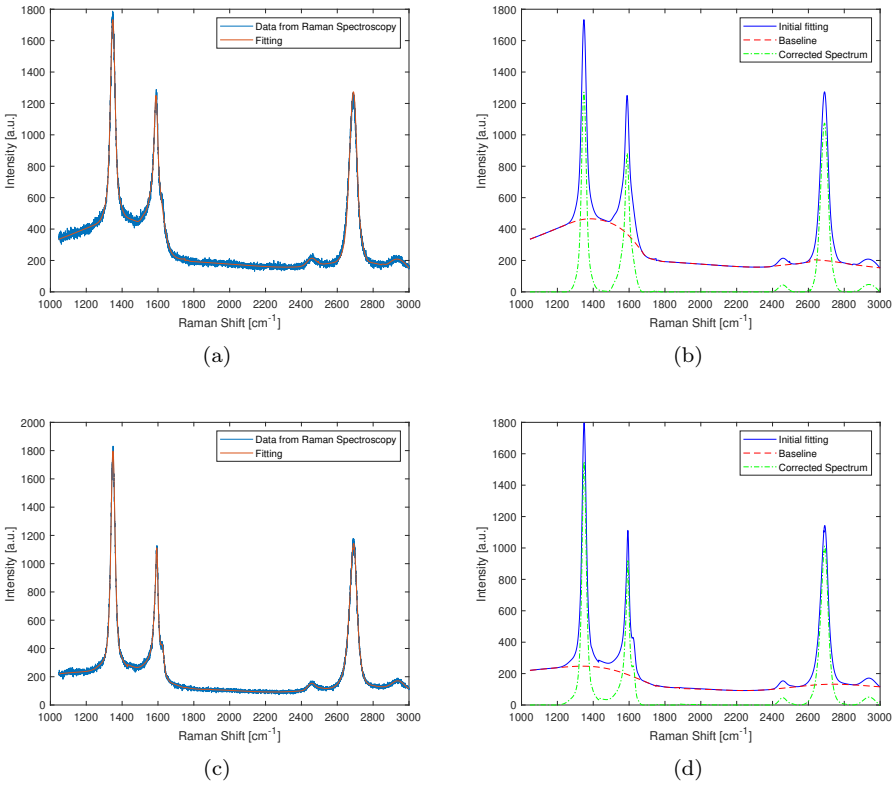

Figure 84: Treatment of the data obtained by Raman spectroscopy for(a) and (b) G_4 and (c) and (d) G_5.

References

[1] K. S. Novoselov et al. "Electric Field Effect in Atomically Thin Carbon Films". In: *Science* 306.5696 (2004), pp. 666–669. DOI: 10.1126/science.1102896.

[2] F. D. M. Haldane. "Model for a Quantum Hall Effect without Landau Levels: Condensed-Matter Realization of the "Parity Anomaly"". In: *Phys. Rev. Lett.* 61 (18 Oct. 1988), pp. 2015–2018. DOI: 10.1103/PhysRevLett.61.2015. URL: https://link.aps.org/doi/10.1103/PhysRevLett.61.2015.

[3] C. L. Kane and E. J. Mele. "Quantum Spin Hall Effect in Graphene". In: *Phys. Rev. Lett.* 95 (22 Nov. 2005), p. 226801. DOI: 10.1103/PhysRevLett.95.226801. URL: https://link.aps.org/doi/10.1103/PhysRevLett.95.226801.

[4] Jiayong Zhang et al. "Quantum Anomalous Hall Effect in Graphene-based Heterostructure". In: *Scientific Reports* 5 (May 2015), p. 10629. DOI: 10.1038/srep10629.

[5] N.M.R. Peres A.H. Castro Neto F. Guinea. "The electronic properties of graphene". In: *Review of Modern Physics* 81 (Jan. 2009). DOI: 10.1103/RevModPhys.81.109.

[6] M.O. Goerbig. "Electronic properties of graphene in a strong magnetic field". In: *Review of Modern Physics* 83 (Nov. 2011). DOI: 10.1103/RevModPhys.83.1193.

[7] Simon Dubois et al. "Electronic properties and quantum transport in Graphene-based nanostructures". In: *The European Physical Journal B* 72 (Nov. 2009), pp. 1–24. DOI: 10.1140/epjb/e2009-00327-8.

[8] Thomas Ihn. *Semiconductor nanostructures*. 1st ed. Oxfort University Press, 2010.

[9] J.-C. Charlier L. E. F. Foa Torres S. Roche. *Semiconductor nanostructures*. Cambridge University Press, 2014.

[10] Gordon W. Semenoff. "Condensed-Matter Simulation of a Three-Dimensional Anomaly". In: *Physical Review Letters* 53 (Dec. 1984). DOI:10.1103/PhysRevLett.53.2449.

[11] Seng Ghee Tan and Mansoor B.A. Jalil. *6 - Graphene carbon nanostructures for nanoelectronics*. Ed. by Seng Ghee Tan and Mansoor B.A. Jalil. Woodhead Publishing Series in Electronic and Optical Materials. Woodhead Publishing, 2012, pp. 198–242. ISBN: 978-0-85709-511-4. DOI: https://doi.org/10.1533/9780857095886.198. URL: http://www.sciencedirect.com/science/article/pii/B978085709511450006X.

[12] A. F. Morpurgo and F. Guinea. "Intervalley Scattering, Long-Range Disorder, and Effective Time-Reversal Symmetry Breaking in Graphene". In: *Phys. Rev. Lett.* 97 (19 Nov. 2006), p. 196804. DOI: 10.1103/PhysRevLett.97.196804. URL: https://link.aps.org/doi/10.1103/PhysRevLett.97.196804.

[13] F. V. Tikhonenko et al. "Transition between Electron Localization and Antilocalization in Graphene". In: *Phys. Rev. Lett.* 103 (22 Nov. 2009), p. 226801. DOI: 10.1103/PhysRevLett.103.226801. URL: https://link.aps.org/doi/10.1103/PhysRevLett.103.226801.

[14] Mikhail Katsnelson, K. Novoselov, and A. Geim. "Chiral tunneling and the Klein paradox in graphene". In: *Nature Physics* 2 (Sept. 2006), pp. 620–625. DOI: 10.1038/nphys384.

[15] Seunghyun Lee and Zhaohui Zhong. "Nanoelectronic circuits based on two-dimensional atomic layer crystals". In: *Nanoscale* 6 (Sept. 2014). DOI: 10.1039/C4NR03670K.

[16] M.F. Craciun et al. "Tuneable electronic properties in graphene". In: *Nano Today* 6.1 (2011), pp. 42–60. ISSN: 1748-0132. DOI: https://doi.org/10.1016/j.nantod.2010.12.001. URL: http://www.sciencedirect.com/science/article/pii/S1748013210001623.

[17] Mitsutaka Fujita, Katsunori Wakabayashi, and Nakada. "Peculiar Localized State at Zigzag Graphite Edge". In: *Journal of the Physical Society of Japan* 65.7 (1996), pp. 1920–1923. DOI: 10.1143/JPSJ.65.1920. eprint: https://doi.org/10.1143/JPSJ.65.1920. URL: https://doi.org/10.1143/JPSJ.65.1920.

[18] Katsunori Wakabayashi et al. "Electronic states of graphene nanoribbons and analytical solutions". In: *Science and Technology of Advanced Materials* 11.5 (2010). PMID: 27877361, p. 054504. DOI: 10.1088/1468-6996/11/5/054504. eprint: https://doi.org/10.1088/1468-6996/11/5/054504. URL: https://doi.org/10.1088/1468-6996/11/5/054504.

[19] John H. Davies. *The Physics of Low-dimensional Semiconductors: An Introduction*. Cambridge University Press, 1997. DOI: 10.1017/CBO9780511819070.

[20] K. v. Klitzing, G. Dorda, and M. Pepper. "New Method for High-Accuracy Determination of the Fine-Structure Constant Based on Quantized Hall Resistance". In: *Phys. Rev. Lett.* 45 (6 Aug. 1980), pp. 494–497. DOI: 10.1103/PhysRevLett.45.494. URL: https://link.aps.org/doi/10.1103/PhysRevLett.45.494.

[21] Daniel Cooper et al. "Experimental Review of Graphene". In: *ISRN Condens. Matter Phys.* 2012 (Oct. 2011). DOI: 10.5402/2012/501686.

[22] Wilfrid Poirier et al. "The ampere and the electrical units in the quantum era". In: *Comptes Rendus Physique* 20 (May 2019), p. 92. DOI: 10.1016/j.crhy.2019.02.003.

[23] K. Novoselov et al. "Two-Dimensional Gas of Massless Dirac Fermions in Graphene". In: *Nature* 438 (Dec. 2005), pp. 197–200. DOI: 10.1038/nature04233.

[24] F. Duncan M. Haldane. "Nobel Lecture: Topological quantum matter". In: *Rev. Mod. Phys.* 89 (4 Oct. 2017), p. 040502. DOI: 10.1103/RevModPhys.89.040502. URL: https://link.aps.org/doi/10.1103/RevModPhys.89.040502.

[25] Chao-Xing Liu, Shou-Cheng Zhang, and Xiao-Liang Qi. "The Quantum Anomalous Hall Effect: Theory and Experiment". In: *Annual Review of Condensed Matter Physics* 7.1 (2016), pp. 301–321. DOI: 10.1146/annurev-conmatphys-031115-011417. eprint: https://doi.org/10.1146/annurev-conmatphys-031115-011417. URL: https://doi.org/10.1146/annurev-conmatphys-031115-011417.

[26] M. Z. Hasan and C. L. Kane. "Colloquium: Topological insulators". In: *Rev. Mod. Phys.* 82 (4 Nov. 2010), pp. 3045–3067. DOI: 10.1103/RevModPhys.82.3045. URL: https://link.aps.org/doi/10.1103/RevModPhys.82.3045.

[27] Yafei Ren, Zhenhua Qiao, and Qian Niu. "Topological phases in two-dimensional materials: a review". In: *Reports on Progress in Physics* 79.6 (May 2016), p. 066501. DOI: 10.1088/0034-4885/79/6/066501. URL: https://doi.org/10.1088%2F0034-4885%2F79%2F6%2F066501.

[28] Markus König et al. "Quantum Spin Hall Insulator State in HgTe Quantum Wells". In: *Science (New York, N.Y.)* 318 (Dec. 2007), pp. 766–70. DOI: 10.1126/science.1148047.

[29] Sanfeng Wu et al. "Observation of the Quantum Spin Hall Effect up to 100 Kelvin in a Monolayer Crystal". In: *Science (New York, N.Y.)* 359 (Nov. 2017). DOI: 10.1126/science.aan6003.

[30] Marius Grundmann. *External Fields*. Cham: Springer International Publishing, 2016, pp. 437–460. ISBN: 978-3-319-23880-7. DOI: 10.1007/978-3-319-23880-7_13. URL: https://doi.org/10.1007/978-3-319-23880-7_13.

[31] S. A. Hassani Gangaraj, M. G. Silveirinha, and G. W. Hanson. "Berry Phase, Berry Connection, and Chern Number for a Continuum Bianisotropic Material From a Classical Electromagnetics Perspective". In: *IEEE Journal on Multiscale and Multiphysics Computational Techniques* 2 (2017), pp. 3–17.

[32] M. V. Berry. "Quantal Phase Factors Accompanying Adiabatic Changes". In: *Proceedings of the Royal Society of London. Series A, Mathematical and Physical Sciences* 392.1802 (1984), pp. 45–57. ISSN: 00804630. URL: http://www.jstor.org/stable/2397741.

[33] George Hanson, Ali Hassani Gangaraj, and Andrei Nemilentsau. "Notes on photonic topological insulators and scattering-protected edge states - a brief introduction". In: *arXiv:1602.02425v2* (May 2016).

[34] T. Thonhauser and David Vanderbilt. "Insulator/Chern-insulator transition in the Haldane model". In: *Phys. Rev. B* 74 (23 Dec. 2006), p. 235111. DOI: 10.1103/PhysRevB.74.235111. URL: https://link.aps.org/doi/10.1103/PhysRevB.74.235111.

[35] Michel Fruchart and David Carpentier. "An introduction to topological insulators". In: *Comptes Rendus Physique* 14.9 (2013). Topological insulators / Isolants topologiques, pp. 779–815. ISSN: 1631-0705. DOI: https://doi.org/10.1016/j.crhy.2013.09.013. URL: http://www.sciencedirect.com/science/article/pii/S1631070513001461.

[36] Marmi S. Golin S. Knauf A. "The Hannay angles: Geometry, adiabaticity, and an example." In: *Commun.Math. Phys.* 123 (1989), pp. 95–122. DOI: 10.1007/BF01244019.

[37] Eliahu Cohen et al. "Geometric phase from Aharonov–Bohm to Pancharatnam–Berry and beyond". In: *Nature Reviews Physics* (June 2019), p. 1. DOI: 10.1038/s42254-019-0071-1.

[38] Matthias Tarnowski et al. "Measuring topology from dynamics by obtaining the Chern number from a linking number". In: *Nature communications* 10.1 (Apr. 2019), p. 1728. ISSN: 2041-1723. DOI: 10.1038/s41467-019-09668-y. URL: https://europepmc.org/articles/PMC6465319.

[39] Robert Karplus and J. M. Luttinger. "Hall Effect in Ferromagnetics". In: *Phys. Rev.* 95 (5 Sept. 1954), pp. 1154–1160. DOI: 10.1103/PhysRev.95.1154. URL: https://link.aps.org/doi/10.1103/PhysRev.95.1154.

[40] Di Xiao, Ming-Che Chang, and Qian Niu. "Berry phase effects on electronic properties". In: *Rev. Mod. Phys.* 82 (3 July 2010), pp. 1959–2007. DOI: 10.1103/RevModPhys.82.1959. URL: https://link.aps.org/doi/10.1103/RevModPhys.82.1959.

[41] Cui-Zu Chang and Mingda Li. "Quantum Anomalous Hall Effect in Time-Reversal-Symmetry Breaking Topological Insulators". In: *Journal of Physics: Condensed Matter* 28 (Oct. 2015). DOI: 10.1088/0953-8984/28/12/123002.

[42] Xue-Si Li, Shu-Feng Zhang, and Wei-Jiang Gong. "Andreev reflections modulated by the breaking of space-inversion symmetry in graphene-typed materials". In: *New Journal of Physics* 21.8 (Aug. 2019), p. 083017. DOI: 10.1088/1367-2630/ab3562. URL: https://doi.org/10.1088%2F1367-2630%2Fab3562.

[43] Darshana Wickramaratne, Leigh Weston, and Chris Van de Walle. "Monolayer to Bulk Properties of Hexagonal Boron Nitride". In: *The Journal of Physical Chemistry C* 122 (Oct. 2018). DOI: 10.1021/acs.jpcc.8b09087.

[44] Dean Moldovan, Miša Anđelković, and Francois Peeters. *pybinding v0.9.4: a Python package for tight- binding calculations*. This work was supported by the Flemish Science Foundation (FWO-Vl) and the Methusalem Funding of the Flemish Government. July 2017. DOI: 10.5281/zenodo.826942. URL: https://doi.org/10.5281/zenodo.826942.

[45] Gregor Jotzu et al. "Experimental realization of the topological Haldane model with ultracold fermions". In: *Nature* 515 (Nov. 2014), pp. 237–40. DOI: 10.1038/nature13915.

[46] K. S. Novoselov et al. "Electric Field Effect in Atomically Thin Carbon Films". In: *Science* 306.5696 (2004), pp. 666–669. ISSN: 0036-8075. DOI: 10.1126/science.1102896. eprint: https://science.sciencemag.org/content/306/5696/666.full.pdf. URL: https://science.sciencemag.org/content/306/5696/666.

[47] M. Gmitra et al. "Band-structure topologies of graphene: Spin-orbit coupling effects from first principles". In: *Phys. Rev. B* 80 (23 Dec. 2009), p. 235431. DOI: 10.1103/PhysRevB.80.235431. URL: https://link.aps.org/doi/10.1103/PhysRevB.80.235431.

[48] J. Sichau et al. "Resonance Microwave Measurements of an Intrinsic Spin-Orbit Coupling Gap in Graphene: A Possible Indication of a Topological State". In: *Phys. Rev. Lett.* 122 (4 Feb. 2019), p. 046403. DOI: 10.1103/PhysRevLett.122.046403. URL: https://link.aps.org/doi/10.1103/PhysRevLett.122.046403.

[49] Zhenhua Qiao et al. "Quantum anomalous Hall effect in graphene from Rashba and exchange effects". In: *Phys. Rev. B* 82 (16 Oct. 2010), p. 161414. DOI: 10.1103/PhysRevB.82.161414. URL: https://link.aps.org/doi/10.1103/PhysRevB.82.161414.

[50] Petra Högl et al. "Quantum Anomalous Hall Effects in Graphene from Proximity-Induced Uniform and Staggered Spin-Orbit and Exchange Coupling". In: *Phys. Rev. Lett.* 124 (13 Mar. 2020), p. 136403. DOI: 10.1103/PhysRevLett.124.136403. URL: https://link.aps.org/doi/10.1103/PhysRevLett.124.136403.

[51] Lin'an Yang et al. "Asymmetric quantum-well structures for AlGaN/GaN/AlGaN resonant tunneling diodes". In: *Journal of Applied Physics* 119.16 (2016), p. 164501. DOI: 10.1063/1.4948331. eprint: https://doi.org/10.1063/1.4948331. URL: https://doi.org/10.1063/1.4948331.

[52] J. P. Heida et al. "Spin-orbit interaction in a two-dimensional electron gas in a InAs/AlSb quantum well with gate-controlled electron density". In: *Phys. Rev. B* 57 (19 May 1998), pp. 11911–11914. DOI: 10.1103/PhysRevB.57.11911. URL: https://link.aps.org/doi/10.1103/PhysRevB.57.11911.

[53] Takaaki Koga et al. "Rashba Spin-Orbit Coupling Probed by the Weak Antilocalization Analysis in InAlAs/InGaAs/InAlAs Quantum Wells as a Function of Quantum Well Asymmetry". In: *Phys. Rev. Lett.* 89 (4 July 2002), p. 046801. DOI: 10.1103/PhysRevLett.89.046801. URL: https://link.aps.org/doi/10.1103/PhysRevLett.89.046801.

[54] Anjan Soumyanarayanan et al. "Emergent Phenomena Induced by Spin-Orbit Coupling at Surfaces and Interfaces". In: *Nature* 539 (Nov. 2016), pp. 509–517. DOI: 10.1038/nature19820.

[55] Chien-Liang Chen, Yu-Hsin Su, and Ching-Ray Chang. "Spin-orbit force in graphene with Rashba spin-orbit coupling". In: *Journal of Applied Physics* 111.7 (2012), 07B330. DOI: 10.1063/1.3678488. eprint: https://doi.org/10.1063/1.3678488. URL: https://doi.org/10.1063/1.3678488.

[56] Conan Weeks et al. "Engineering a Robust Quantum Spin Hall State in Graphene via Adatom Deposition". In: *Phys. Rev. X* 1 (2 Oct. 2011), p. 021001. DOI: 10.1103/PhysRevX.1.021001. URL: https://link.aps.org/doi/10.1103/PhysRevX.1.021001.

[57] D. Marchenko et al. "Giant Rashba splitting in graphene due to hybridization with gold". In: *Nature Communications* 3 (Nov. 2012), p. 1232. DOI: 10.1038/ncomms2227.

[58] Zhenhua Qiao et al. "Microscopic theory of quantum anomalous Hall effect in graphene". In: *Phys. Rev. B* 85 (11 Mar. 2012), p. 115439. DOI: 10.1103/PhysRevB.85.115439. URL: https://link.aps.org/doi/10.1103/PhysRevB.85.115439.

[59] Mayra Peralta, Ernesto Medina, and Francisco Mireles. "Proximity-induced exchange and spin-orbit effects in graphene on Ni and Co". In: *Phys. Rev. B* 99 (19 May 2019), p. 195452. DOI: 10.1103/PhysRevB.99.195452. URL: https://link.aps.org/doi/10.1103/PhysRevB.99.195452.

[60] Sergej Konschuh, Martin Gmitra, and Jaroslav Fabian. "Tight-binding theory of the spin-orbit coupling in graphene". In: *Phys. Rev. B* 82 (24 Dec. 2010), p. 245412. DOI: 10.1103/PhysRevB.82.245412. URL: https://link.aps.org/doi/10.1103/PhysRevB.82.245412.

[61] Zhenhua Qiao et al. "Quantum Anomalous Hall Effect in Graphene Proximity Coupled to an Antiferromagnetic Insulator". In: *Phys. Rev. Lett.* 112 (11 Mar. 2014), p. 116404. DOI: 10.1103/PhysRevLett.112.116404. URL: https://link.aps.org/doi/10.1103/PhysRevLett.112.116404.

[62] Hua-Ding Song et al. "Asymmetric Modulation on Exchange Field in a Graphene-BiFeO3 Heterostructure by External Magnetic Field". In: *Nano Letters* 18 (Mar. 2018). DOI: 10.1021/acs.nanolett.7b05480.

[63] Wang-Kong Tse et al. "Quantum anomalous Hall effect in single-layer and bilayer graphene". In: *Phys. Rev. B* 83 (15 Apr. 2011), p. 155447. DOI: 10.1103/PhysRevB.83.155447. URL: https://link.aps.org/doi/10.1103/PhysRevB.83.155447.

[64] Subir K. Banerjee and Bruce M. Moskowitz. *Ferrimagnetic Properties of Magnetite*. Ed. by Joseph L. Kirschvink, Douglas S. Jones, and Bruce J. MacFadden. DOI: 10.1007/978-1-4613-0313-8_2. Boston, MA: Springer US, 1985, pp. 17–41.

[65] Rajender S. Varma Manoj B. Gawande Paula S. Brancoa. "Nano-magnetite (Fe3O4) as a support for recyclablecatalysts in the development ofsustainable methodologies". In: *Chemical Society Reviews* 8 (Nov. 2012). DOI: 10.1039/c3cs35480f.

[66] U.Schwertmann R.M.Cornell. *The Iron oxides:Structure, Properties, Reactions, Occurences and Uses*. DOI: 10.1002/3527602097. Wiley-VCH Verlag GmbH Co, 2003.

[67] Hoser A. Levy D. Giustetto R. "A. Structure of magnetite (Fe3O4) above the Curie temperature: a cation ordering study". In: *Phys Chem Minerals* 39 (Nov. 2012). DOI: 10.1007/s00269-011-0472-x, pp. 169–176.

[68] Denis Yan Ashok Gupta. *Chapter 17 Magnetic and Electrostatic Separation*. DOI: 10.1016/B978-0-444-63589-1.00024-1. Elsevier, 2016.

[69] Leonard Dobrzyński et al. "Chapter 5 - Surface, Interface, and Confined Slab Magnons". In: *Magnonics*. Ed. by Abdellatif Akjouj et al. Interface Transmission Tutorial Book Series. Elsevier, 2019, pp. 185–220. ISBN: 978-0-12-813366-8. DOI: https://doi.org/10.1016/B978-0-12-813366-8.00005-4. URL: http://www.sciencedirect.com/science/article/pii/B9780128133668000054.

[70] Matthias Opel. "Spintronic oxides grown by laser-MBE". In: *Journal of Physics D: Applied Physics* 45.3 (Dec. 2011), p. 033001. DOI: 10.1088/0022-3727/45/3/033001. URL: https://doi.org/10.1088%2F0022-3727%2F45%2F3%2F033001.

[71] Fausto Fiorillo, Carlo Appino, and M. Pasquale. "Hysteresis in Magnetic Materials". In: vol. 3. Dec. 2006, pp. 1–190. ISBN: 0-12-369433-7. DOI: 10.1016/B978-012480874-4/50019-1.

[72] Thierry F. Vandamme Justine Wallyn Nicolas Anton. "Synthesis, Principles, and Properties of Magnetite Nanoparticles for In Vivo Imaging Applications—A Review". In: *Pharmaceutics* 11 (Nov. 2019). DOI: 10.3390/pharmaceutics11110601.

[73] Taekyung Yu Wei Wu Zhaohui Wu. "Recent progress on magnetic iron oxide-nanoparticles: synthesis, surface functionalstrategies and biomedical applications". In: *Science and Technology of Advanced Materials* 16 (Feb. 2015). DOI: 10.1088/1468-6996/16/2/023501.

[74] Costica Caizer. *Nanoparticle Size Effect on Some Magnetic Properties*. Ed. by Mahmood Aliofkhazraei. DOI: 10.1007/978-3-319-13188-7$_2$4 − 1. Cham: Springer International Publishing, 2015, pp. 1–38. ISBN: 978-3-319-13188-7.

[75] Marc Widdrat1 Jens Baumgartner Luca Bertinetti. "Formation of Magnetite Nanoparticles at LowTemperature: From Superparamagnetic to Stable SingleDomain Particles". In: *PLos ONE* 8(3) (Jan. 2013). DOI: 10.1371/journal.pone.0057070.

[76] An-Hui Lu, E. L. Salabas, and Ferdi Schüth. "Magnetic Nanoparticles: Synthesis, Protection, Functionalization, and Application". In: *Angewandte Chemie International Edition* 46.8 (2007). DOI: 10.1002/anie.200602866, pp. 1222–1244.

[77] H. Kachkachi. "Effects of spin non-collinearities in magnetic nanoparticles". In: *Journal of Magnetism and Magnetic Materials* 316.2 (2007). DOI: 10.1016/j.jmmm.2007.03.212, pp. 248–254.

[78] R.H Kodama. "Magnetic nanoparticles". In: *Journal of Magnetism and Magnetic Materials* 200.1 (1999). DOI: 10.1016/S0304-8853(99)00347-9, pp. 359–372. ISSN: 0304-8853.

[79] R. H. Kodama et al. "Surface Spin Disorder in $NiFe_2O_4$ Nanoparticles". In: *Phys. Rev. Lett.* 77 (2 July 1996). DOI: 10.1103/PhysRevLett.77.394, pp. 394–397.

[80] Yu. S. Dedkov et al. "Rashba Effect in the Graphene/Ni(111) System". In: *Phys. Rev. Lett.* 100 (10 Mar. 2008), p. 107602. DOI: 10.1103/PhysRevLett.100.107602. URL: https://link.aps.org/doi/10.1103/PhysRevLett.100.107602.

[81] D. R. Hamann. "Optimized norm-conserving Vanderbilt pseudopotentials". In: *Phys. Rev. B* 88 (8 Aug. 2013), p. 085117. DOI: 10.1103/PhysRevB.88.085117. URL: https://link.aps.org/doi/10.1103/PhysRevB.88.085117.

[82] Harman Johll, Hway Chuan Kang, and Eng Soon Tok. "Density functional theory study of Fe, Co, and Ni adatoms and dimers adsorbed on graphene". In: *Phys. Rev. B* 79 (24 June 2009), p. 245416. DOI: 10.1103/PhysRevB.79.245416. URL: https://link.aps.org/doi/10.1103/PhysRevB.79.245416.

[83] Bin Wang and Sokrates T. Pantelides. "Magnetic moment of a single vacancy in graphene and semiconducting nanoribbons". In: *Phys. Rev. B* 86 (16 Oct. 2012), p. 165438. DOI: 10.1103/PhysRevB.86.165438. URL: https://link.aps.org/doi/10.1103/PhysRevB.86.165438.

[84] Peter Larkin. *Infrared and Raman Spectroscopy: Principles and Spectral Interpretation*. 1st ed. Elsevier, 2017.

[85] Rakesh Mohan Sharma Gurvinder Singh Bumbrah. "Raman spectroscopy-Basic principle, instrumentation and selected applications for the characterieation of drugs of abuse." In: *Elsevier* 6 (June 2015). DOI: 10.1016/j.ejfs.2015.06.001.

[86] Marek Prochazka. "Basics of Raman Scattering (RS) Spectroscopy , In: Surface-Enhanced Raman Spectroscopy". In: *Springer, Cham* (Dec. 2015). DOI: 10.1007/978-3-319-23992-7_2.

[87] G.Dresselhausb L.M.Malarda M.A.Pimentaa. "Raman spectroscopy in graphene". In: *Elsevier* 473 (Apr. 2009). DOI: 10.1016/j.physrep.2009.02.003.

[88] Ajit Jena and Wu Li. "Significant reduction of lattice thermal conductivity in suspended graphene by charge doping". In: *ResearchGate* (Aug. 2019).

[89] M. Mohr et al. "Phonon dispersion of graphite by inelastic x-ray scattering". In: *Phys. Rev. B* 76 (3 July 2007). DOI: 10.1103/PhysRevB.76.035439, p. 035439.

[90] S. Karamat et al. "Synthesis of few layer single crystal graphene grains on platinum by chemical vapour deposition". In: *Progress in Natural Science: Materials International* 25.4 (2015), pp. 291–299. ISSN: 1002-0071. DOI: https://doi.org/10.1016/j.pnsc.2015.07.006. URL: http://www.sciencedirect.com/science/article/pii/S1002007115000787.

[91] Andrea Ferrari and Denis Basko. "Raman spectroscopy as a versatile tool for studying the properties of graphene". In: *Nature nanotechnology* 8 (Apr. 2013), pp. 235–46. DOI: 10.1038/nnano.2013.46.

[92] R. Saito et al. "Raman spectroscopy of graphene and carbon nanotubes". In: *Advances in Physics* 60.3 (2011), pp. 413–550. DOI: 10.1080/00018732.2011.582251. eprint: https://doi.org/10.1080/00018732.2011.582251. URL: https://doi.org/10.1080/00018732.2011.582251.

[93] F. Tuinstra and J. L. Koenig. "Raman Spectrum of Graphite". In: *The Journal of Chemical Physics* 53.3 (1970), pp. 1126–1130. DOI: 10.1063/1.1674108. eprint: https://doi.org/10.1063/1.1674108. URL: https://doi.org/10.1063/1.1674108.

[94] Philippe Mallet-Ladeira et al. "A Raman study to obtain crystallite size of carbon materials: A better alternative to the Tuinstra–Koenig law". In: *Carbon* 80 (2014), pp. 629–639. ISSN: 0008-6223. DOI: https://doi.org/10.1016/j.carbon.2014.09.006. URL: http://www.sciencedirect.com/science/article/pii/S0008622314008574.

[95] L. G. Cançado et al. "Quantifying Defects in Graphene via Raman Spectroscopy at Different Excitation Energies". In: *Nano Letters* 11.8 (2011). PMID: 21696186, pp. 3190–3196. DOI: 10.1021/nl201432g. eprint: https://doi.org/10.1021/nl201432g. URL: https://doi.org/10.1021/nl201432g.

[96] A. C. Ferrari and J. Robertson. "Interpretation of Raman spectra of disordered and amorphous carbon". In: *Phys. Rev. B* 61 (20 May 2000), pp. 14095–14107. DOI: 10.1103/PhysRevB.61.14095. URL: https://link.aps.org/doi/10.1103/PhysRevB.61.14095.

[97] M.M. Lucchese et al. "Quantifying ion-induced defects and Raman relaxation length in graphene". In: *Carbon* 48.5 (2010), pp. 1592–1597. ISSN: 0008-6223. DOI: https://doi.org/10.1016/j.carbon.2009.12.057. URL: http://www.sciencedirect.com/science/article/pii/S0008622310000138.

[98] Daniel Johnson, Nidal Hilal, and W. Bowen. "Basic Principles of Atomic Force Microscopy". In: Dec. 2009, pp. 1–30. DOI: 10.1016/B978-1-85617-517-3.00001-8.

[99] Xinming Li et al. "Graphene and related two-dimensional materials: Structure-property relationships for electronics and optoelectronics". In: *Applied Physics Reviews* 4 (June 2017), p. 021306. DOI: 10.1063/1.4983646.

[100] Jagpreet Singh et al. "Graphene: from synthesis to engineering to biosensor applications". In: *Frontiers of Materials Science* 12 (Jan. 2018), pp. 1–20. DOI: 10.1007/s11706-018-0409-0.

[101] Jan Plutnar, Martin Pumera, and Zdeněk Sofer. "The chemistry of CVD graphene". In: *J. Mater. Chem. C* 6 (23 2018), pp. 6082–6101. DOI: 10.1039/C8TC00463C. URL: http://dx.doi.org/10.1039/C8TC00463C.

[102] Yi Zhang, Luyao Zhang, and Chongwu Zhou. "Review of Chemical Vapor Deposition of Graphene and Related Applications". In: *Accounts of chemical research* 46 (Mar. 2013). DOI: 10.1021/ar300203n.

[103] O. Leenaerts, B. Partoens, and F. M. Peeters. "Adsorption of H_2O, NH_3, CO, NO_2, and NO on graphene: A first-principles study". In: *Phys. Rev. B* 77 (12 Mar. 2008), p. 125416. DOI: 10.1103/PhysRevB.77.125416. URL: https://link.aps.org/doi/10.1103/PhysRevB.77.125416.

[104] Bing Huang et al. "Adsorption of Gas Molecules on Graphene Nanoribbons and Its Implication for Nanoscale Molecule Sensor". In: *The Journal of Physical Chemistry C* 112 (Aug. 2008), pp. 13442–13446. DOI: 10.1021/jp8021024.

[105] Stefan Goniszewski et al. "Correlation of p-doping in CVD Graphene with Substrate Surface Charges". In: *Scientific Reports* 6 (Mar. 2016), p. 22858. DOI: 10.1038/srep22858.

[106] Haomin Wang et al. "Hysteresis of Electronic Transport in Graphene Transistors". In: *ACS nano* 4 (Nov. 2010), pp. 7221–8. DOI: 10.1021/nn101950n.

[107] Zhi-Min Liao et al. "Hysteresis reversion in graphene field-effect transistors". In: *The Journal of Chemical Physics* 133.4 (2010), p. 044703. DOI: 10.1063/1.3460798. eprint: https://doi.org/10.1063/1.3460798. URL: https://doi.org/10.1063/1.3460798.

[108] Yumeng Shi et al. "Effective doping of single-layer graphene from underlying SiO_2 substrates". In: *Phys. Rev. B* 79 (11 Mar. 2009), p. 115402. DOI: 10.1103/PhysRevB.79.115402. URL: https://link.aps.org/doi/10.1103/PhysRevB.79.115402.

[109] Byoung Lee et al. "Issues with the electrical characterization of graphene devices". In: *Carbon letters* 13 (Jan. 2012). DOI: 10.5714/CL.2012.13.1.023.

[110] A. M. Goossens et al. "Mechanical cleaning of graphene". In: *Applied Physics Letters* 100.7 (2012), p. 073110. DOI: 10.1063/1.3685504. eprint: https://doi.org/10.1063/1.3685504. URL: https://doi.org/10.1063/1.3685504.

[111] Niclas Lindvall, Alexey Kalabukhov, and August Yurgens. "Cleaning graphene using atomic force microscope". In: *Journal of Applied Physics* 111.6 (2012), p. 064904. DOI: 10.1063/1.3695451. eprint: https://doi.org/10.1063/1.3695451. URL: https://doi.org/10.1063/1.3695451.

[112] Quan Wang et al. "Investigating change of properties in gallium ion irradiation patterned single-layer graphene". In: *Physics Letters A* 380 (Aug. 2016). DOI: 10.1016/j.physleta.2016.08.025.

[113] Anthea Agius Anastasi et al. "Raman spectroscopy of gallium ion irradiated graphene". In: *Diamond and Related Materials* 89 (2018), pp. 163–173. ISSN: 0925-9635. DOI: https://doi.org/10.1016/j.diamond.2018.09.011. URL: http://www.sciencedirect.com/science/article/pii/S0925963518302279.

[114] Zhichuan Xu et al. "Oleylamine as Both Reducing Agent and Stabilizer in a Facile Synthesis of Magnetite Nanoparticles". In: *Chemistry of Materials* 21 (May 2009). DOI: 10.1021/cm802978z.

[115] Walid Baaziz et al. "Few-Layer Graphene Decorated with Homogeneous Magnetic Fe3O4 Nanoparticles with Tunable Covering Densities". In: *Journal of Materials Chemistry* 2 (Dec. 2013). DOI: 10.1039/C3TA14512C.

[116] G. Greczynski and L. Hultman. "X-ray photoelectron spectroscopy: Towards reliable binding energy referencing". In: *Progress in Materials Science* 107 (2020), p. 100591. ISSN: 0079-6425. DOI: https://doi.org/10.1016/j.pmatsci.2019.100591. URL: http://www.sciencedirect.com/science/article/pii/S0079642519300738.

[117] Stephen J. Sque, Robert Jones, and Patrick R. Briddon. "The transfer doping of graphite and graphene". In: *physica status solidi (a)* 204.9 (2007), pp. 3078–3084. DOI: 10.1002/pssa.200776313. eprint: https://onlinelibrary.wiley.com/doi/pdf/10.1002/pssa.200776313. URL: https://onlinelibrary.wiley.com/doi/abs/10.1002/pssa.200776313.

[118] Mikhail Fonin et al. "Surface electronic structure of the Fe3O4(100): Evidence of a half-metal to metal transition". In: *Physical Review B, v.72, 104436-1-104436-8 (2005)* 72 (Sept. 2005). DOI: 10.1103/PhysRevB.72.104436.

[119] H Schulze et al. "A Small-Window Moving Average-Based Fully Automated Baseline Estimation Method for Raman Spectra". In: *Applied spectroscopy* 66 (June 2012), pp. 757–64. DOI: 10.1366/11-06550.

UNIVERSITÉ CATHOLIQUE DE LOUVAIN
École polytechnique de Louvain
Rue Archimède, 1 bte L6.11.01, 1348 Louvain-la-Neuve, Belgique | **www.uclouvain.be/epl**